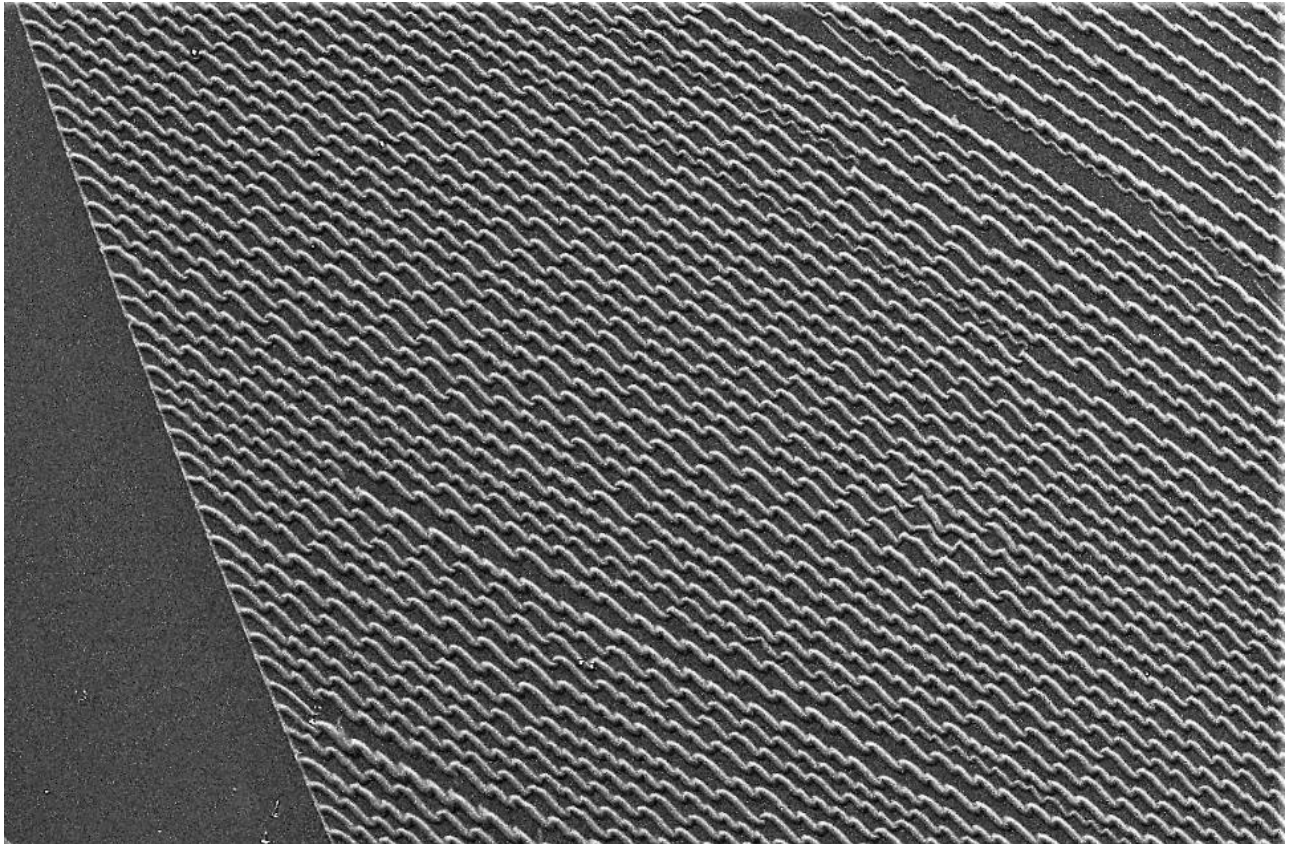


Plastic Deformation of Phyllosilicates
High temperature creep in muscovite single crystals



Master of Science Thesis

S.T. Verboom

September 2018
Faculty of Geosciences
Department of Earth Sciences
Utrecht University

Supervisors:

Dr. A.R. Niemeijer and Prof. Dr. C.J. Spiers



Universiteit Utrecht

Abstract

Earthquakes are an integral and catastrophic part of the seismic cycle. Due to their disruptive impact on society, there is a public as well as a scientific interest in accurate modeling of this cycle. Part of this, is constraining the maximum strength of the crust in the transition region between brittle and ductile rheologies. This maximum strength of long-lived faults is important in geodynamic models governing e.g. mountain building and collapse and volcano activity. In seismic models the strength of faults controls the strain build up before it's released in a seismic event. Ductile behavior is incorporated in such models via flow laws.

Phyllosilicates are abundant in faults and fault gouges. Incorporating their ductile behavior is necessary to accurately describe the behavior in long-lived faults. To date there are multiple flow laws for phyllosilicate creep, giving significantly different results in terms of stress and strain rate upon extrapolation from the laboratorial conditions under which they were established to nature. There are two groups of flow laws, one group with a power law relation between strain rate and stress ($\dot{\epsilon} \propto \sigma^n$) based on geometrical relations. The other group has an exponential relation between strain rate and stress ($\dot{\epsilon} \propto e^{\alpha\sigma}$) and finds its origin in the elementary atomic jump theory.

To distinguish between these two flow laws, sheets of single crystals of muscovite were submitted to three point bending tests under constant stress and elevated temperatures conditions. TGA measurements were performed to establish the maximum experimental temperature of 600°C to avoid dehydroxylation. The stresses employed varied between 0.1-0.4 MPa and temperatures between 500°C and 600°C. Strain and strain rates were calculated. Results were compared with previous work and both flow law approaches were fit to the data. After retrieval of the samples, they were examined with a Leica optical microscope and a scanning electron microscope. Microstructural observations displayed an array of different features that do not influence the deformation behavior, but are most likely shrinking features that form upon cooling.

The maximum of strain reached ranges between 0.6 – 1.0 %. After an initial period of thermal cooling due to the set-up, the initial strain rates are 10^{-6} s^{-1} , but decrease with time to 10^{-8} to 10^{-10} s^{-1} (=strain hardening). When a power law relation was fitted to the data, our results gave a stress exponent (n) of 1, corresponding with Harper-Dorn creep which assumes a constant dislocation density. This linear relation between stress and strain rate is previously found in combination with strain rates slower than 10^{-5} s^{-1} . At higher strain rates this value increased to ~18. When an exponential relation was fitted to the data, our results gave an exponential factor (α) of 4. Previous work found lower values of around 0.5.

There is too little data to conclusively distinguish between the two flow laws. However, from the Geometrically Necessary Dislocations (GND) theory it follows that in a bending geometry, dislocations of one sign need to accumulate in the crystal to accommodate the bend which conflicts with the assumption of a constant dislocation density. In addition, we also observed strain hardening, Harper-Dorn creep is therefore regarded unlikely. This leaves glide due to thermal vibration, as expressed by the exponential flow law, as the most likely operating mechanism.

This has implications for models that use a flow law with power law relation between stress and strain rate to incorporate phyllosilicate behavior. As the exponential relationship predicts higher strain rates for lower stresses, and therefore a weaker crust. This means that the strain will most likely be released aseismically before stresses necessary to initiate brittle behavior can build up.

Contents

Abstract	1
1. Introduction	3
1.1 Structural description of muscovite	5
1.2 Review of deformation by crystal defects	7
1.3 Theoretical models describing deformation through lattice defects	9
1.4 Introducing the general flow laws and their physical basis	9
1.5 Previous work and measured parameter values of micas	12
1.6 Aims of this thesis	16
2. Material and Methods	17
2.1 Materials	17
2.2 Apparatus description	18
2.3 Testing procedure	18
2.4 Experimental conditions	19
2.5 Microstructural analysis	19
2.6 Data processing/analysis	20
3. Results	23
3.1 TGA	23
3.2 Mechanical data	25
3.3 Flow law parameter values	35
3.4 Optical Results	38
4. Discussion	45
4.1 Comparison with previous work	45
4.2 Macroscopic observations	50
4.3 Microstructures	50
4.4 Underlying mechanism	57
4.5 Implications of my work	58
4.6 Suggestions for methodological improvements	59
4.7 Further research	59
5. Conclusion	61
6. Acknowledgements	62
7. References	62

1. Introduction

Earthquakes are counted among nature's most potentially destructive phenomena. Owing to their massive impact on society, earthquake hazard assessments are made with the aim of reducing damages by providing guidelines for the construction of buildings and infrastructures. Efforts are made in earthquake seismology and geophysics to estimate the probability of an earthquake of a given magnitude to occur within a certain time interval in a specific region (Satake & Atwater, 2007).

To do this, an understanding of the nature and the processes at play during the seismic cycle is essential. The macroscopic behavior of such large-scale phenomena is controlled by nano- and microscopic- (e.g. atomic and grain scale) or mesoscopic-scale physical and/or chemical processes. With the advent of (super)computers, (numerical) models have become increasingly important in aiding our study and understanding of both large-scale phenomena and the underlying small-scale processes. However, the accuracy of model predictions heavily depends on the quality of the input parameter values. A lot of research, especially in the discipline of rheology, is therefore aimed at uncovering the fundamental components and processes at work and their relationship to the macroscopic behavior. Material responds to stresses in roughly one of three ways: elastic, i.e. the deformation achieved is fully reversible, brittle, i.e. deformation is permanent and the integrity of the material is lost (e.g. fracturing), or ductile, i.e. deformation is permanent, but the integrity of the material remains intact (e.g. creep). The prevailing view is that earthquakes are the results of instantaneous elastic strain release by brittle friction processes occurring on preexisting faults, which are relatively weak compared to the fault wall rocks (Zhang & He, 2016). The conditions, e.g. stress (σ), temperature (T), pressure (P), that cause the materials response to switch from brittle behavior to ductile behavior or vice versa are therefore of interest.

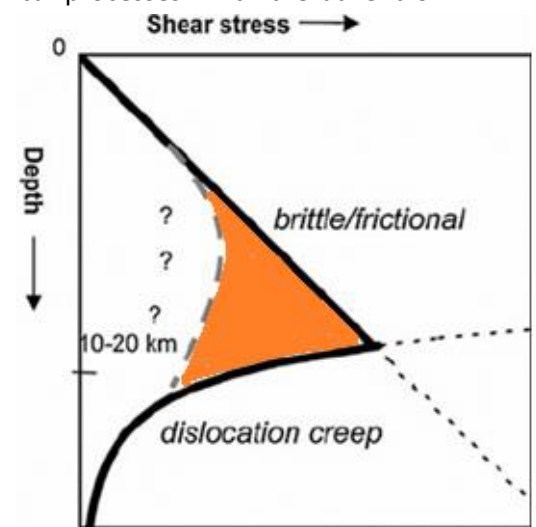


Figure 1 "Classic" crustal strength profile (based on Byerlee's rule) in solid black, and the possible crustal strength profile, taking into account complicating factors and weakening mechanisms represented by the grey dashed line. Figure after Bos & Spiers, 2002

In modeling of fault behavior, crustal strength profiles are constructed to predict the strength of the crust with depth, and the transition from brittle to ductile behavior. Such profiles, and the mechanical behavior response they describe, are helpful for understanding the seismic cycle (Bos & Spiers, 2002). "Classic" models use Byerlee's rule and produce two-mechanism profiles (see Fig. 1). The upper parts of the crust are modeled using a brittle-frictional faulting rheology, whereas the lower parts are described using power law creep equations describing crystal plastic flow of quartz or feldspar. Flow laws are constructed by considering the response of materials in terms of ductile deformation (rate), i.e. "the flow", during (quasi-)steady state deformation under various conditions (σ , T , P , etc.). These flow laws allow for extrapolation from laboratory to geologic and seismic cycle timescales (Bos & Spiers, 2002; Niemeijer & Spiers, 2005).

However, field findings are not always consistent with the strengths these "classic" models predict (e.g. Imber et al., 2008). These findings underline that there is an oversimplicity in the "classic" approach. This

oversimplicity is most likely to overestimate the maximum strength of the crust in the transition region between brittle and ductile rheologies (see Fig. 1). This maximum strength of long-lived faults is important in geodynamic models governing e.g. mountain building and collapse and volcano activity. In seismic models the strength of faults controls the strain build up before it's released in a seismic event.

Oversimplicity is partially due to the use of monomineralic flow laws for low strains. Furthermore weakening mechanisms such as pressure solution, the formation of reaction rate products, like phyllosilicates, and the development of an extensive foliation are postulated to explain the deviation. In the last decades, attempts to incorporate complicating factors as well as some of the weakening mechanisms in the crustal strength models are made (Bos & Spiers, 2002; Niemeijer & Spiers, 2005). These incorporations lead to an area where multiple mechanisms operate, called frictional-viscous flow, truncating the strength maximum at the transition, i.e. the steady state stresses at which crustal fault rocks deform could be lower than previously predicted. This means that both frictional and viscous processes, such as crystal plasticity/creep, are active under the same conditions. This produces shear deformation behavior in which the shear stress shows a significant dependence on both normal stress and strain rate (Bos & Spiers, 2002).

As phyllosilicates are major constituents of these fault rock and gouges (Wintsch et al., 1995; Imber et al., 2001) and they are relatively weak and thought to contribute significantly to the localization of strain in the Earth's crust (Moore and Lockner, 2004; Shea and Kronenberg, 1992; Niemeijer and Spiers, 2005; Imber et al., 2008), incorporating their ductile rheology into models could significantly improve their accuracy. The model of Niemeijer and Spiers (2005) allowed for phyllosilicate creep to influence the crustal strength profile. The laboratory flow law for single crystal biotite by Kronenberg et al. (1990) (see Fig. 2a) with a power law fit was used as input. However, it is unknown under which conditions which mechanism is controlling phyllosilicate creep. There are multiple mechanisms with corresponding flow laws that can be fit to data obtained in laboratorial experiments. Most used are flow laws with either a power law or an exponential relation between strain rate and stress. These flow laws describing these mechanisms can predict different results when extrapolated (see Fig. 2 and e.g. Fagereng et al., 2014). More research towards the mechanical behavior of these minerals is needed to improve our understanding of the mechanisms involved and to enable researchers to select the one most accurate for their work.

Exponential vs Power

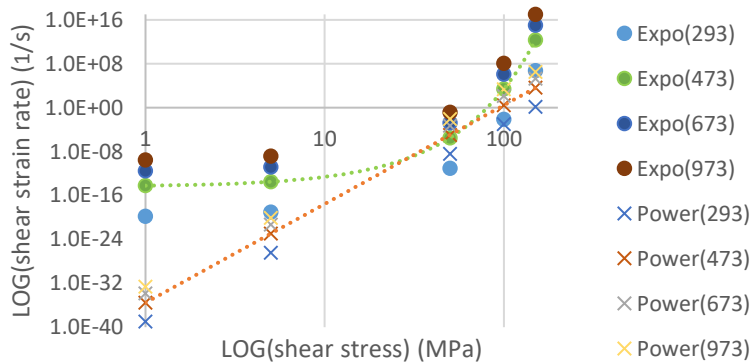


Figure 2a Kronenberg et al. (1990) fitted flow laws with a power law ($n=18$) as well as an exponential law ($\alpha=0.4$) relation to their data of single crystal biotite. They obtained the data in the area with a well agreement between both models, but extrapolating it shows already a large deviation. The values between brackets are the temperatures in Kelvin.

Exponential vs Power

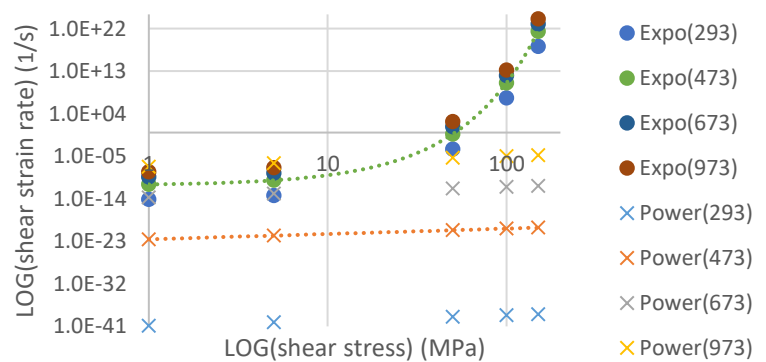


Figure 2b Mariani et al. (2006) fitted a flow law with a power law relation ($n=1$) to data of muscovite powder and Mares & Kronenberg (1993) fitted one with an exponential law relation ($\alpha=0.5$) to data of single crystal muscovite. The values between brackets are the temperatures in Kelvin.

In this thesis I have investigated the deformation behavior of muscovite, a phyllosilicate common to fault gouges and shear zones at deeper levels in the Earth's crust (Mariani et al, 2006), as affected by stress. To this end, constant stress experiments on single crystals were conducted in a three-point bending set up. The results, and specifically the observed stress dependence, were compared with existing laboratory flow laws, against a theoretical background. The theoretical background consists of a description of the muscovite structure, a review of crystal defects and associated theoretical rheological models, and a review of the physical basis of the present flow laws. The aim is to gain more insight in the parameter constraints of the existing flow laws and gain a better understanding of the active physical mechanisms. This should give flow laws that are better constrained, thereby improving the accuracy of the extrapolations needed for modeling.

1.1 Structural description of muscovite

Muscovite belongs to the silicate group and its crystallography is well described by e.g. Putnis (2003). Silicates are a mineral group whose structures is dominated by the $[\text{SiO}_4]$ tetrahedron (see Fig. 3a & b). Classifications are made in terms of the way in which these tetrahedra are arranged. Tetrahedra can be isolated from each other or connected by corner-sharing. Within micas the tetrahedra are connected by sharing three corners, forming sheets with a hexagonal symmetry by doing so (see Fig. 3c).

Muscovite consists of two basic building blocks: two sheets of $[\text{SiO}_4]$ tetrahedra sandwiching a sheet of edge sharing octahedra (making them 2:1 layer silicates). The unbound apices of the tetrahedra sheets all point towards the octahedra sheet in the middle, sharing their apical oxygen atoms with the octahedra (see Fig. 4). A feature of muscovite, but also of mica in general, is the substitution of Al^{3+} for Si^{4+} in the tetrahedron. The $[\text{AlO}_4]$ tetrahedron is slightly larger than the $[\text{SiO}_4]$ tetrahedron. Al-tetrahedrons are in general not found next to each other, since this is energetically unfavorable. These substitutions results in an overall negative charge on these layers, which is compensated by large, positively charged interlayer cations, mostly K^+ , Na^+ or Ca^+ (see Fig. 4a). The smallest repeatable block of this structure is called the unit cell and is repeated periodically in three dimensions and this forms the crystal lattice.

When a trivalent ion such as Al^{3+} or Fe^{3+} occupies the tetrahedra, charge balance is achieved when two thirds of the octahedral sites are occupied. In this case, each hexagonal ring of tetrahedra contains two octahedra and the sheet is termed dioctahedral, as is the case for muscovite. When a divalent ion such as Mg^{2+} or Fe^{2+} is contained in the octahedra all sites are occupied. Each hexagonal ring of tetrahedra contains three octahedra and the sheet is called trioctahedral, as is the case for biotite. The dioctahedral sheet is more distorted than the trioctahedral sheet, since the vacant sites are larger than the occupied sites around it (see Fig. 5).

This structure leads to the polytypism observed in mica's. In the tet-oct-tet sandwich, the two opposing tetrahedral sheets are not directly opposite one another (see Fig. 4a). There is an offset, the so called 'stagger factor', which is necessary to produce the octahedral co-ordination in the octahedral sheet. To

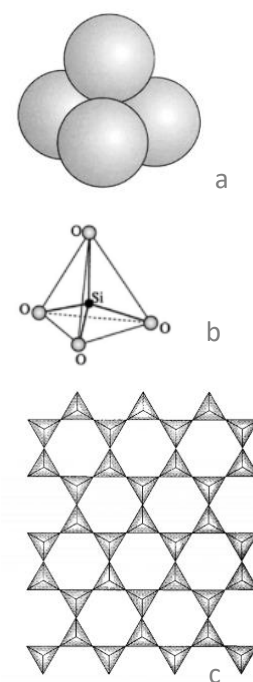


Fig 3 a & b) the silica tetrahedron, c) silica tetrahedra sharing 3 corners (figures from Putnis, 2003)

add to this, the hexagonal symmetry in the tetrahedral sheet means that this offset can be in any of the six directions. For a given direction of the offset in one layer, the important point is how the offsets in consecutive layers are related to one another. There are six possible interlayer stacking angles (see Fig. 6). The most common muscovite polytype in nature is a 2M polytype with a 20 angstrom (Å) (001) layer spacing. The M stands for monoclinic, which means that the axes of the crystals have different lengths ($a \neq b \neq c$) and the angle between a and b , called γ , and b and c , called α , is identical but different than the angle between a and c , called β (see Fig. 7). Viewed along the c -axis, you look down on the (001) plane, also known as the basal plane. For 2M muscovite unit cell $a = 5.19 \text{ Å}$, $b = 9.04 \text{ Å}$, $c = 20.08 \text{ Å}$ and $\alpha = \gamma = 90^\circ$, and $\beta = 95.5^\circ$. A single layer of muscovite is $\sim 10 \text{ Å}$, so the 2M polytype has a unit cell containing two layers. In a 0.1 mm thick sample of muscovite, there are 100 000 individual layers.

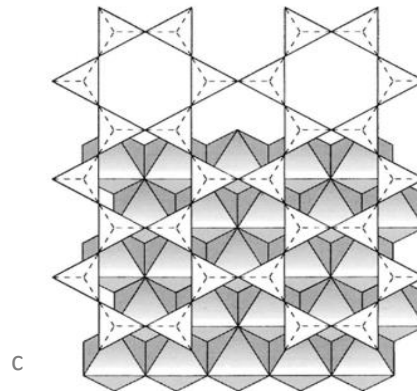
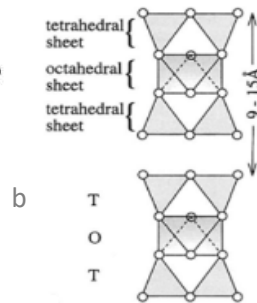
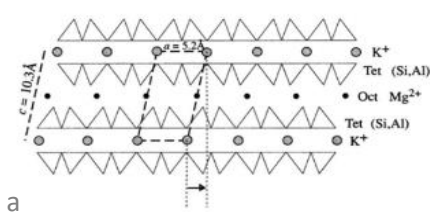


Fig 4 a & b) structure of muscovite
c) the way tetrahedra sheet are configured on top of an octahedra sheet (figures from Putnis, 2003)

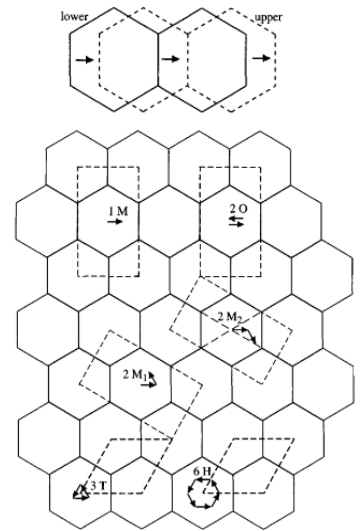


Fig 6 The stagger factor and the 6 possible ways to stack mica layers. 2M is the most common polytype of muscovite (figure from Putnis, 2003)

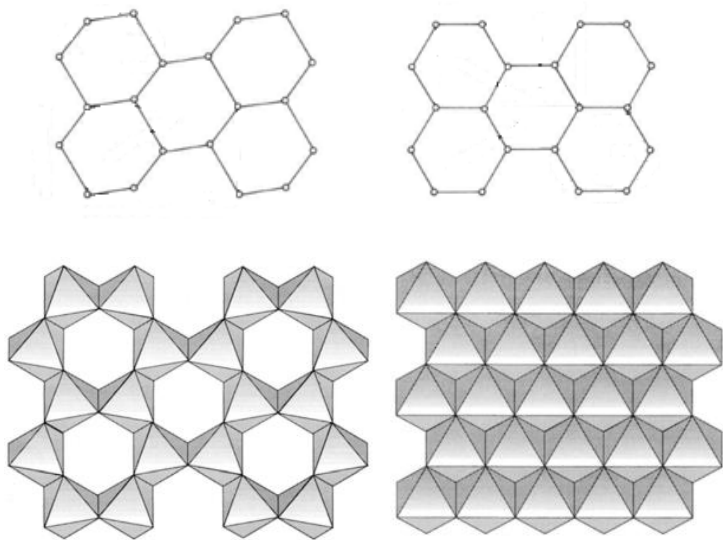


Fig 5 a) In muscovite (1M), two out of three octahedron sites are occupied, giving rise to a distortion (top figure after Meike, 1989, bottom figure from Putnis, 2003)
b) In biotite, all three octahedron sites are occupied (top figure after Meike, 1989, bottom figure from Putnis, 2003)

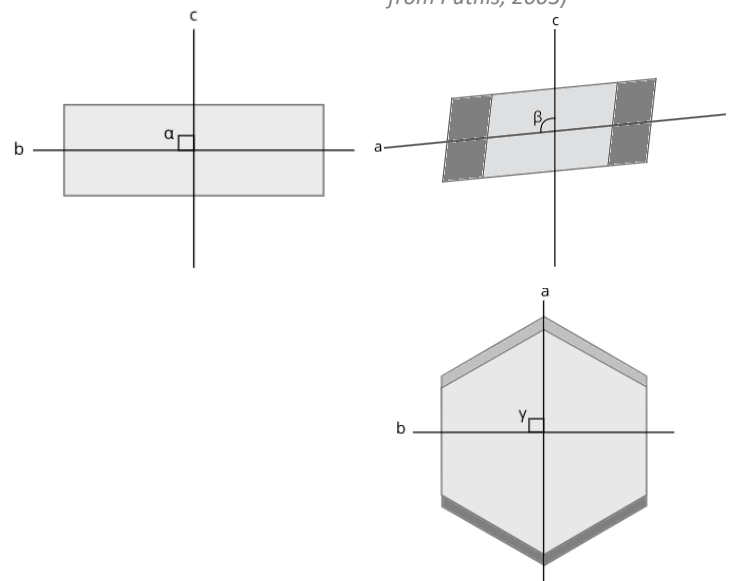


Figure 7 The hexagonal symmetry of muscovite viewed along the a -axis, the b -axis and the c -axis. Showing the 90° angle between the a - and b -axis, and the b - and c -axis. Viewed along the c -axis you look down on the (001) plane, also known as the basal plane.

1.2 Review of deformation by crystal defects

In the early 1900s the atomistic and periodic nature of crystalline substances was fully established and attempts were made to relate the macroscopic behavior of minerals to their crystal lattice. One of the topics of interest was the plastic strength of materials, i.e. the shear stress needed to produce permanent plastic deformation. The theoretical shear strength was estimated by assuming all bonds within a plane of a lattice needed to be broken simultaneously. However, these estimates were several orders of magnitude higher than the strengths measured during experiments. To explain this discrepancy, it was postulated that defects are present in the crystal. The presence of defects distorts the lattice in such a way that the bonds neighboring a defect are weaker than the bonds in a perfect lattice. Therefore, introducing defects allows for consecutive breaking of the surrounding bonds at lower stresses than otherwise needed for breaking perfect bonds. Thereby aiding the ease of deformation and lowering the plastic strength.

Nowadays the existence of crystal defects is well established, although new types of crystal/lattice defects are still being discovered (Griggs et al., 2017; Kushima et al., 2015). In the following a short overview of the different, well established, defect groups will be presented. Recently discovered defects that might be relevant for this work, will be discussed in Section 4.2.

1.2.1 Point defects

1. A vacancy (see Fig. 8a) exists when an atom is missing from its regular arrangement in the lattice. Vacancies are responsible for deformation by diffusive transport of matter. For entropic reasons, there is an equilibrium concentration of vacancies present in all crystals, dependent on the temperature (Putnis, 2003). Stress modifies the equilibrium vacancy concentration in crystals. Their migration obeys diffusion equations equivalent to those governing the diffusion of heat. Vacancies can help line defects overcome obstacles.

2. An impurity defect (see Fig. 8b) exists when an regular atom is swapped for another atom, but still keeps its regular place in the arrangement.

3. An interstitial defect (see Fig. 8c) exists when a regular atom is found in a different site than what could be expected from the regular arrangement of the lattice.

Impurities and interstitials do not directly contribute to deformation, but they can form obstacles for dislocations impeding their motion.

1.2.2 Line defects (dislocations)

1. Edge dislocations (see Fig. 9) consist of an extra half plane of atoms in the crystal. They move, parallel to the direction of the burgers vector, through the crystal by successively breaking the bonds between atoms. If edge dislocations move out of their current glide plane, it is called climb.

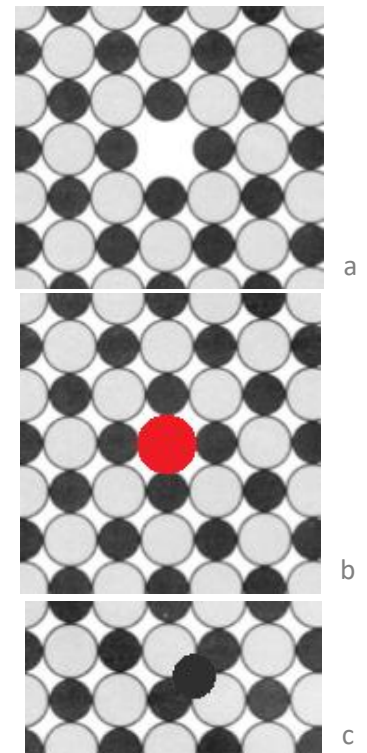


Figure 8 Examples of point defects in a crystal lattice. a) a vacancy, b) an impurity, c) an interstitial (figure a from Putnis, 2003), b & c are modified after Putnis, 2003

2. Screw dislocations (see Fig. 10) consist of an extra half plane of atoms in the crystal. They move, perpendicular to the direction of the burgers vector, through the crystal by successively breaking the bonds between atoms. If screw dislocations move out of their current glide plane, it is called cross-slip.

Dislocations are responsible for deformation by moving through the crystal lattice. Dislocations create an internal strain field and stress field, whose strength decreases as the inverse of the distance to the dislocation (Poirier, 1985). Their motion is impeded by the energy barrier separating two equilibrium positions in the lattice and by obstacles. The product of individual movements of dislocations results in slip. It is common for the dislocation line to not move as a straight line. As some parts of the dislocation line encounter obstacles and become pinned for a certain amount of time, or permanent, depending on the (size of) the obstacle. This causes some part of the dislocation line to climb/cross slip to different glide planes, and parts of the dislocation line will advance a little more than the pinned parts. This creates an irregular dislocation line, with so called jogs

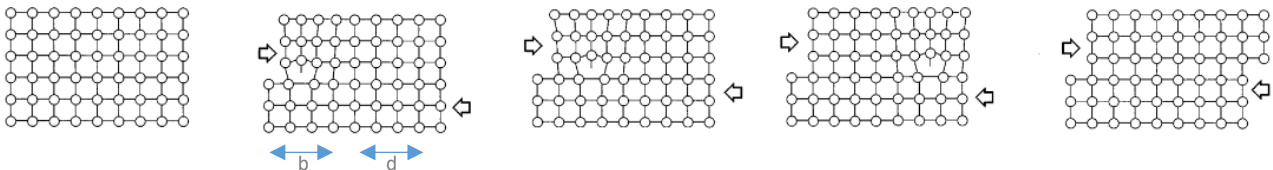


Fig 9 A edge dislocation and the way it moves through the crystal resulting in strain (figure from Putnis, 2003). b stands for the orientation of the burgers vector, d stand for the direction of the dislocation glide.

1.2.4 Dislocation arrays

Dislocations do not always run entirely through a crystal and produce macroscopic slip. They can get stuck, pile up, tangle and organize themselves in walls, kinkbands, and networks in order to achieve the lowest possible energy configuration. This raises the dislocation density of the crystal, which increases dislocation interactions and it decreases the overall deformation rate, a process called work hardening (Hull & Bacon, 2011). Rearrangement and detangling of dislocations under suitable circumstances (e.g. high enough thermal energy to assist climb), can cause softening and an increase in overall deformation rate, a process known as recovery. When line defect organize themselves in three dimensional structures, e.g. dislocations walls, these features are called planar defects. On longer timescales, planar defects can offset the internal structure of the grains enough to form new grains.

Dislocations can either be homogeneously distributed throughout the crystal, or tangles of dislocations can arrange themselves in regions with high dislocation density, such as walls, and regions almost free of dislocations. The configuration and orientation of the dislocations in these high density regions is along certain crystallographic directions (Hull & Bacon, 2011). Therefore, distribution and organization of dislocations are characteristic of the structure of the material being deformed, but also of deformation temperature, strain and strain rate (Hull & Bacon, 2011).

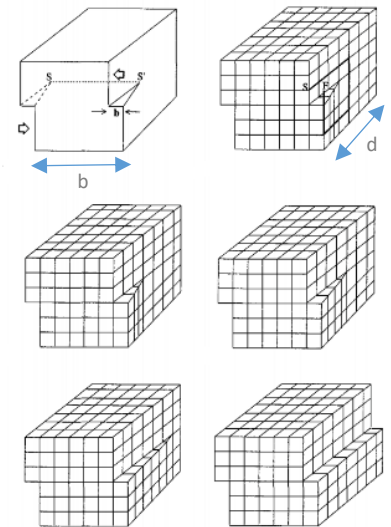


Fig 10 A screw dislocation and the way it moves through the crystal resulting in strain (figure from Putnis, 2003) b stands for the orientation of the burgers vector, d stand for the direction of the dislocation glide.

Dislocation configurations can be made visible with a transmission electron microscope using thin films (Meike, 1989) or with SEM using decorating techniques, like etching (Karato, 1987).

1.3 Theoretical models describing deformation through lattice defects

Glide controlled slip: This type of deformation occurs when dislocations movement is restricted to their current crystallographic plane. Obstacles are thermally overcome, i.e. the activation energy for flow (J mol^{-1}) depends on σ . Movement of the dislocation is parallel to the direction of the burgers vector.

Climb & Cross slip: These types of deformation occurs when respectively edge or screw dislocations aided by vacancies move out of their current glide plane to overcome, for example, obstacles. It is only indirectly thermally activated via the migration of vacancies. Movement of the dislocation, during this out of plane movement, is perpendicular to the plane of the burgers vector.

Vacancy diffusion: This is a diffusive transport mechanism aiding the operation of cross slip and climb, enabling dislocation movement where they would otherwise be stuck in their glide plane due to obstacles. The rate of vacancy diffusion and stress are linearly related ($\dot{\epsilon} \propto \sigma^1$).

1.4 Introducing the general flow laws and their physical basis

Flow laws are constitutive equations with underlying creep models giving the physical basis for the empirical relations. Phenomenological analysis of deformation is best done on quasi-steady state, constant-stress creep-test results, since they provide time-independent empirical equations of state of the form $\dot{\epsilon} = f(\sigma, T, P)$, where $\dot{\epsilon}$ is the (shear) strain rate (s^{-1}), σ the (shear) stress (MPa), T is the temperature (K), and P the pressure (MPa).

1.4.1 Temperature relations

At constant stress, the creep rate usually increases exponentially with temperature, and it is therefore convenient to describe the creep rate by an Arrhenius-type relation:

$$\dot{\epsilon} \propto \exp\left(-\frac{\Delta Q}{RT}\right) \quad (1)$$

where R is the gas constant ($8.3145 \text{ J mol}^{-1} \text{ K}^{-1}$).

If the strain-rate is controlled by a unique, thermally activated process, the Arrhenius plot ($\ln \dot{\epsilon}$ vs $1/T$) is a straight line over the whole temperature range investigated and the apparent activation energy of creep (ΔQ) is equal to the activation energy of the controlling process. However, it is often the case that several potential rate-controlling processes exist, with different activation energies. As a result the Arrhenius plot is curved in the temperature range where the activity of two or more mechanisms is comparable (see Fig. 11, Poirier, 1985).

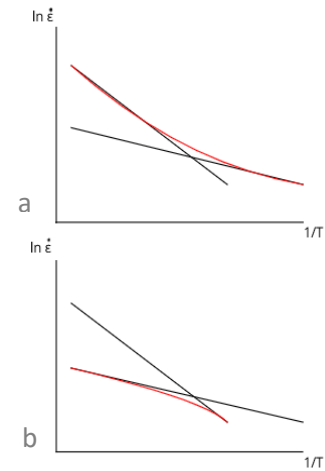


Figure 11, Arrhenius plots for two rate-controlling processes (black) and the overall rate (red). a) parallel processes, the faster process controls the overall rate, b) series processes, the slower process controls the overall rate (figure after Poirier, 1985)

1.4.2 Stress relations

Stress can be related to strain rate using two fundamentally different approaches. It is commonly observed that at small stress intervals, the strain rate as a function of stress on a double-logarithmic scale plot shows a straight line. One general procedure is to fit a power law of the form $\dot{\epsilon} \propto \sigma^n$ to the data and obtain a stress exponent. However, since the curve of strain rate as a function of stress on a double-logarithmic scale plot seldom fits a straight line over a wide range of applied stresses and at high stresses increases exponentially, the other approach is to fit an exponential function to the data. Both approaches have their physical foundations and benefits, which will be discussed below.

1.4.2.1 Power law

From theoretical considerations we know that a linear dependence exists between stress and strain rate ($\dot{\epsilon} \propto \sigma^1$) if vacancy diffusion is rate-controlling, to aid climb and cross slip of the dislocations. Furthermore, the stress field around dislocations decays as the inverse of the distance to the dislocation. As such, any dislocation configuration in equilibrium will have a characteristic length: $l \propto \sigma_i^{-1}$ where σ_i is the internal stress field. It follows that dislocation density $\propto \sigma_i^2$ (Poirier, 1985). This gives recovery controlled creep, such as cross slip and climb, a stress exponent of 3.

The flow laws following the power law relationship between (differential) stress and strain rate are generally of the form:

$$\dot{\epsilon} = A \sigma^n \exp\left(\frac{-\Delta Q}{RT}\right) \quad (2)$$

A and n are material parameters, σ is the shear stress (MPa), (e.g. Mariani et al., 2006; Mares & Kronenberg, 1993).

These power law relations are only valid for a small domain of stress (Poirier, 1985). Over a wide range of stresses, the plot of experimentally obtained data is usually no longer a straight line. One way to solve this problem, is to fit several models, each corresponding to a power law with a unique n-value, presumably corresponding to physically meaningful parallel-concurrent processes. For high stresses the creep-rate is observed to increase exponentially with stress and the power law approach render invalid.

1.4.2.2 Power law creep models

Weertman creep: is a climb (and/or cross slip) controlled recovery creep. It states that edge (and/or screw) dislocations are generated in different planes, and dislocations of opposite sign migrate towards each other (climbing out of their “birth” plane), to annihilate. It has a theoretical stress exponent of 3, although it is in practice observed in the range 3-5.

Harper – Dorn creep: is a specific type of dislocation creep, where at small stresses the dislocation density is quite low and independent of stress. The creep arises from the climb of edge dislocations under saturated conditions, i.e. the concentration of jogs is high enough for climb to be controlled by vacancy diffusion to and from the dislocations, as is assumed in most climb-controlled models. The strain rate is related to stress only by the vacancy diffusion, giving rise to a stress exponent of 1. At higher stresses the exponent “returns” to a normal value of 3-5.

1.4.2.3 Exponential law

The exponential flow law finds its origin in elementary (atomic scale) jump theory. An atom thermally vibrates around an equilibrium position. Every now and then, the atom acquires enough energy to jump over the energy barrier separating it from the next equilibrium position. Lattices are made of periodically repeating units in 3 dimensions and equilibrium positions for each atom are also repeated periodically in 3 dimensions. With no other forces/stresses present, this jump is equally likely to be backward as forward. One can determine forward jump frequency (i.e. the amount of successful jumps forward) and vice versa the backward jump frequency. It is a thermally activated process, and is described by an Arrhenius type of equation. Applied shear stresses can influence the favored jump direction.

Applied stresses, such as normal stress (σ_n) and shear stress (τ) can raise this barrier, i.e. impeding successful jumps, or lower it, i.e. promoting successful jumps, which is described by (Chen & Spiers, 2016):

$$v_n = A \exp\left(\frac{-\Delta F + \Omega \sigma_n}{kT}\right) \sinh\left(\frac{\Omega \tau}{kT}\right) \quad (3)$$

Where v_n is net jump frequency, ΔF is the maximum energy barrier at zero normal or shear stress, A comprises the lattice vibration frequency and the burgers vector, and Ω include geometric parameters associated with the barrier. If the reverse jump frequency can be approximated by zero, due to high stresses compared with kT , the equation can be reduced to the form:

$$v_n = A \exp\left(\frac{-\Delta F + \Omega \sigma_n}{kT}\right) \exp\left(\frac{\Omega \tau}{kT}\right) = A \exp\left(\frac{-\Delta Q}{kT}\right) \exp(\alpha \tau) \quad (4)$$

Where A and α are material parameters (Kronenberg et al., 1990; Shea and Kronenberg, 1992; Mares and Kronenberg, 1993). ΔQ is, as defined earlier, the apparent activation energy and contains $(\Delta F - \Omega \sigma_n)$, α is a material parameter containing $\frac{\Omega}{kT}$.

The (shear) strain rate is given by Orowan's equation as stated by Cottrell (1953):

$$\dot{\epsilon} = \rho v_g b \quad (5)$$

Where ρ is the density of mobile dislocations, and v_g is the average dislocation glide velocity. This approach assumes dislocation glide controlled by dispersed obstacles (Manonukul et al., 2002). Obstacles obstruct the glide of dislocations, a process called pinning of dislocations. Following Dunne et al. (2007), this average dislocation glide velocity is defined as length of the thermal event (d) times the rate of escape of pinned dislocations (RFE):

$$v_g = d \cdot RFE = d \cdot \frac{b}{2l} v_n = A' \exp\left(\frac{-\Delta Q}{kT}\right) \exp(\alpha \tau) \quad (6)$$

Where A' constitutes A times $d \frac{b}{2l}$. Taking equation (6) with equation (5) together gives:

$$\dot{\epsilon} = \rho b \cdot A' \exp\left(\frac{-\Delta Q}{kT}\right) \exp(\alpha \tau) = A'' \exp(\alpha \tau) \exp\left(\frac{-\Delta Q}{kT}\right) \quad (7)$$

Experiments were used to determine the values for A'' , α and ΔQ . When the creep rate is determined by the average velocity of glide dislocations, it is determined by the nature of the obstacles that pin the dislocations, and the thermal activation events that are necessary to enable dislocation climb (Manonukul

et al., 2002). More detailed assessments of the parameters Ω , A and α are made for different materials (e.g. Manonukul et al. (2002) for nickel-base super alloy C263; Dunne et al. (2007) for hcp near-alpha Ti-6 Al alloy), and although the parameters represent the mechanism(s) at work, to go into their details would be beyond the scope of this thesis.

1.4.2.4 Differences in approach between power law and exponential law

Power law creep incorporates in plane glide and out of plane climb of dislocations. Strain rate to stress relations are based on geometrical relations, following a power law type of equation.

Exponential creep finds its physical basis in the elementary (atomic) scale jump theory and describes in plane glide limited by the energy barrier generated by obstacles. This is a thermally activated process which is aided by stress. Therefore, strain rate is related to stress via an Arrhenius type of equation.

1.5 Previous work and measured parameter values of micas

Previous studies reported that mica's can respond to stress in roughly three ways. Kink bands (KBs) are observed to accommodate deformation when samples are loaded parallel to their basal planes (Griggs et al., 2017; Kronenberg et al., 1990). Samples loaded perpendicular to their basal planes usually deform by fracturing at high stresses (Kronenberg et al., 1990). Samples loaded under an angle to their basal planes show indications of creep behavior. Deformed samples have broad deformation bands, with undulose/undulatory extinctions, approximating simple shear (Kronenberg et al., 1990). In this work, the aim was to activate the last response.

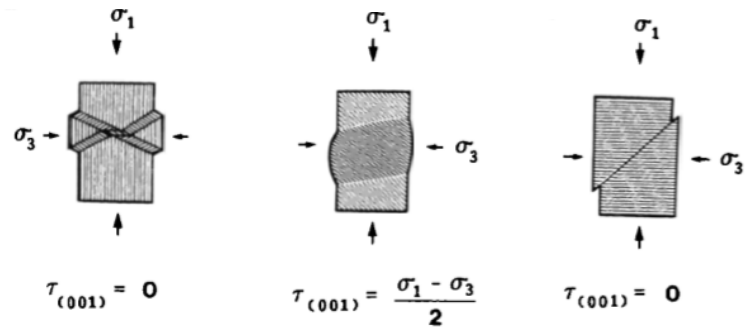


Figure 12 Figures from Kronenberg et al. (1990) (their Figure 1) depicting the three basic modes of deformation in muscovite single crystals. Left: samples loaded parallel to their basal plane, resulting in kinkbands. Middle: samples loaded at an angle to their basal plane, resulting in broad deformation bands approximating simple shear. Right: samples loaded perpendicular to their basal plane, resulting in failure by fracturing at high stresses.

Although extensive research has been done on mathematically describing deformation/creep behavior in general (e.g. Manonukul et al, 2002; Dunne et al, 2007) and on phyllosilicate minerals specifically (e.g. Moore & Lockner, 2004) the work discussed in this section will concentrate on earlier studies on creep behavior of mica's. Explicitly or implicitly the microscale mechanism responsible for deformation of muscovite at high temperatures in the reviewed literature is glide of dislocations in the basal plane (BDs). Non-basal dislocations are not observed as they would require very high burgers vectors due to the large c/a ratio (see Section 1.1; for 2M muscovite $c/a = \sim 4$), which renders their existence nearly impossible (Griggs et al., 2017; Gruber et al., 2016; Hull & Bacon, 2011). In earlier work the power law relationship as well as the exponential are discussed and/or fitted to the data. The findings are summarized in Table 2.

Mariani et al. (2006) performed saw cut shear experiments in a triaxial set up on a muscovite powder with a grainsize of $\sim 12 \mu\text{m}$. The experimental temperature varied between 300°C and 700°C and they achieved strains up to 2%. For the highest temperatures pore water pressures up to 103 MPa were used to inhibit the dehydroxylation of the muscovite aggregates. Shear strain rates varied between $1 \times 10^{-3} \text{s}^{-1}$ and $1 \times 10^{-7} \text{s}^{-1}$ and the shear stresses reported varied between 14 MPa and 160 MPa. A total of 28 experiments were performed whereof 17 stress relaxation tests. These relaxation tests were used to determine the stress

dependence in a power law relation. They found a stress exponent of 1.13 ± 0.12 for strain rates slower than $1 \times 10^{-5} \text{ s}^{-1}$ and a stress exponent of ~ 19 was found for strain rates faster than $1 \times 10^{-5} \text{ s}^{-1}$. They could not obtain a well constrained value for the apparent thermal activation energy, so instead they calculated a minimum value for ΔQ to be 270 kJ mol^{-1} . Kronenberg et al. (1990) performed triaxial compression experiments, shortening single crystals of biotite with dimensions $5.5 \times 5.5 \times 15 \text{ mm}$. The experimental temperature varied between 20°C and 400°C and strains of $\sim 15\%$ were achieved. Strain rates varied between $4.6 \times 10^{-4} \text{ s}^{-1}$ and $2.0 \times 10^{-7} \text{ s}^{-1}$, differential stresses required to achieve this varied between 16 MPa and 460 MPa at 5% strain. A total of 19 experiments were performed, whereof 2 strain rate stepping experiments. When loaded at 45° to the basal plane (001), they found a stress exponent of 18 ± 4 and an apparent activation energy of $51 \pm 9 \text{ kJ mol}^{-1}$.

Mares & Kronenberg (1993) performed 23 triaxial compression experiments, whereof 4 temperature stepping and 3 strain rate stepping experiments, on single crystals of muscovite with dimensions $15 \times 6 \times 6 \text{ mm}$. Experimental temperatures varied between 20°C and 400°C and strains of $\sim 12\%$ were achieved. Strain rates varied between $2.3 \times 10^{-4} \text{ s}^{-1}$ and $2.5 \times 10^{-7} \text{ s}^{-1}$, differential stresses required to achieve this varied between 0.5 MPa and 75 MPa at 3% strain. When loaded at 45° to the basal plane (001), they found an α -value of 0.5 ± 0.2 for a fit using an exponential relation and an apparent activation energy of $47 \pm 19 \text{ kJ mol}^{-1}$. Kronenberg et al. (1990) also fitted an exponential relation to their data for single crystal biotite (for description: see previous paragraph). They found an α -value of 0.41 ± 0.8 and an apparent activation energy of $81 \pm 13 \text{ kJ mol}^{-1}$.

Figure 2 displays the results of the two different approaches. In Figure 2a Kronenberg et al. (1990) fitted a power law relation as well as an exponential relation to their data for single crystals of biotite. The data was obtained in the region with the best fit between both approaches. As soon as the stresses start to deviate from the experimental conditions, the two approaches predict vastly different strain rates. In Figure 2b the data of Mariani et al. (2006) for muscovite powder is fitted to a power law relation, and the data of Mares & Kronenberg (1993) for single crystals of muscovite is fitted to an exponential relation. Maraini et al. (2006) explicitly state that their flow law is determined for a temperature of 700°C (973 Kelvin), and temperature has a larger effect on the predicted strain rates than in the flow law of Mares & Kronenberg (1993).

From Figure 2a it follows that applying an exponential relationship between strain rate and stress lowers the strength of the crust. This means that the strain will most likely be released aseismically before stresses necessary to initiate brittle behavior can build up.

	sample	method	conditions	n	Q [kJmol ⁻¹]	α	Mechanism
Mariani et al., 2006	Fine grained muscovite	Triaxial shearing Constant displacement (28) Whereof: Stress relaxation (17)	T between 300 and 700°C P _c of 206 MPa $\dot{\epsilon}$ between 10 ⁻³ and 10 ⁻⁷ s ⁻¹ ϵ up to 2	1.13 ± 0.12 ($\dot{\epsilon}$ < 1.4*10 ⁻⁵) 19 ($\dot{\epsilon}$ > 1.4*10 ⁻⁵)	270	-	Kinking --> glide on (001)
Mariani et al., 2006				n(7): ϵ = 0.5 – 1.9% $\dot{\epsilon}$ = 10 ⁻³ - 10 ⁻⁶ s ⁻¹ T = 700°C P _c = 206 MPa	Estimated based on the absence of the transition to linear viscous flow in experiments done at 600°C (compared to those of 700°C)	-	
Mares & Kronenberg, 1993	Single crystals muscovite	Triaxial compression Constant strain rate (23) Whereof: T stepping (4) $\dot{\epsilon}$ stepping (3)	T from 20°C to 400°C P _c from 10 to 400 MPa $\dot{\epsilon}$ from 2.5 x 10 ⁻⁷ to 2.3 x 10 ⁻⁴ s ⁻¹ σ from 0.5 to 75 MPa (= $\sigma_1 - \sigma_3$) at 3% (varies to keep $\dot{\epsilon}$ constant)	-	47 ± 19	0.5 ± 0.2 (they “missed” a data point redone the calculation: 0.27)	Assumed: glide (equation)
Mares & Kronenberg, 1993		Determine basal shear strength as a function of (P_c, T, $\dot{\epsilon}$, shear direction) Differential stress is taken as a measure of shear strength. Higher diff. stress = stronger Directions: [110], [100], [310], [010] [100],[110] the weakest No reported influence of ϵ	T: strength increases as T decreases. Same in all 4 directions $\dot{\epsilon}$: small changes in strength with big changes in $\dot{\epsilon}$ (only in 2 directions [110], [010]) iffy if they are equal P _c : strengths are independent of P _c above 100 MPa (only in 2 directions [110], [310]) low P _c gives way to frictional sliding	-	Q (3): determined at P _c = 200 $\dot{\epsilon}$ = 2*10 ⁻⁵ ϵ = 5% T (30, 100, 200, 400) All directions 1/T vs stress, slope of Q/ α R	A (4): determined at P _c = 200 T = 400 ϵ = 5% $\dot{\epsilon}$ = 2*10 ⁻⁴ , 10 ⁻⁵ , 10 ⁻⁶ , 10 ⁻⁷ [110][010] Stress vs ln $\dot{\epsilon}$, slope of α	

Table 1 Previous work

Kronenberg et al., 1990	Single crystals biotite	Triaxial compression Constant strain rate (19) Whereof: $\dot{\epsilon}$ stepping (2)	T between 20°C and 700°C P_c up to 600 MPa $\dot{\epsilon}$ 2.0×10^{-7} to $4.6 \times 10^{-4} \text{ s}^{-1}$	18±4	82 ± 13 51 ± 9	0.41 ± 0.08	Slip on (001) & glide
Kronenberg et al., 1990				n (7 constant $\dot{\epsilon}$, 2 $\dot{\epsilon}$ stepping): determined at P = 200-499 MPa T = 400 °C $\dot{\epsilon}$ = 10^{-5} - 10^{-7} ϵ = 5%? Ln($\dot{\epsilon}$) vs Ln(stress) Slope 1/n	Q (12): determined at P = 200-499 MPa $\dot{\epsilon}$ = $2.4 \times 10^{-5} \text{ s}^{-1}$ ϵ = 5% T (20, 200, 400) All directions 1/T vs stress, slope Q/ α R 1/T vs Ln(stress), slope Q/nR	α (7 constant $\dot{\epsilon}$, 2 $\dot{\epsilon}$ stepping): determined at P = 200-499 MPa T = 400 °C $\dot{\epsilon}$ = 10^{-5} - 10^{-7} ϵ = 5%? Ln($\dot{\epsilon}$) vs stress Slope 1/ α	
Shea & Kronenberg, 1992	Mica schist (70% biotite)	Triaxial compression Constant strain rate (74) Whereof: T stepping (12) $\dot{\epsilon}$ stepping (5) P stepping (1)	T from 25°C to 400°C P_c to 500 MPa constant $\dot{\epsilon}$ from 1.7×10^{-5} ϵ varying up to 12%	31 ± 1 (ss) 171 ± 6 (ws) (depends on history, see α)	89 98 ± 9	0.15 ± 0.01 (ss) 0.55 ± 0.04 (ws) (depends on history: ss: fast to slow ws: slow to fast)	
Shea & Kronenberg, 1992				n (5): $\dot{\epsilon}$ = 10^{-4} - 10^{-7} Assumption of constant Q History tested Ln($\dot{\epsilon}$) vs Ln(stress) Slope 1/n (ss) just on one (BS-Z14) (ws)	Q(10, T stepping): determined at P = 200-300 MPa $\dot{\epsilon}$ = $1.7 \times 10^{-5} \text{ s}^{-1}$ ϵ = 2% T (25/35, 100, 200, 400) History tested as well 1/T vs stress, slope Q/ α R 1/T vs Ln(stress), slope Q/nR	α (5): Assumption of constant Q History tested Ln($\dot{\epsilon}$) vs stress Slope 1/ α (ss) just on one (BS-Z14) (ws)	

Table 1 (continued) Previous work

1.6 Aims of this thesis

The power law relation and the exponential law relation, although both fitting to data equally well within small ranges, predict significant differences in stress or strain rate when extrapolated from the conditions under which they were established (see Fig. 2). It is therefore useful to further investigate rheological behavior of minerals, and micas in particular, and try to relate the data to actual physical processes operating.

Data describing the inelastic single-crystal mechanical properties and deformation mechanisms of muscovite are currently all from constant strain rate triaxial compression experiments and some (strain rate, temperature, pressure) stepping experiments. In this research a three point bending set up was used instead of the triaxial compression set up, allowing constant stress experiments to be performed. The aim was to achieve quasi-steady state creep with an attempt to activate basal dislocation glide. The acquired data and results will be compared with previous work and against a theoretical background. The aim is to gain more insight in the processes at work during the deformation, and establish better constrained parameter values for the flow laws.

2. Materials and Methods

2.1 Materials

One particular member of the phyllosilicate group, called muscovite, will be studied in this work. Muscovite was chosen because of its abundant presence in fault gouges at deeper levels in the crust. It is easy to buy in specific shapes and with standardized quality, so called grades, therefore ensuring as little sample to sample variations as possible.

Muscovite with 4V grade was used (with 25% air content according to the supplier (SPI supplies)). It was ordered in squares of 25 x 25 mm and with a thickness of 0.26 mm. The squares were cut in half to a size of 12 x 25 mm with a slow circle saw. This gave a first set of samples with two different orientations of the crystallographic a- and b-axes. Samples with the long axis at a small angle to [010], and samples with long axis at a large angle to [010]. The orientations of the crystallographic axes were determined from interference figures using the Bertrand lens on a Leica optical microscope. Another set of samples were cut to 8 x 22 mm, so that the a- and b-axes are aligned parallel to, respectively, the short and long edges of the sample (see Table 2). The long sides were cut similar to the other set with a slow saw. The slow saw caused significantly more damage to the short edges, and therefore these were cut with a “cutter”. Various sample thicknesses were used in both sets (0.047 mm up to 0.26 mm). The original thickness (0.26 mm) was reduced with a razorblade separating the mica sheets from one another. Final thicknesses were measured with a Mitutoyo outside micrometer (0.001mm instrumental precision). Samples were macroscopically inspected for tears and other surface damages before use.

A small amount of muscovite powder (used for TGA measurements) was made by cutting a part of a sheet with a razorblade to smaller pieces and sieved with a 50 µm sieve.

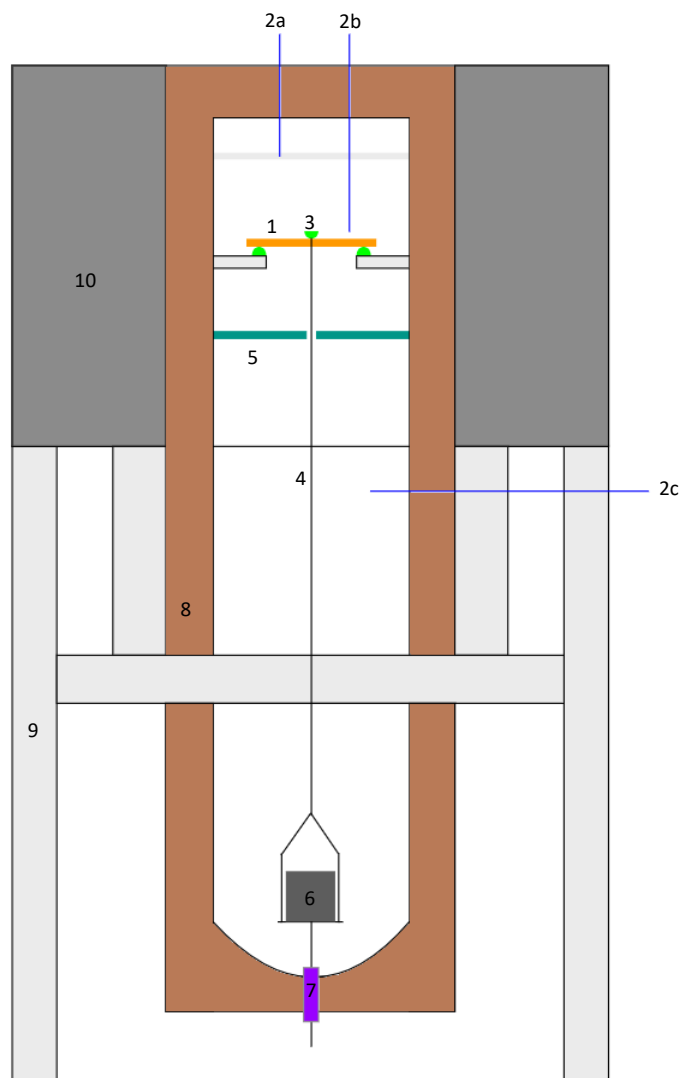


Figure 13 Apparatus set up. 1. (orange) is the sample. 2. (blue) are the thermocouples controlling the temperature of the ovenchamber. 3. (green) are the two semi-cylindrical rods onto which the sample is place, and semi-cylindrical rod which transmits the load of the deadweight, 4. is a kanthal wire, 5. (seagreen) steel plate guiding the kanthal wire, 6. (dark grey) dead-weight providing the load, 7. (purple) LVDT measuring the displacement of the samples centre (aka the bending), 8. (brown) frame that holds the sample, 9. (light grey) is the frame onto which the ovenchamber is placed, 10. (dark grey) the ovenchamber (the chamber encloses the entire sample set up). Figure is not to scale, the height of the entire set-up is ± 70 cm.

2.2 Apparatus description

Samples were placed in a three-point-bending apparatus as shown in Figure 13. The apparatus consists of two frames (8 and 9) with a removable oven chamber (10). Open spaces between the oven chamber and the frame were filled with insulating material. In the top of the frame two thermocouples were placed. One is connected to a temperature control box and regulates the overall oven temperature within $\pm 1^\circ\text{C}$ (2a). The other one (2b) is placed closer to the sample and registers the temperature just above the sample. The third one (2c) was placed just below the oven chamber, to register outside temperature fluctuations, possibly affecting the measurements. Temperatures were registered with a Type-K Thermocouple and Amplifier. In the middle of the chamber two small support beams equipped with semi-cylindrical rods (3) form the supports on which the sample (1) is placed. The semi-cylindrical rods are separated by a gap of 10 mm between them. A dead-weight (6) provided a constant load throughout the experiment, transmitted through a semi-cylindrical rod placed on top (3) and in the middle of the sample. The beam is connected to a loading disc at the bottom of the frame by a kanthal wire (4). The wire was guided through a steel plate (5) to prevent horizontal movement. At the bottom of the frame is the loading disc supporting the dead-weight. The disc has a small piston onto which the dead-weight is placed to prevent movement. The disc itself is connected to a Linear Variable Differential Transformer (LVDT) (7) with a range of 1 mm which corresponds to a range of 20 Volt analogue output. As the sample will bend and deform, the loading disc will lower and the connected LVDT measures this movement. Data was acquired using a National Instruments 16 bit A/D converter with a frequency of one measurement every second. SignalExpress software was used to collect the data.

On a final note, some approaches to data analysis in a three point bending set-up make direct use of the gap width between the supports and it is argued that at large deflections the use of semi-cylindrical supports creates a small decrease of this gap (see Fig. 14, Ogorkiewicz & Mucci, 1971), but considering the small amount of deflection achieved (see Fig. 42), the distance loss was regarded insignificant.

2.3 Testing procedure

Samples were placed into the apparatus using tweezers. During assembling the loading disc was supported to prevent direct application of the load. Before closing the oven chamber the sample was briefly loaded to make sure the experiment started with a proper signal of the LVDT to prevent data loss by the LVDT being out of range. The LVDT could be moved up and down in the frame to adjust the range accordingly. During heating to the experimental temperature the sample was unloaded. The final temperature was reached after about two hours by slowly raising the temperature to prevent exposing the sample to temperatures far above the designated temperature. After reaching the correct temperature the apparatus was equilibrated at this temperature and stay in a $\pm 1^\circ\text{C}$ range for at least 30 minutes. When the temperature was stable, the support of the loading disc was carefully removed to place the load onto the sample. Note that after loading, the wire is displaced with an amount of 0.4mm out of the oven chamber. This means that the wire is not in thermal equilibrium and will shorten a bit at the beginning of the experiments due to thermal cooling. Experiments were done with dead-weights of

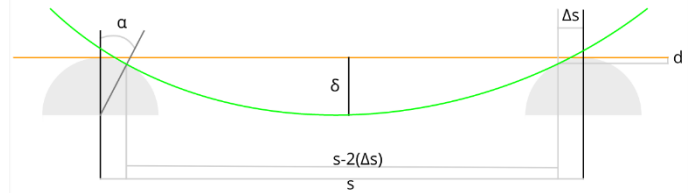


Figure 14 The undeflected sample (orange), and the deflected sample (green), δ is the maximum amount of deflection, Δs is the distance the tangent plane between the sample and the semi-cylindrical rods shifts when the sample is deflected, α is the angle between the normal of the tangent plane, s is the original distance between the support contact points, which is decreased by $2(\Delta s)$ when the sample is deflected, d is the distance the contact point lowers on the support (figure after Ogorkiewicz & Mucci, 1971)

15.9 – 31.8 – 62.15 grams, and ran for at least 24h up to several weeks. At the end of the experiment the temperature controller was switched off, allowing the apparatus to cool. The load remained applied to the sample, to prevent rebounding of the sample at still elevated temperatures (see reversible strain hysteretic loops, Basu et al., 2009). After reaching room temperature the set up was disassembled, the retrieved samples were placed into sample holders awaiting further analysis.

2.4 Experimental conditions

Previous work suggested that at or below 600°C dehydroxylation does not occur (Mares & Kronenberg, 1992 (citing Vedder & Wilkens, 1969)). However, other research states that the dehydroxylation reaction starts as early as 400 °C and comes to completion between 640°C and 820 °C (Mariani et al., 2006). Therefore, thermogravimetric analysis (TGA) was done to determine the highest possible experimental temperatures at which dehydroxylation does not occur. Our data did not show significant weight loss up to 600°C, and this became our highest temperature employed.

The average sample stress, in contrast with the applied force, takes into account the way the force is distributed over the sample (stress = force / the area the force is acting on). Therefore, to calculate the stress, one must assume a deformation geometry. In these experiments it is assumed that only one slip system is activated, which causes the crystal to behave like a ‘deck of cards’ (Ranalli, 1995). With the assumption of this geometry, the sample failed by fracturing when loaded with a stress of 0.56 MPa. Therefore, experiments were done with varying stresses under 0.5 MPa. See table 2 for an overview of the experiments conducted.

2.5 Microstructural analysis

The samples developed macroscopically visible features during the high temperature experiments. Microstructural analysis of the starting materials and the deformed specimens were carried out using a Leica optical microscope and a table top scanning electron microscope (SEM). For SEM imaging specimens were prepared with a platinum coating. Secondary electron images were used to study the surface structures. “Live” images of back scattered electron were examined to see if there were any phase changes, but none were found. Infrared spectroscopy (IRS) was used to see if there was a measurable difference in e.g. OH content, but once again no differences could be found within a deformed sample.

2.6 Data processing/analysis

Before experiments were conducted the size and thickness of samples [mm] we measured. During experiments direct measurements were made of the temperature [°C] inside the oven, the temperature [°C] outside the oven, and dead-weight displacement [volts]. The LVDT has a range of 20 volts, corresponding to 1 mm. All displacement data in volts was therefore divided by 20 to obtain the displacement in mm. Due to the initial thermal cooling of the kanthal wire (see Section 2.3) the first two minutes of the experiments were examined with care. The start of the experiment (i.e. the point of 0.00% strain) was chosen to be the part at which the down displacement became dominant over the apparent upward motion due to the thermal cooling (see Fig. 18). The experiments ran with a constant load [g]. See Table 2 for an overview of the experiments and their conditions.

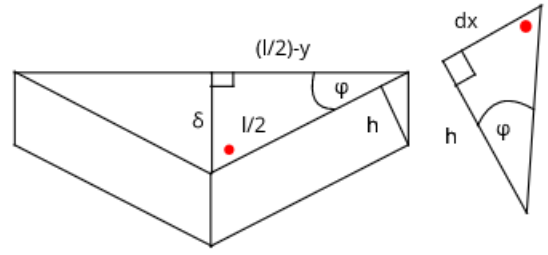


Figure 15 Left: deformation geometry, represented as two identical blocks experiencing simple shear, l is the length of the sample [m], h is the thickness of the sample [m], Δx is the sheared distance [m], δ is the maximum deflection [m], φ is the angle between the deflected surface and the original undeflected surface. Right: enlargement of the small triangle in the top right

Stress, strain and strain rates are calculated with respect to a chosen deformation geometry. For this experimental set up a “deck of cards” geometry was assumed. This is basically two juxtaposed blocks experiencing simple shear (see Fig. 15). When φ is very small, as would be the case for very small deflections, y approaches 0 and therefore both legs of the triangle are approximated to have the same length.

Generally speaking, strain is calculated as:

$$\gamma = \frac{\Delta x}{h} = \tan \varphi \quad (5)$$

where γ is the strain [-], Δx is the sheared distance [m] and h is the thickness of the sample [m]. φ is the angle between the original undeflected surface and the deflected surface. δ and l are known, γ is unknown. φ in the small triangle is the same as φ in the large triangle, therefore

$$\tan \varphi = \sin^{-1} \frac{2\delta}{l} = \frac{2\delta/l}{\sqrt{1-(\frac{2\delta}{l})^2}} \quad (6)$$

where δ is the maximum deflection [m] and l is the length of the sample [m]. If you multiply this by l it gives:

$$\gamma = \frac{2\delta}{\sqrt{l^2 - (2\delta)^2}} \quad (7)$$

However in our experiments $l \gg 2\delta$, as a result φ becomes very small, and γ can be approximated by:

$$\gamma = \tan \varphi = \frac{\delta}{l/2} = \frac{2}{l} \cdot \delta \quad (8)$$

Strain rate are successively calculated by taking the time derivative of the strain:

$$\dot{\gamma} = \frac{d\gamma}{dt} = \frac{2}{l} \cdot \frac{d\delta}{dt} \quad (9)$$

Stresses [Pa] were calculated assuming that during (quasi-)steady-state deformation, the total work put into the “system” (i.e. the muscovite crystal) by the dead-weight is dissipated entirely by internal shear deformation (i.e. there are no other energy sinks $W = D$). The work put into the system can be written as

$$W = F \cdot \delta \quad (10)$$

where W is the work put into the system [J], F is the force exerted by the dead-weight (mass [kg] * gravitation acceleration [ms^{-2}]) [N] and, and δ is the deflection (i.e. the lowering of the dead weight) [m]. The total energy dissipation can be written as:

$$d = \tau \cdot \gamma \quad (11)$$

where d is the energy dissipated per unit volume of crystal [Jm^{-3}] and τ is the shear stress [MPa] This is divided over the entire volume of the crystal as:

$$D = d \cdot V = d \cdot lbh \quad \text{with } V = lbh \quad (12)$$

D is the total energy dissipated in the entire crystal [Jm^{-3}] and V is the crystal volume [m^3], with b the width of the sample [m]. Combining (11) and (12) gives:

$$D = \tau \cdot \gamma \cdot lbh = W = F \cdot \delta \quad (13)$$

Rewriting (9) gives the following equation for the shear stresses on our samples:

$$\tau = \frac{l \cdot F \cdot \delta}{2lbh\delta} = \frac{F}{2bh} \quad (14)$$

Strains were calculated directly from the displacement data. The data showed a significant amount of noise, e.g. caused by the small temperature fluctuations and some difficulties were encountered when calculation strain rate. One approach was to take the first time a certain amount of strain was reached, and taking the derivative of that point. This however did not correspond well with the general curve reaching that amount of strain and was therefore discarded. The other approach was to take all the times the strain was reached within a certain time frame and calculate a mean, but this gave strains that deviated from the designated strain. Ultimately we decided to fit small straight lines to the data (see Fig. 23 top) and taking the time derivative of these small segments to calculate the strain rate (see Fig. 23 bottom).

Sample	l * w [mm]	d [mm]	W [g]	°to b	σ [MPa]	T [°C]	ϵ [%]	$\dot{\epsilon}_i$ [s ⁻¹]	$\dot{\epsilon}_{ss}$ [s ⁻¹]	Obs	Comments
0	-	-	-	-	-	room	-	-	-		No experiment done on it
1	22 * 12	0.25	15.9		0.025997	600	0.25	4.6*10 ⁻⁶	1.5*10 ⁻⁸		
4	22 * 12	0.119	31.8	30	0.109229	600	0.50	4.2*10 ⁻⁶	8.8*10 ⁻⁹	SEM	
16	25 * 12	0.096	31.8		0.135398	600	0.15	2.3*10 ⁻⁶	3.3*10 ⁻⁸		Second part (NR), not included
5	22 * 12	0.13	31.8		0.099987	600	0.25	5.0*10 ⁻⁶	3.4*10 ⁻⁸		Second part (NR), not included
7	22 * 12	0.06	31.8		0.216638	600	0.60	4.3*10 ⁻⁶	9.7*10 ⁻⁹		
8	25 * 12	0.117	62.15	81	0.217127	600	2.1 (1.0)	7.0*10 ⁻⁶	1.2*10 ⁻⁷	SEM	Abnormal large amount of strain
6	22 * 12	0.055	31.8		0.236332	600	0.70	4.3*10 ⁻⁶	1.4*10 ⁻⁸		
9	25 * 12	0.098	62.15		0.259223	600	1.0	4.3*10 ⁻⁶	1.1*10 ⁻⁸		Jump in data, fixed
11	25 * 12	0.091	62.15	77	0.279163	600	0.60	6.4*10 ⁻⁶	1.5*10 ⁻⁸	SEM	
10	25 * 12	0.09	62.15		0.282265	600	0.6	1.1*10 ⁻⁵	9.9*10 ⁻⁹		
21	25 * 12	0.116	62.15	0	0.328498	600	0.3	2.9*10 ⁻⁶	2.2*10 ⁻⁸	LEICA	
19	25 * 12	0.098	62.15	0	0.388834	600	0.9	2.2*10 ⁻⁶	7.5*10 ⁻⁹	LEICA	
22	25 * 12	0.07	62.15		0.362912	500	0.50	8.3*10 ⁻⁸	2.6*10 ⁻⁸		NB. first data points after 365s!
25	25*12	0.09	62.15		0.282265	500	1.4	1.7*10 ⁻⁷	3*10 ⁻¹⁰		
12	25 * 6	0.09	31.8		0.28885	600	0.0040	1.3*10 ⁻⁶	2.8*10 ⁻⁹		No smooth data
13	25 * 6	0.09	62.15		0.56562	room	-	-	-		Broke after loading
14	25 * 12	0.13	-		-	600	-	-	-	SEM	Unsupported
15	25 * 12	0.079	-		-	600	-	-	-	SEM	Supported

Table 1 Experimental conditions. l*w is length times width, i.e. the dimensions of the sample, d is the thickness of the sample. w is the added dead weight, °to b is the angle the long edge of the sample makes with the b axis, σ is the stress on the sample, T is the temperature during the experiment, ϵ is the total strain accumulated in the sample during the experiment (first 100 000s). $\dot{\epsilon}_i$ is the strain rate measured at the start of the experiment, $\dot{\epsilon}_{ss}$ is the strain rate measured during the approximate steady part of the experiment (after 100 000s). (NR) means not reliable. Obs is observation method

3. Results

This study had the aim to investigate the deformation of muscovite at elevated temperatures in a three point bending set up. The hypothesis was that glide of basal dislocations could be activated to achieve permanent deformation/strain. In this section the results of the TGA measurements, the mechanical data and the inferred parameter values, and microstructural data from the experiments will be presented.

3.1 TGA

The highest experimental temperatures were determined using thermogravimetric analysis (TGA) (Fig. 17). The TGA curves were used to determine whether and to what extent water loss would occur. The green line is the weight loss curve during heating. The blue line represents the reaction rate. The weight loss before the start of the dehydroxylation reaction up to a temperature of 150°C is attributed to evaporation of water absorbed to the surface. The weight loss observed from start to completion is interpreted to represent solely the dehydroxylation of muscovite (Mariani et al., 2006). In the 0.274 mm thick sheet of muscovite dehydroxylation did not initiate until 693 °C, and goes to completion after 900 °C with a total weight loss of 4.16%. No significant water loss was detected up to 654°C for the 0.134 mm thick sheet of muscovite with completion after 900 °C and a total weight loss of 4.257%. The muscovite powder of 50 µm starts the dehydroxylation reaction at 450 °C, with completion at 900 °C and a total weight loss of 4.49%. This is in good agreement with the expected total hydroxyl content of muscovite (structural formula: $\text{KAl}_2(\text{AlSi}_3\text{O}_{10})(\text{F,OH})_2$, with H_2O contributing 4.5228% of the weight). It should be noted that the curves are not at full completion at 900°C, since the reaction rate is not returned to zero. If the lines are extrapolated, the estimated total water loss increases with 0.04% for the muscovite powder and with 0.164% for the sheets. Temperatures at which the reaction rate peaked are roughly the same for the three samples, around 800°C. The reaction rates at each peak are, however, different. The powders dehydration rate is roughly twice as fast as the rate of the sheets. See Table 3 for an overview of these results. Another interesting result of the TGA experiments is the “fanning” of the heated sheet samples (see Fig. 16). This fanning was not observed in the sheet samples used in the three point bending experiments.

According to our TGA data, there is no significant water loss in the single crystals up to temperatures of 600°C. We therefore employed a maximum temperature of 600 °C in the three point bending tests.

Sample	Initial water loss [wt%]	Water loss before start [wt%]	Start [°C]	Peak [°C]	Rate at peak [%/min]	Completion [°C]	Water loss start - completion [wt%]
50 µm powder	0.31	0.31 + 0.308	450	795	0.32	900 (+10)	3.872 (+0.04)
0.134 mm	0.138	0.138 + 0.300	654	803	0.191	900 (+25)	3.819 (+0.164)
0.274 mm	0.073	0.073 + 0.147	693	805	0.183	900 (+25)	3.94 (+0.164)

Table. 3 TGA data overview

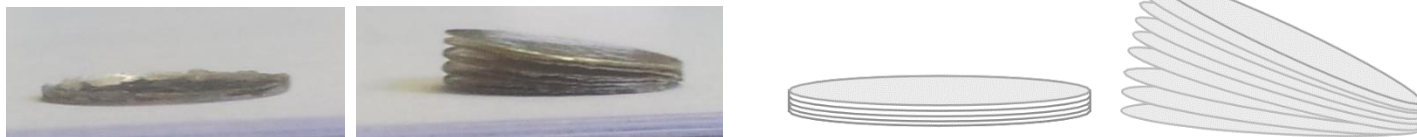


Figure 16 Muscovite discs before and after being heated to 900°C during the TGA measurements. The sample is “fanned” out after heating.

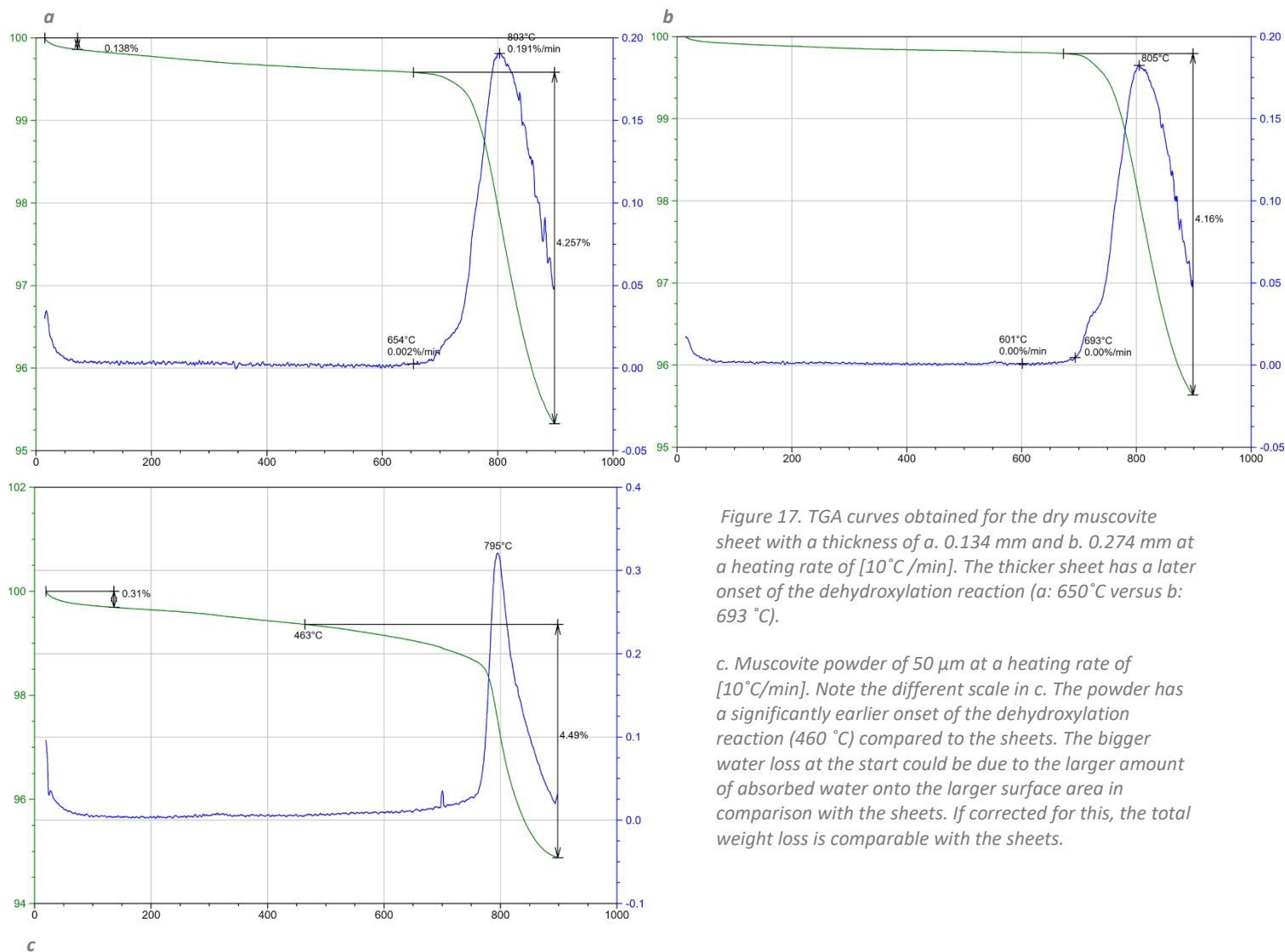


Figure 17. TGA curves obtained for the dry muscovite sheet with a thickness of a. 0.134 mm and b. 0.274 mm at a heating rate of [10°C/min]. The thicker sheet has a later onset of the dehydroxylation reaction (a: 650°C versus b: 693 °C).

c. Muscovite powder of 50 μm at a heating rate of [10°C/min]. Note the different scale in c. The powder has a significantly earlier onset of the dehydroxylation reaction (460 °C) compared to the sheets. The bigger water loss at the start could be due to the larger amount of absorbed water onto the larger surface area in comparison with the sheets. If corrected for this, the total weight loss is comparable with the sheets.

3.2 Mechanical data

We will first describe the general time evolution of sample displacement, strain and strain rate using experiment 11 as a representative sample. Afterwards we will compare and discuss experiments done with different stress and temperature conditions. Before presenting the details of the results, it should be noted that the achieved deflection was in the order of 0.1 mm, corresponding to strains smaller than 1%.

3.2.1 Instantaneous response and thermal cooling

A close inspection of the first minutes of the experiments revealed that multiple processes operate simultaneously, obscuring the measurements of sample deformation (see Fig. 18). When the assembly is heated, the semi cylindrical rod transferring the dead weight to the sample is lifted off the sample by 0.4 mm. After the start of the experiment, the dead weight is lowered onto the sample, instantaneously extruding the 0.4 mm of wire out of the oven chamber. This wire cools down from the designated temperature to a new equilibrium temperature, and shortens accordingly (i.e. it counteracts the displacement generated by deformation). To exclude this effect for as much as possible from our data, we choose the lowest point in the displacement data as the point with 0.0% strain. See table 4 for an overview of the data for all experiments. The two or three seconds it takes to reach its peak are probably due to the fact that the dead weight is not placed perfectly instantaneous due to the set up. The displacement generated reaching the peak is a combination of the actual starting value of the LVDT and the instantaneous elastic response of the sample. Unfortunately those two contributions cannot be separated.

3.2.2 Displacement & strain vs time

Commonly, a strain vs time curve shows 4 different regimes (see Fig. 19a). There is an instantaneous elastic response (i.e. where the curve follows the y-axis). This is followed by a primary/transient regime, in which the strain rate decreases, until creep will accumulate more steadily and (quasi-) steady state creep is reached (Fossen, 2010; Poirier, 1985). Tertiary creep is when microfracturing and/or recrystallization causes an increase in strain rate, which ends when a macroscopic fracture develops (Fossen, 2010). The displacement data is the direct measurement and a general curve of displacement with time is shown in Figure 20a. This data was converted into strains and a typical strain versus time curve is shown in Figure 20b.

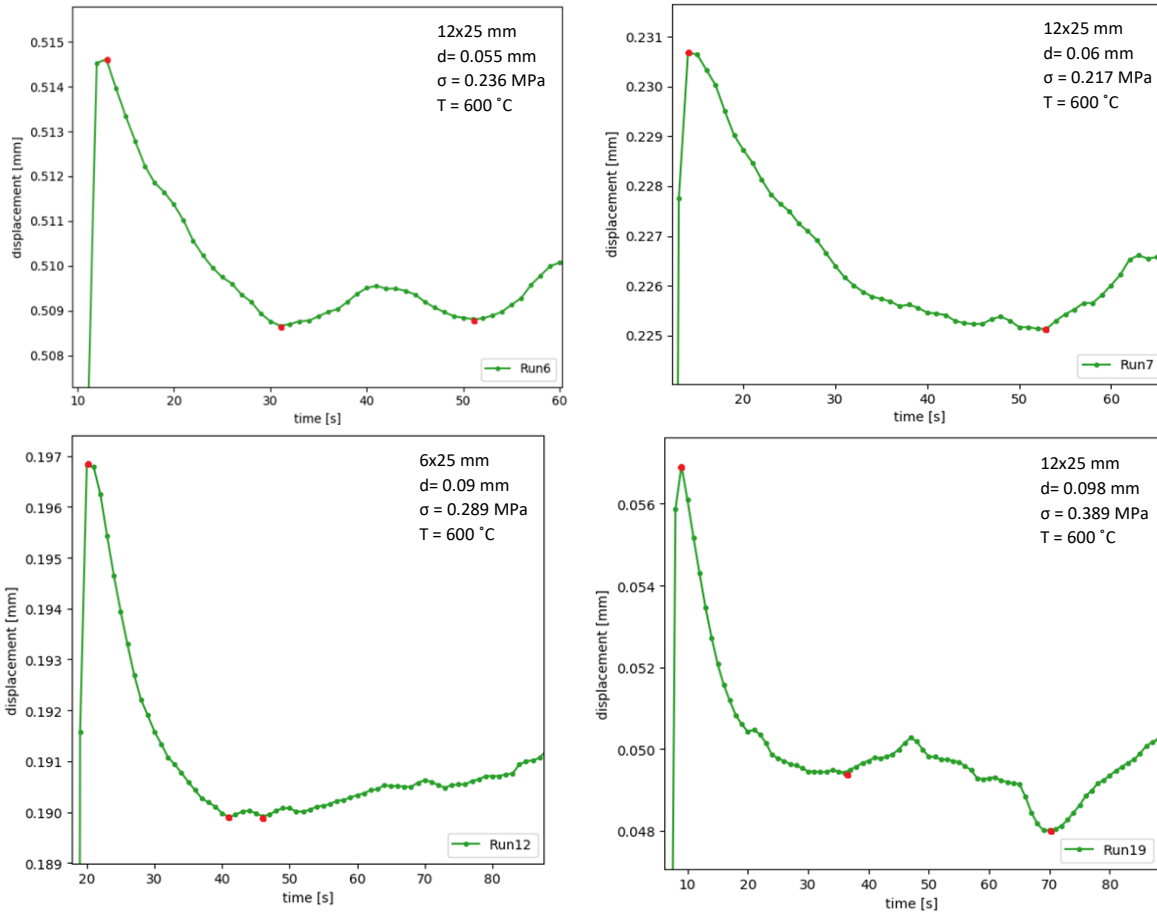


Figure 17 Thermal cooling examples.

Experiment	Start	Peak	1e low	Lowest (= "arbitrary" start)	End	"arbitrary" end
1	12	15	22	53	183838	71200
4	10	15	35	65	319728	175000
5	18	21	-	47	341759	41000
7	12	14	-	53	422192	164939
8	11	14	-	47	345237	256000
6	10	13	31	51	189959	-
11	8	10	24	38	162565	-
10	8	10	-	20	156064	-
21	9	12	-	42	1558058	165000
19	7	9	36	70	397285	-
25	6	8	-	25	2146900	-
12	18	20	40	46	491844	-

Table 4 Thermal cooling data overview.

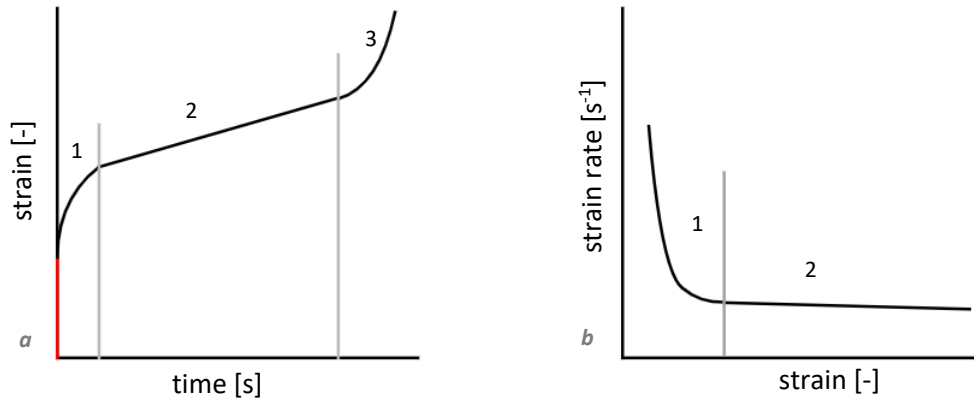


Figure 19 a) Common strain vs time curve, showing the instantaneous elastic response (red), the transient creep regime (1), the (quasi)steady state regime (2) and the tertiary regime (3), b) common strain rate vs strain curve showing the transient regime and the (quasi)steady state regime (2).

Following the division in regimes made in Figure 19a, the curves in Figure 20 can be divided into two parts, a transient regime and a quasi-steady state regime. In the transient regime, displacement/strain is accumulating fast, but accumulation slows down with time at a decaying pace. As it reaches a quasi-constant accumulation, the regime goes towards quasi-steady state. Full steady state and the successive tertiary creep regime are not achieved in our tests. The (almost) instantaneous response of the material is not included in the graphs, as the first seconds of the experiments are excluded from further calculations (see Section 3.2.1 on thermal cooling).

The repeatability of experiments is tested by plotting experiments with roughly the same stress on a strain versus time plot and comparing their achieved strains (see Fig. 20 a and b). There is a 0.15% range in the strains achieved after 40000s in Figure 21a as well as Figure 21b. It is interesting to notice that when the experiments ran longer the range in achieved strains becomes smaller (0.05% in Figure 21b after 160000 s). It is clear that higher stresses lead to higher strains for a given amount of time. When experiments are plotted with increasing stresses (see Fig. 22a), it is evident that higher stresses give rise to higher initial strain rates.

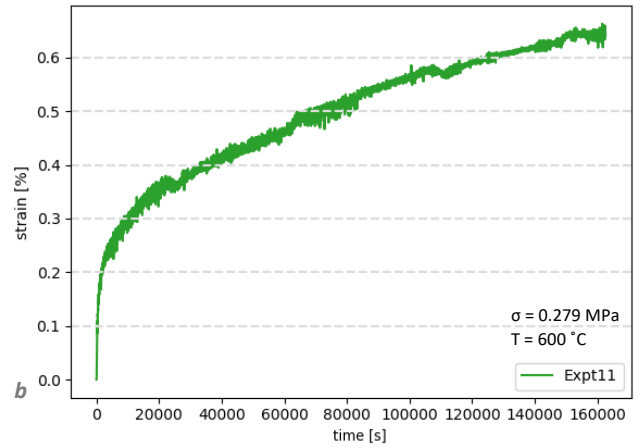
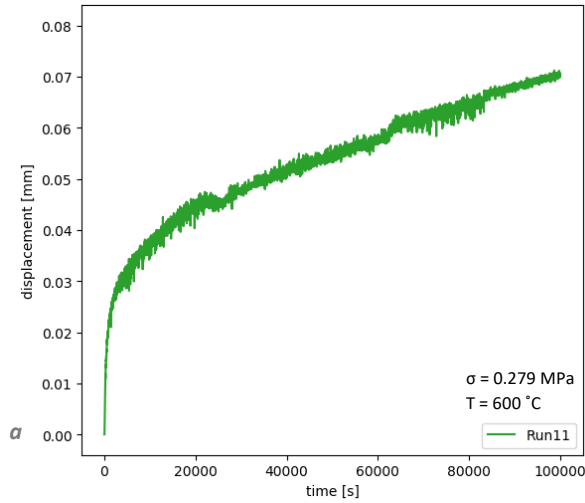


Figure 20 a. displacement vs time for experiment 11, b. strain vs time for experiment 11

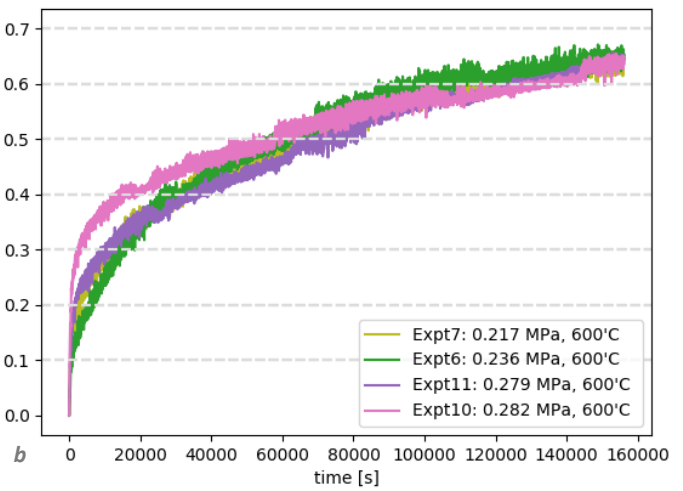
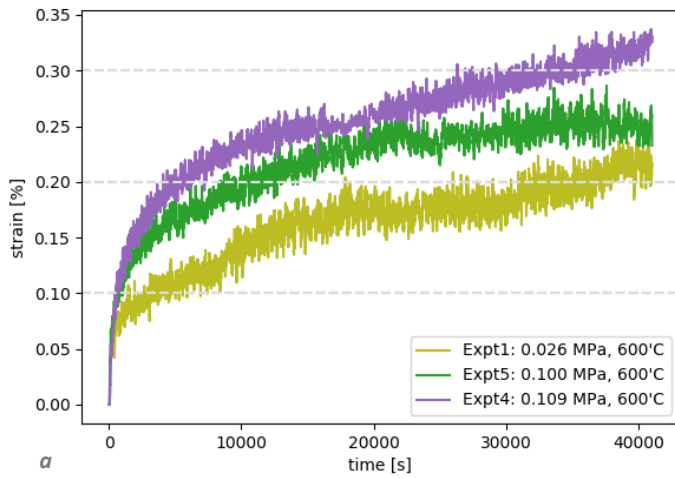


Figure 21a strain vs time (low stress experiments), b. strain vs time (high stress experiments)

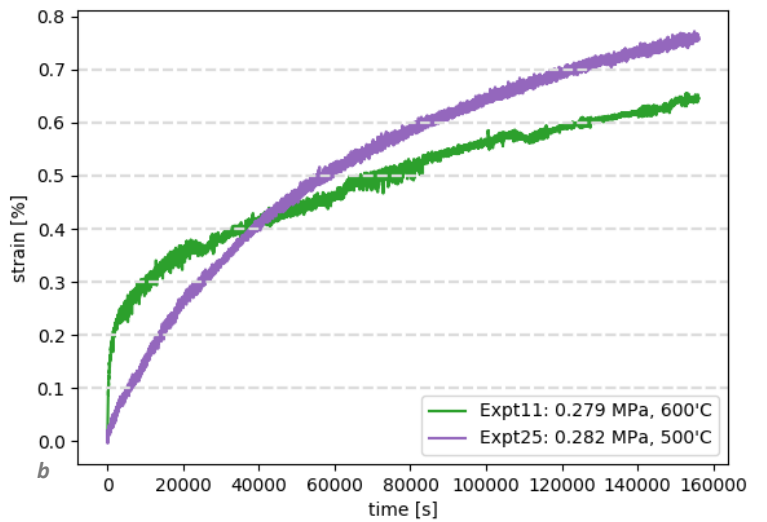
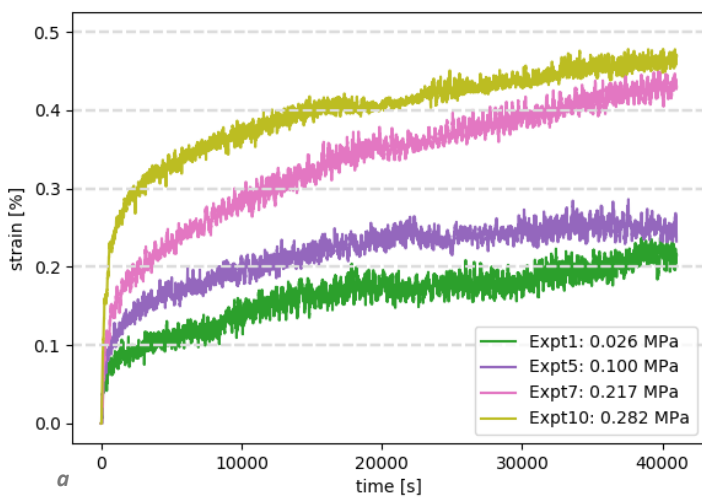


Figure 22a compare low stress and high stress, b. compare temperatures

Since we only conducted one experiment at a different temperature with a continuous displacement curve, only a crude estimate can be made of the influence of temperature on the displacement and strain. A lower temperature gives rise to slower initial strain rates, and a lower decay rate (see Fig. 22b). The strain accumulated within this time interval is higher for the experiment with the lower temperature and lower initial strain rate.

3.2.3 Strain rate vs time & strain

Commonly, a strain rate vs strain curve has two regimes as shown in Figure 19b. In the transient regime in the strain rate slows down with time, i.e. the sample is accumulating strain at a decaying pace. With time the strain rate will no longer decrease with increasing strain and a quasi-steady state regime is reached. Following the division in regimes made in Figure 19b, the curves in Figure 23c can be divided into two parts, a transient regime and at strains above 1% a quasi-steady state regime. The decision to fit small straight lines to the data (see Fig. 23a, the colored segments are fitted to the data curve) to obtain strain rates (see Section 2.6), gives the strain rate plots their plateau appearance (see Fig. 23b). Figure 24-27 shows the curves for other experiments. The creep rates for most experiments start around $8 \times 10^{-6} \text{ s}^{-1}$. It should be noted that this starting rate is affected by our choice for a starting point. The lower limit attained is around $1 \times 10^{-8} \text{ s}^{-1}$ to $9 \times 10^{-9} \text{ s}^{-1}$ for the experiments with a temperature of 600° . For the experiment done at 500°C this limit of the strain rate is lower $\sim 3 \times 10^{-10} \text{ s}^{-1}$.

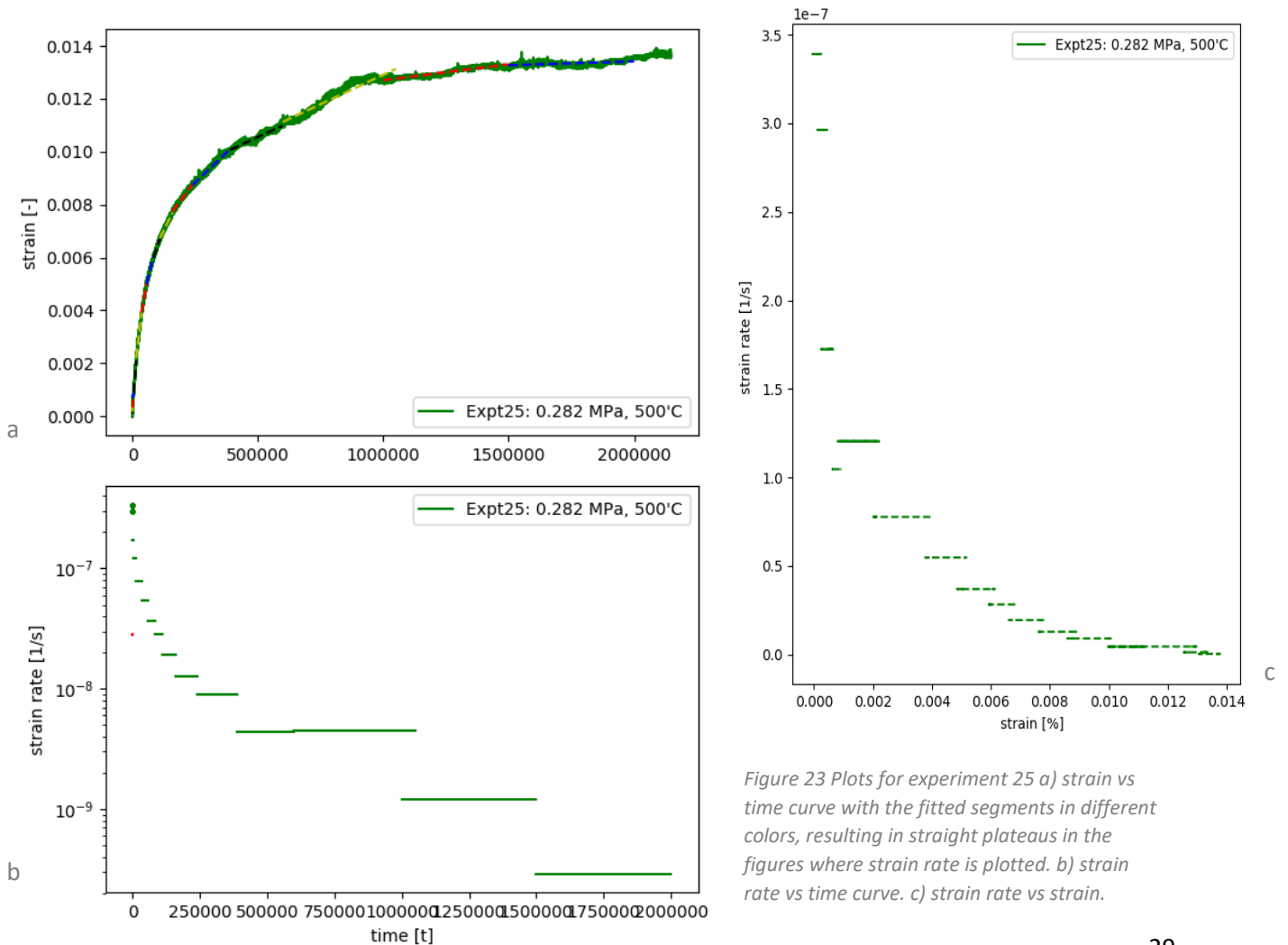


Figure 23 Plots for experiment 25 a) strain vs time curve with the fitted segments in different colors, resulting in straight plateaus in the figures where strain rate is plotted. b) strain rate vs time curve. c) strain rate vs strain.

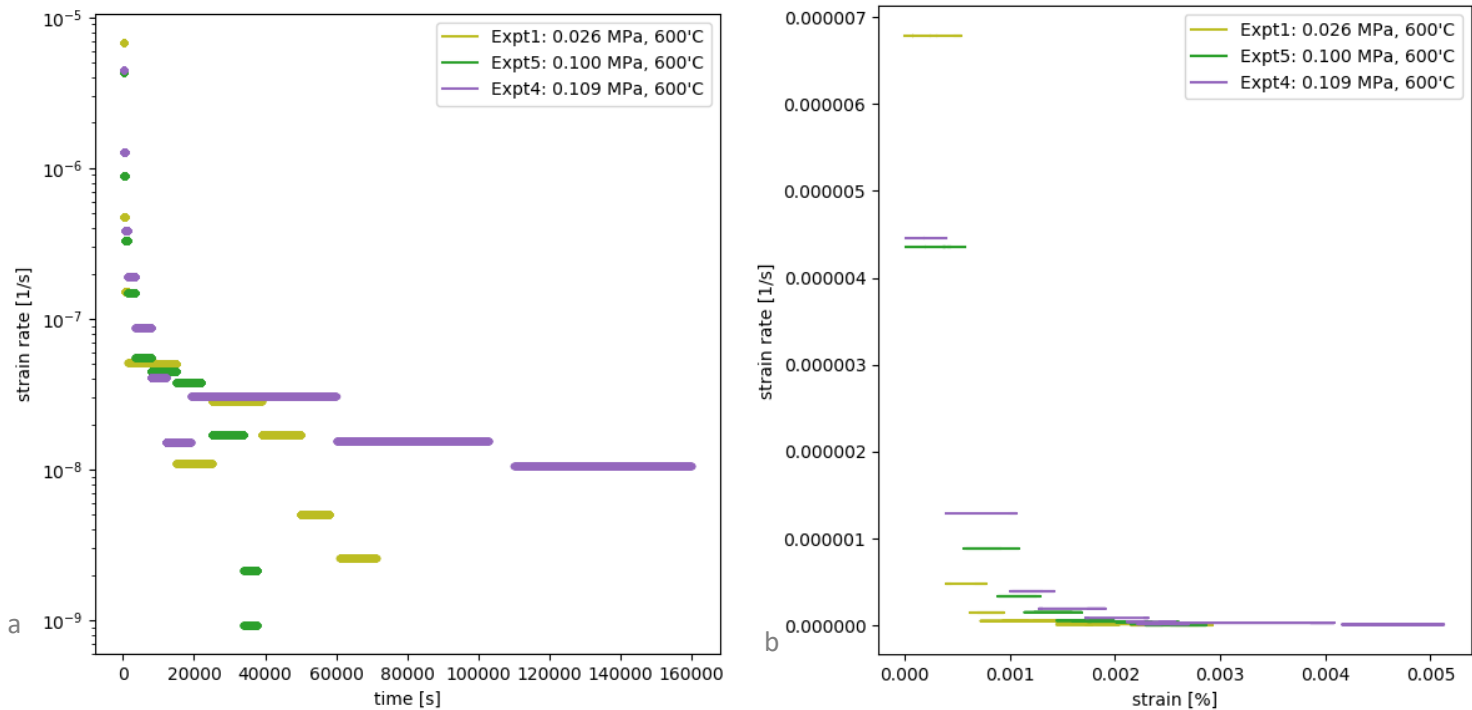


Figure 24 Stresses below 0.1 MPa a) strain rate vs time, b. strain rate vs strain

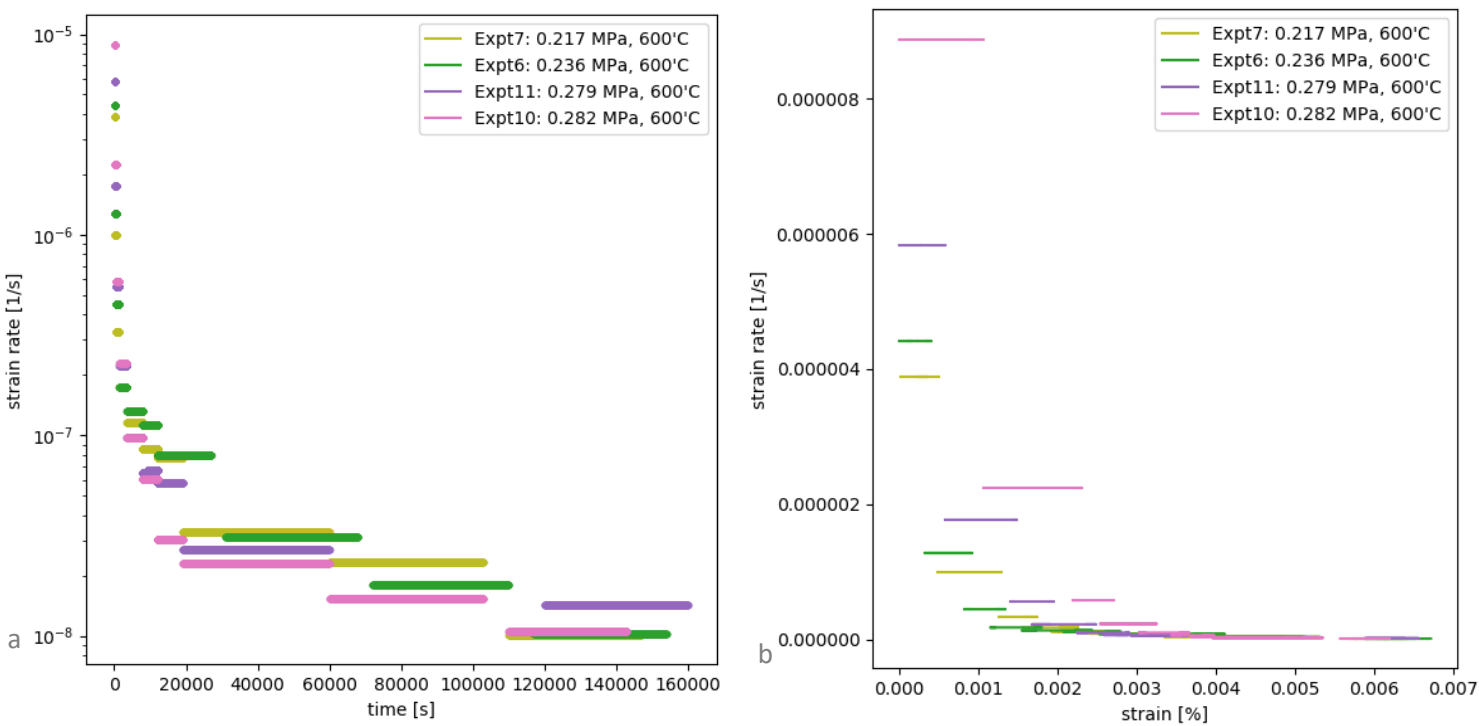


Figure 25 Stresses between 0.2 and 0.3 MPa a) strain rate vs time, b. strain rate vs strain

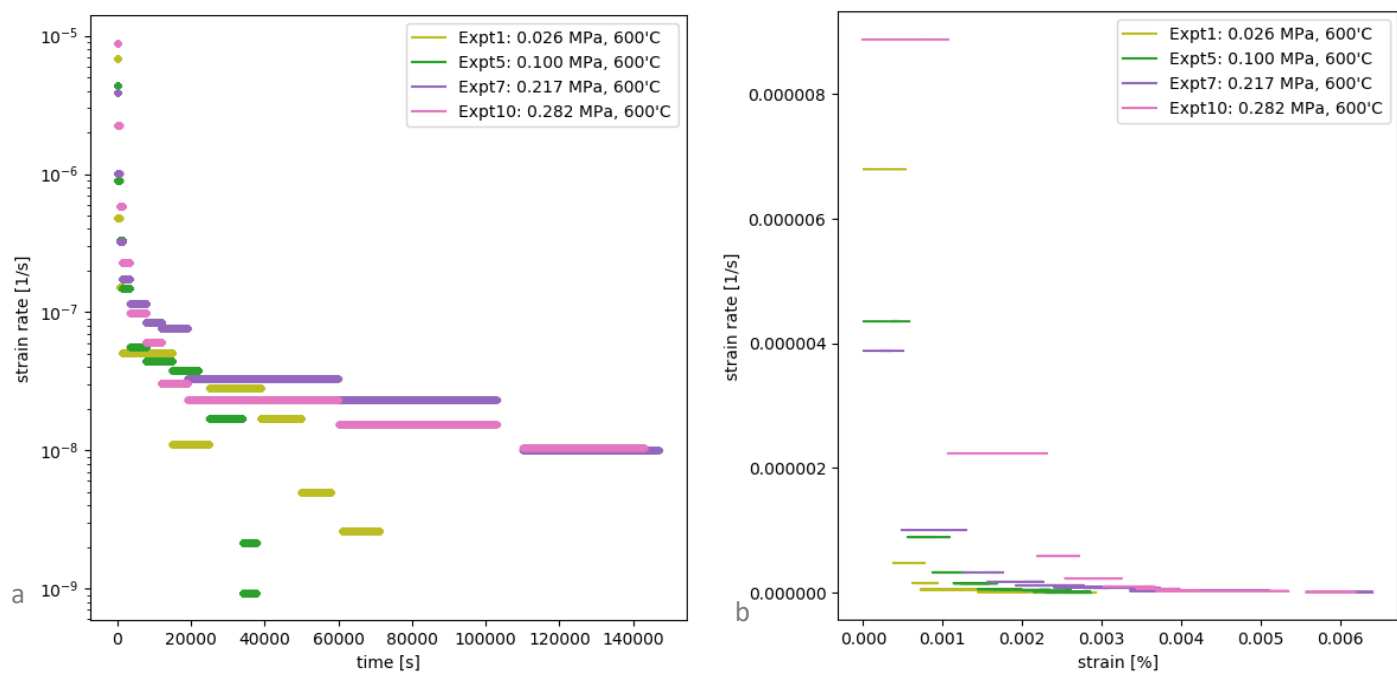


Figure 26 Low stresses compared with high stresses. a) strain rate vs time, b) strain rate vs strain

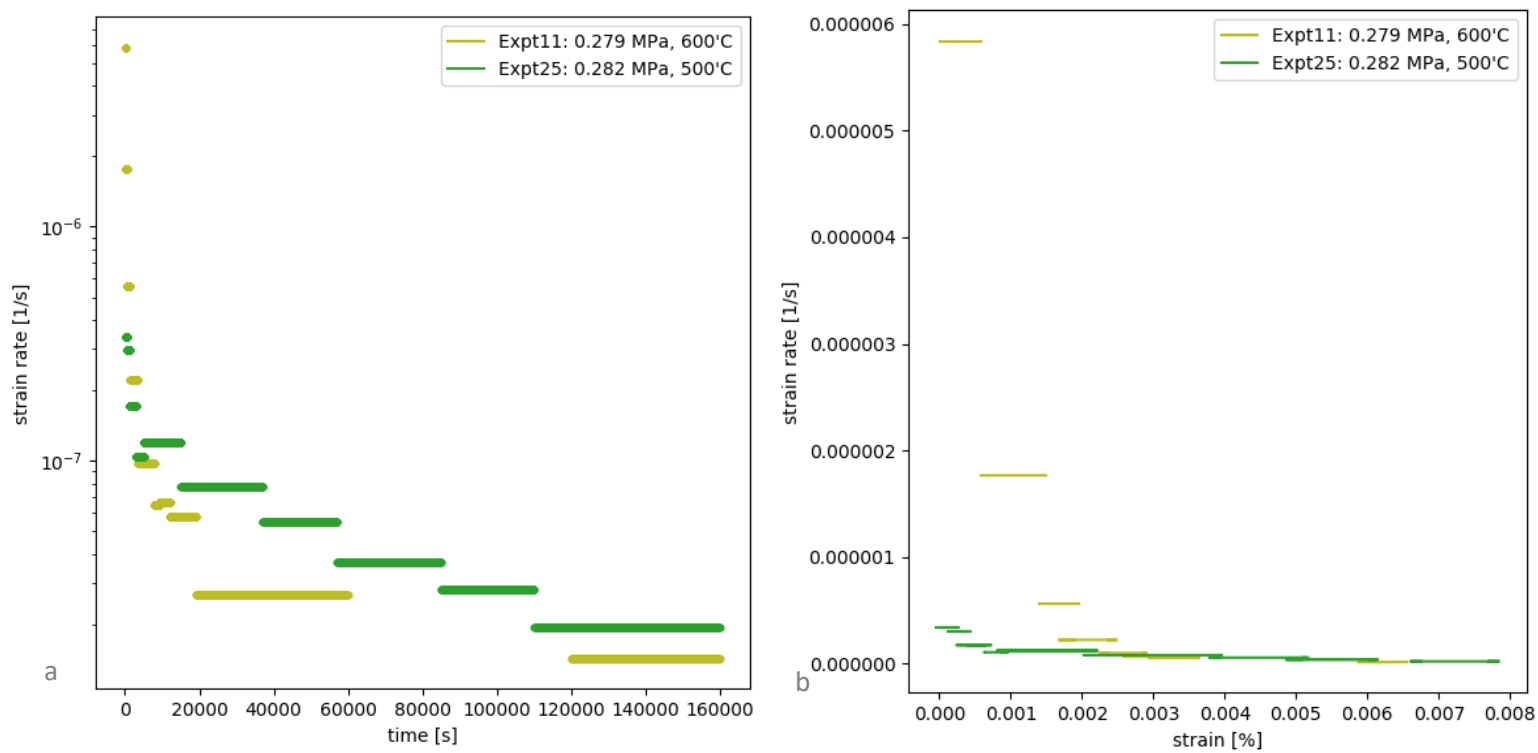


Figure 27 Temperatures compared a) strain rate vs time, b) strain rate vs strain

The set of experiments performed with low stresses (see Fig. 26a) shows a little more scatter than the experiments performed with higher stresses (see Fig. 27b). Experiment 1 and 5 (low stresses) do not follow the trends displayed by the other experiments and do not achieve quasi-steady state.

Within a single experimental run the strain rate is related to the strain by a strain exponent of -2 (see Fig. 28 & 29)

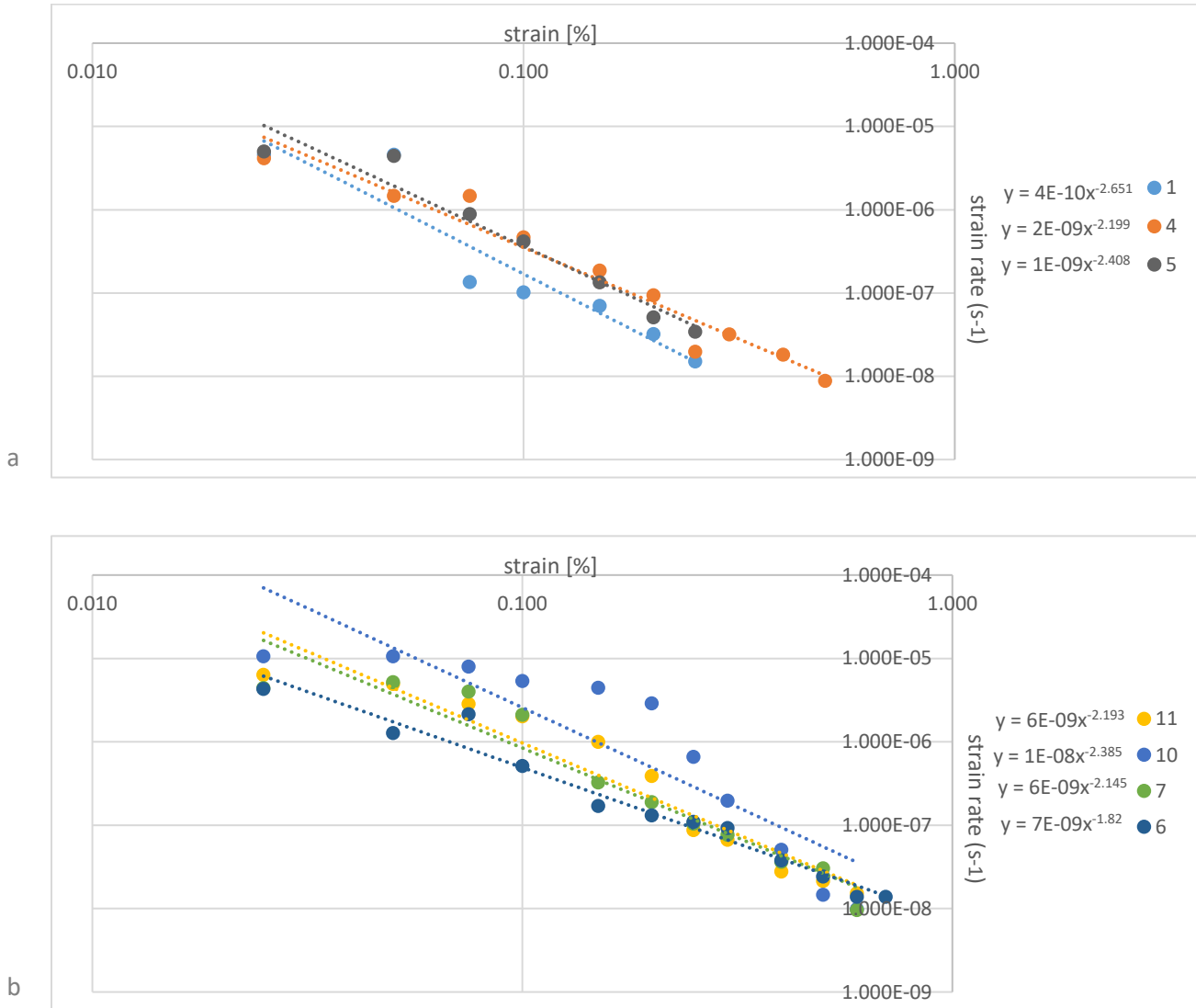


Figure 28 Experiments done at 600°C, strain vs strain rate with a power law fit a) stresses smaller than 0.1 MPa, b) stresses between 0.2-0.3 MPa.

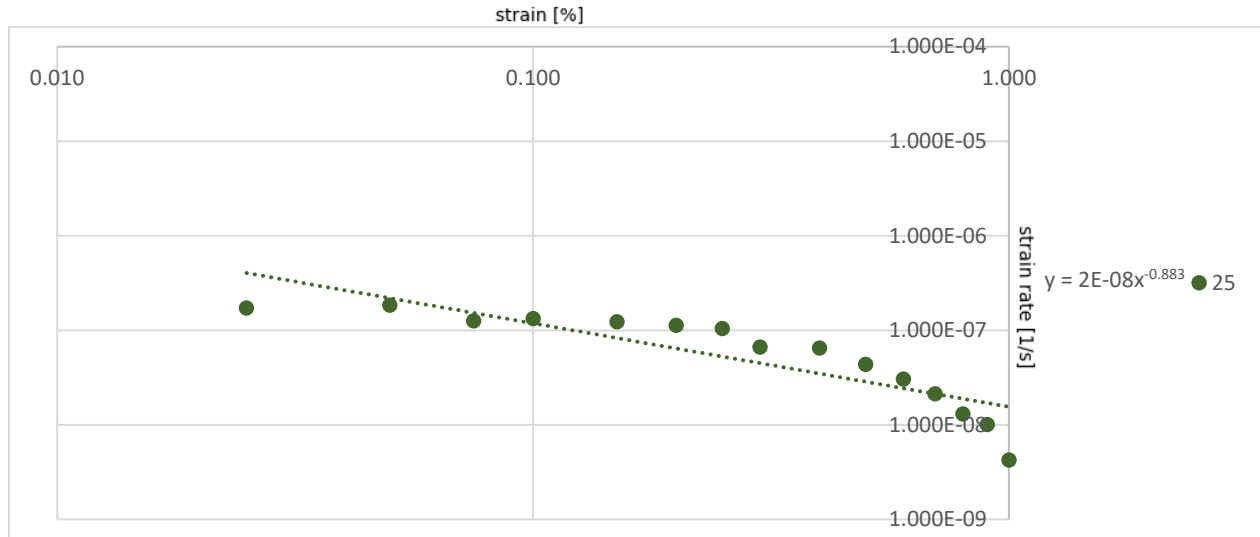


Figure 29 Experiments 25 done at 500°C strain vs strain rate with a power law fit

3.2.4 Effect of ambient temperature on displacement

The temperature was measured at two different locations during single experiments. One temperature is measured close to the sample, and the other just outside the oven chamber (see Fig. 13). The temperature in the oven chamber is fairly constant (see Fig. 30a), while the one outside the chamber seems to display a day-and-night fluctuation (see Fig. 30b). The displacement fluctuates with temperature due to the thermal expansion of the kanthal wire (see Section 3.2.). At the beginning of the experiments the displacement is large enough to obscure this correlation, but later in the experiments, the displacement curve shows a very close correlation to the outside temperature (see Fig. 31).

Since it is a fluctuation of the kanthal wire length, the absolute fluctuation in mm would be roughly the same for every experiment. The strain fluctuation would not be exactly the same, but close. The strain fluctuates within $\pm 0.01\%$ absolute value (see Fig. 32a). This corresponds to a relative fluctuation of around 50% of our smallest selected strain of 0.025%, and 2% for a strain of 0.6%. However, the fluctuation is negligible if the strain/strain rate is averaged over a time interval of at least a few wavelengths. A wavelength of 400s was found (see Fig. 32b).

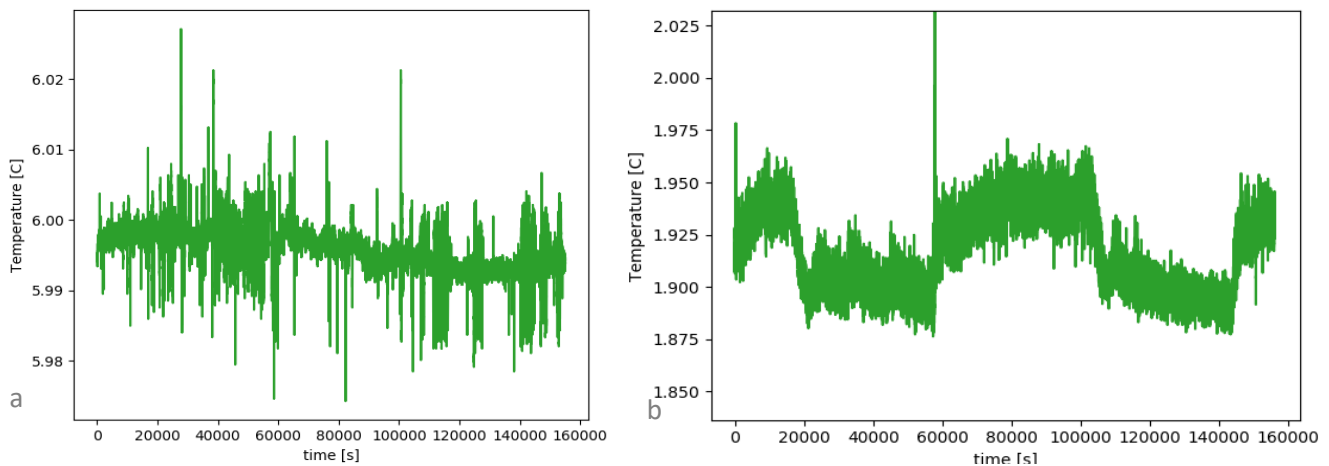


Figure 30 a) The temperature in the oven chamber is fairly constant, b) the one outside the chamber seems to display a day-and-night fluctuation

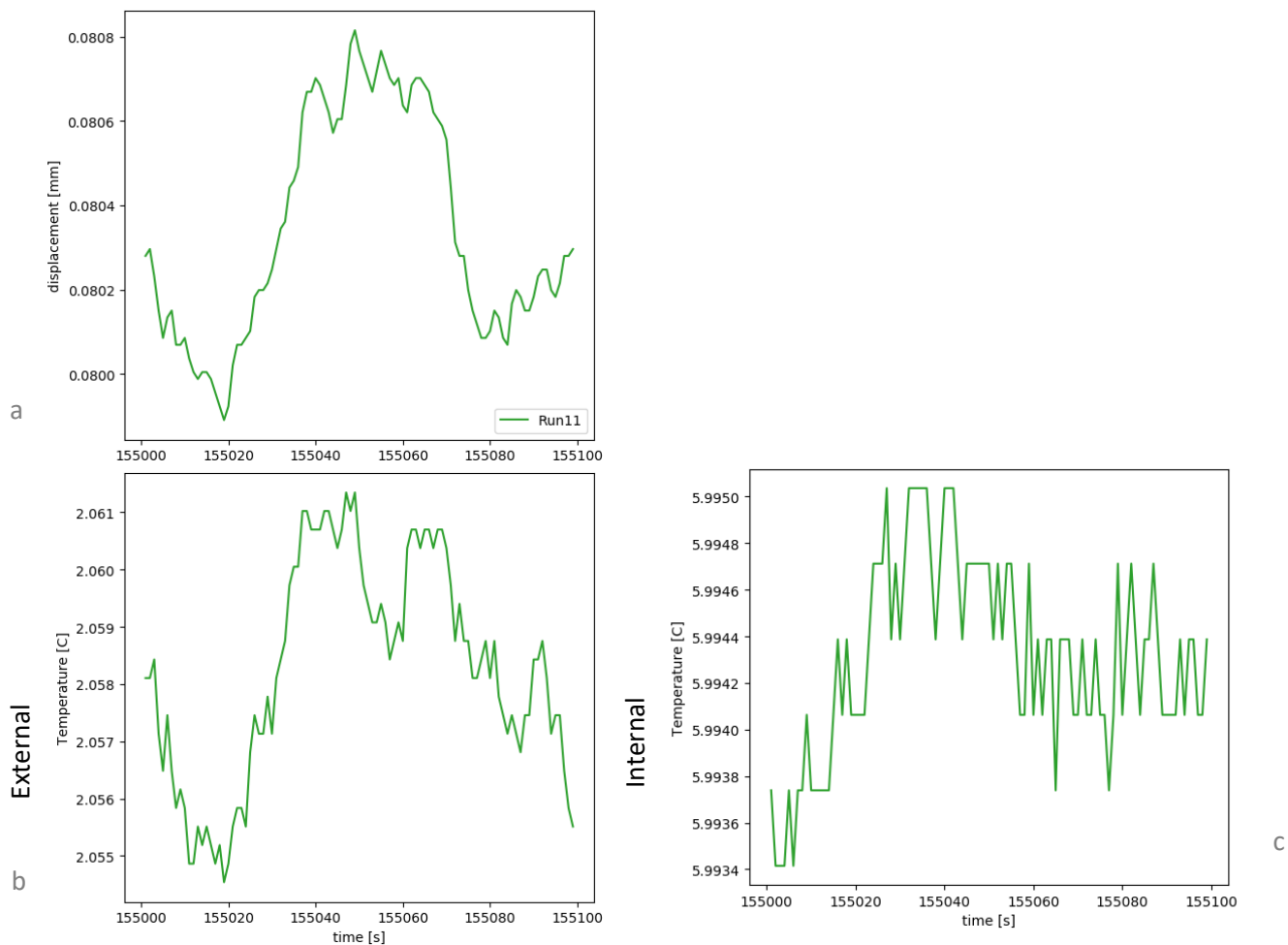


Figure 31 For experiment 11 a) displacement vs time, b) In oven temperature with time, c) out of oven temperature vs time

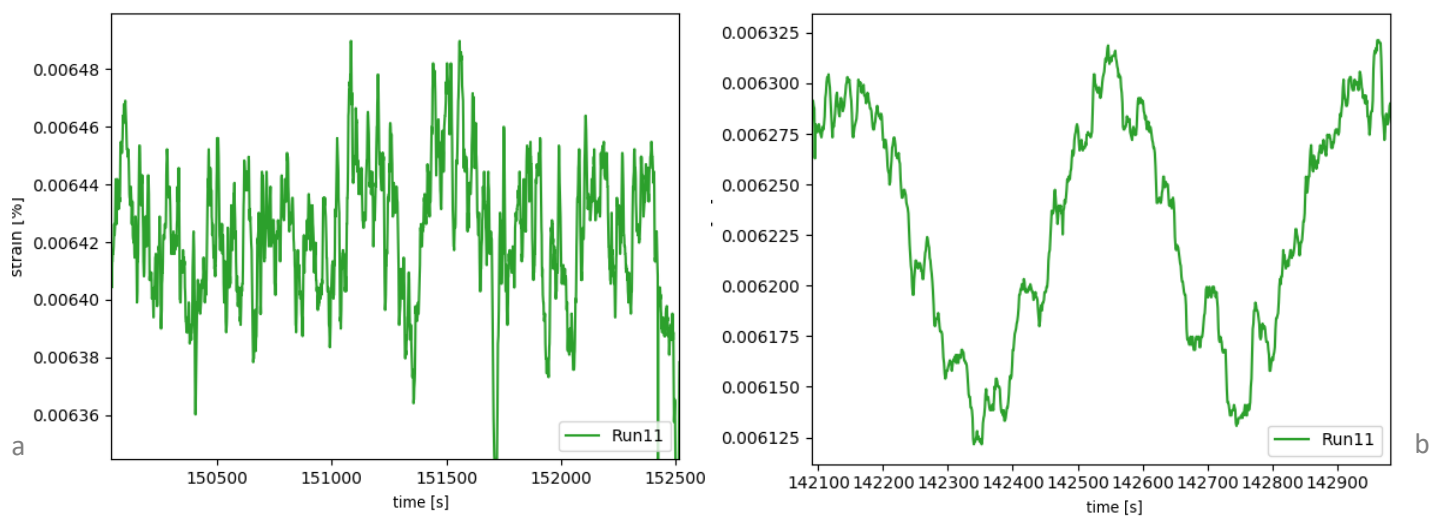


Figure 32 a) strain vs time to determine amplitude of fluctuations, b) strain vs time to determine wavelength of the fluctuations.

3.3 Flow law parameter values

3.3.1 The stress exponent, n

Figure 33 shows the plot of strain rate at given values of strain versus applied stress on a logarithmic scale. A power law trend line is fitted to the data. The best-fit exponent represents the stress exponent n . The plot can be divided into four regimes. For very low strains (0-0.05%) the stress exponent is around 0. For low strains (0.08-0.25%) the stress exponent is around 1. For medium strain (0.3-0.6%) the stress exponent is around 0.8. For high stresses (0.7-0.8%) the stress exponent becomes 0 once more.

Fig 34 shows the stress exponents for each strain with their allotted error bars.

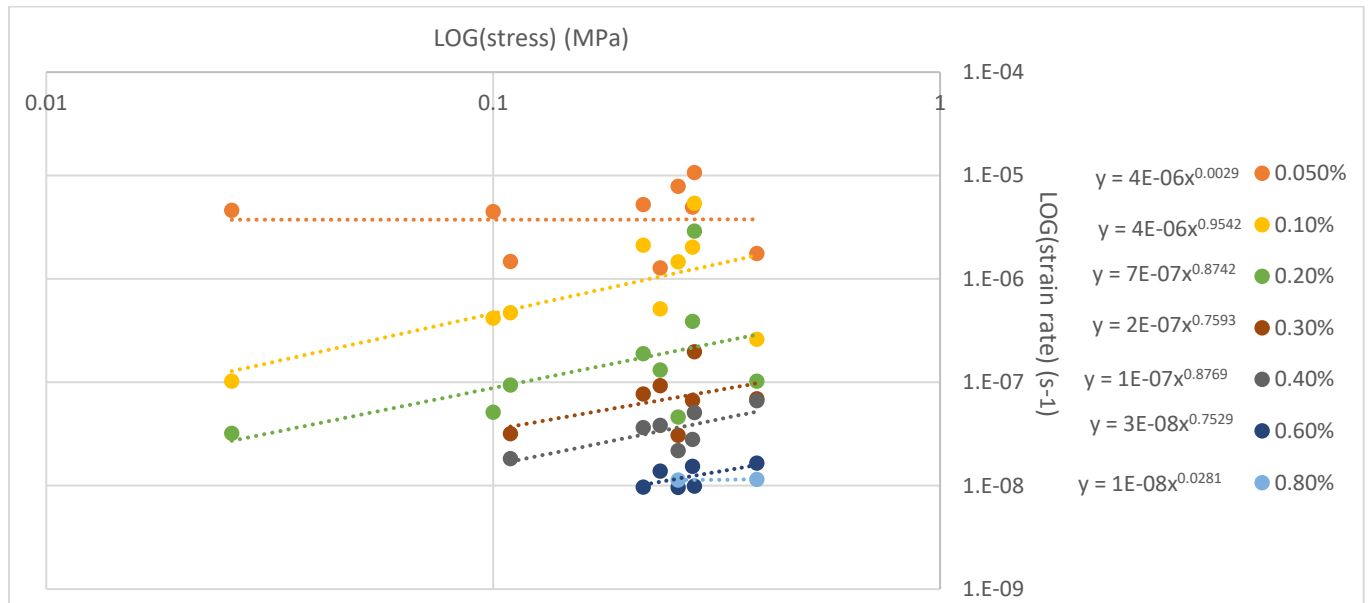


Figure 33 Stress exponent determination

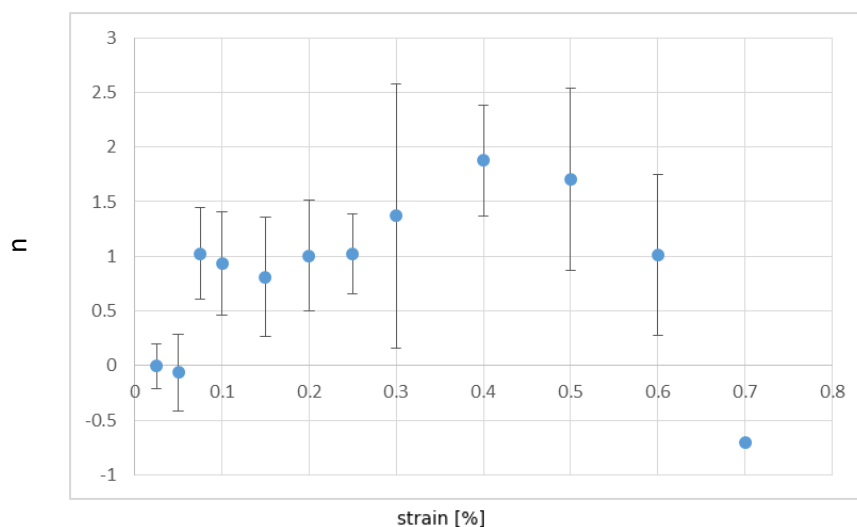


Figure 34 Error bars for the stress exponent n

3.3.2 Exponential factor, α

Figure 35 shows the plot of the natural logarithm of strain rate versus stress. A linear trend line is fitted to the data. The slope of the line represents the stress exponential factor α . The plot can be divided into four regimes. For very low strains (0-0.05%) the exponential factor is around 0. For low strains (0.08-0.25%) the exponential factor is around 6.5. For medium strain (0.3-0.6%) the exponential is around 4. For high stresses (0.7-0.8%) the exponential factor becomes 0 once more.

Fig 36 shows the exponential factor for each strain with their allotted error bars.

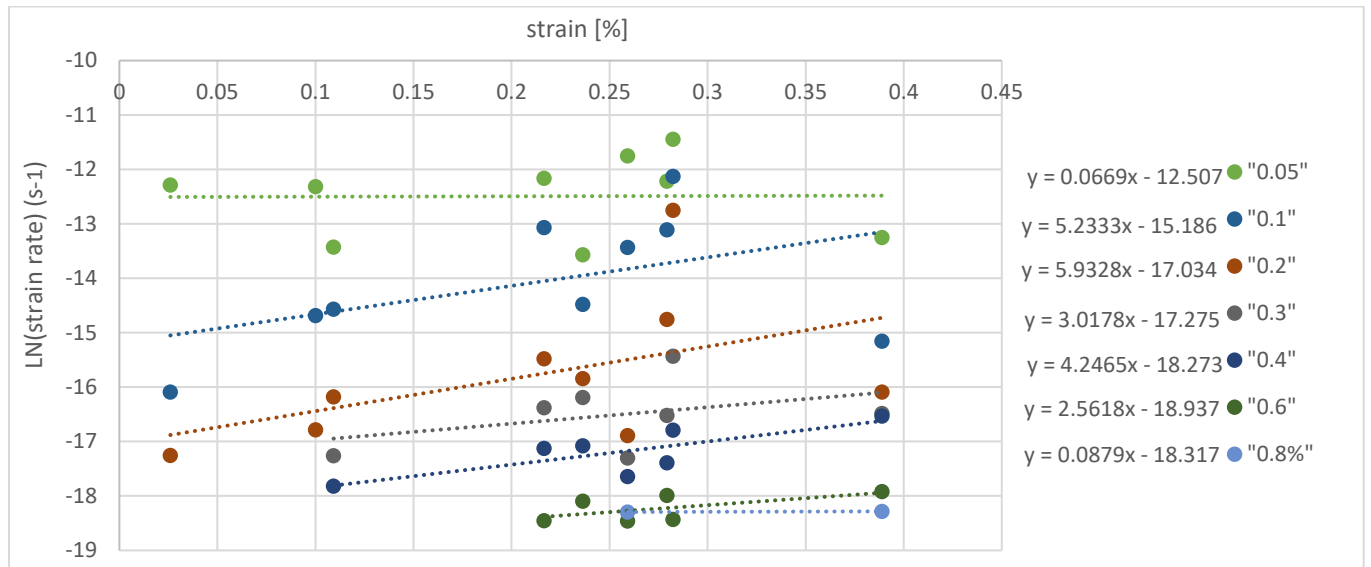


Figure 35 Activation energy determination

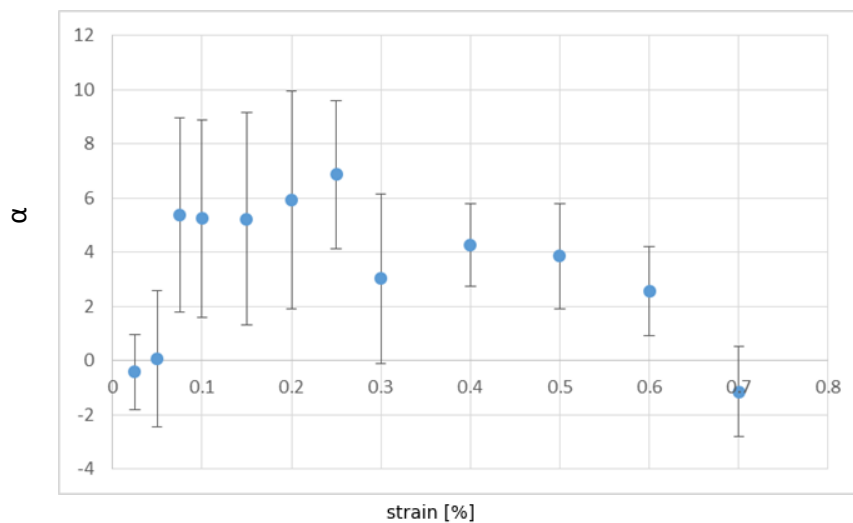


Figure 36 Error bars for the exponential factor α

3.3.3 Activation energy, ΔQ

The activation energy can be found by plotting the natural logarithm of the strain rate against the inverse of temperature. The slope of this curve represents $-\Delta Q/R$. Where ΔQ is the activation energy and R is the universal gas constant. ΔQ is found to be between 206 kJmol^{-1} and -51 kJmol^{-1} (see Fig. 37). The activation energy decreases with increasing strain.

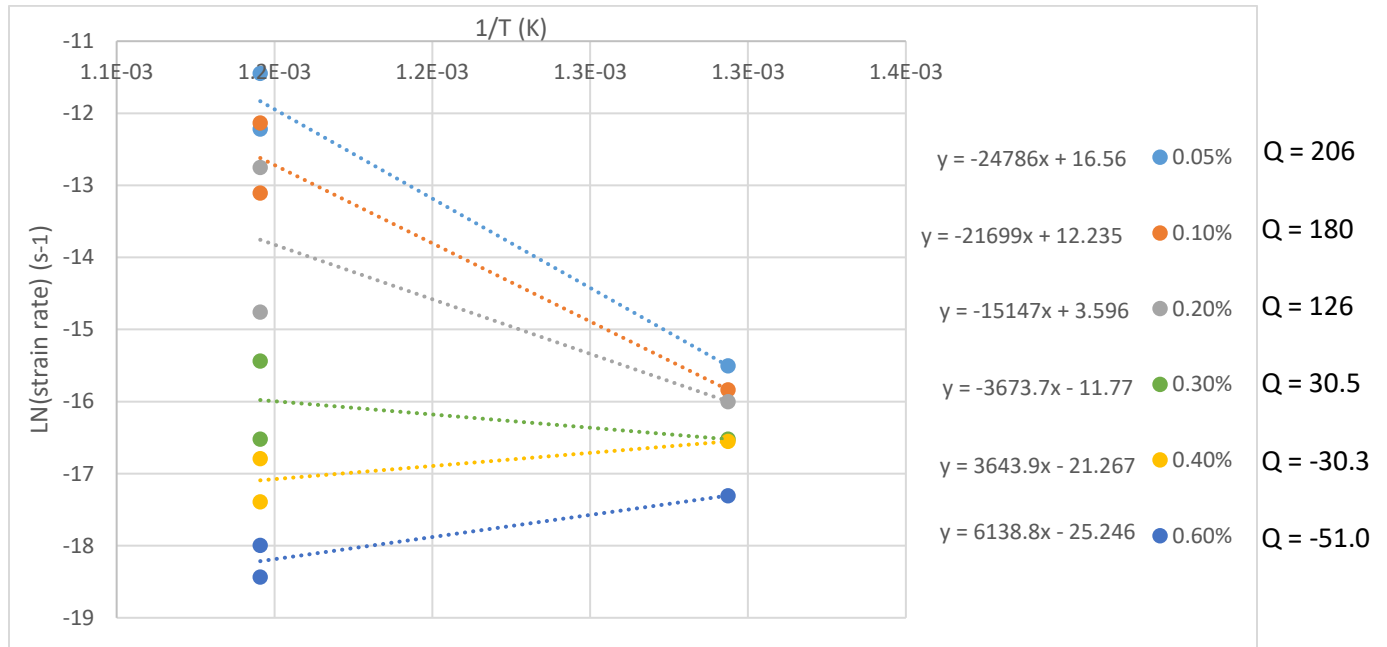


Figure 37 Activation energy determination

3.4 Optical Results

3.4.1 Macroscopic observations

It was expected that the samples would have gained permanent deformation during the experiments, and the retrieved samples would have a visible curvature. However, upon examination these curvatures could not be found. The surface of the samples underwent a striking change in appearance. The samples go from a simple flat surface (see Fig. 38a and Fig. 40), to a surface full of extensive topographic features (see Fig. 38b-d). At 500°C there are no signs of these features, and at 550°C there are only a few visible. The structures follow a crystallographic direction. The main orientation can be predicted to follow the b-axis as determined by optical microscopy.

The sample in Fig. 38 and 39 is sample 17, which had very noisy mechanical data and is therefore not included in that part. In Fig. 39a it can be seen that the deflection of the sample is very small even with an applied stress, and it becomes invisible when the sample is unloaded (see Fig. 39b).

The samples are still a single sheet of muscovite and do not show the fanning reported for the TGA samples in Section 3.1.

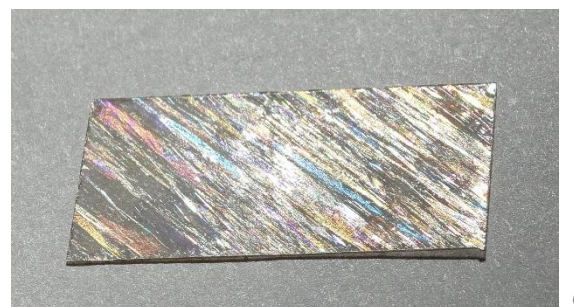


Figure 38 sample 17 (25x12 mm) a. before the experiment, b. after the experiment, c-d. with the light reflecting on the surface

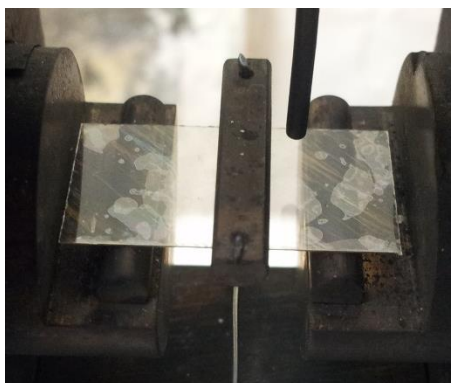
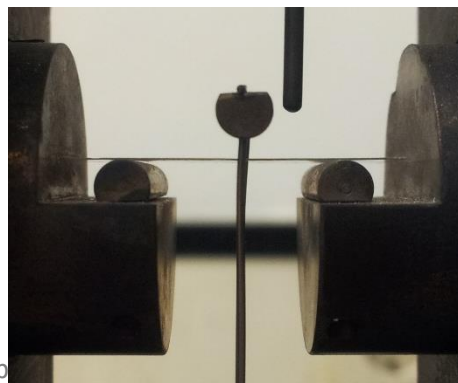
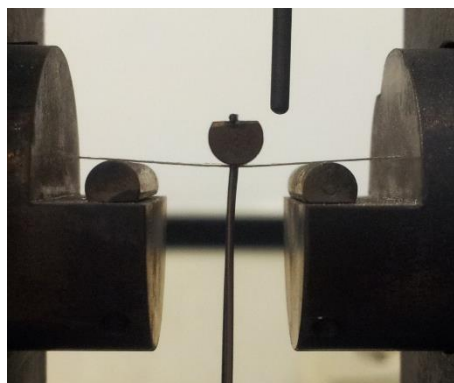


Figure 39 Set up after the experiment with sample 17 (25x12 mm) a. with stress on sample, b. without stress on sample, c. without stress on sample, top view

3.4.2 Microstructural analysis

Figure 41a shows a very regular pattern as observed with the SEM from sample 14 (only heated to 600°). It consists of asymmetric ripples that are cut off by a straight line on the left side. The thickness of the lines varies between 2.4μm and 5μm. The angle between this straight line and the main orientation of the ripples is 41° (see Fig. 41b). To the left of the line, the surface is atomically flat. All ripples have their long sides dipping towards the right. The long side of the ripple and the main orientation make an angle of 15° - 18°. The wavelength of the ripples lies between 17μm and 36μm and their amplitude between 4μm and 10μm. As can be seen in the insets in Fig. 41b, the regular structure is not continuous throughout the entire image. In A one ripple line simply stops. The distance between its neighboring lines is 35μm at the far left side, and 25μm at the far right side. In B and C two ripples on the left side stop, and on ripple line continues to the right, originating between the two stopped ripple lines. In D the “breakdown” of the regular asymmetric ripple pattern can be seen. The lines resemble a boudinage structure and the shape of the individual segments goes toward a starting of dog-bone like shape.

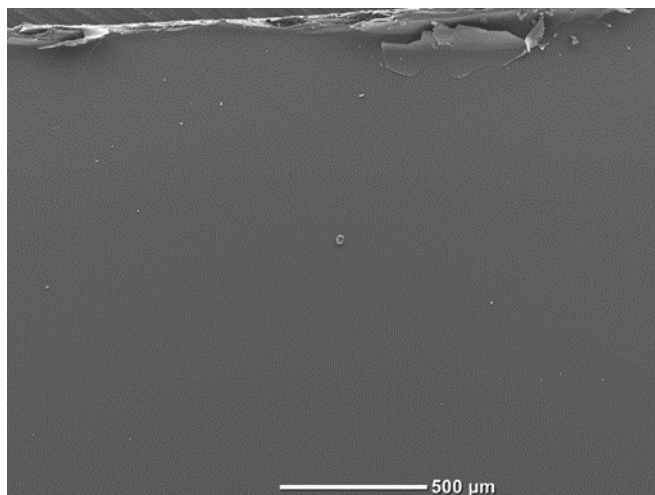


Figure 40 Unheated and undeformed surface

Figure 42 shows the same kind of regular pattern observed with the Leica from sample 19 (heated to 600°C, stress of 0.389 MPa, long side parallel to the microstructures). An additional advantage of the Leica microscope is that it allow for colors to be imaged. The same range of colors seen in Fig. 42 are also macroscopically observed (see Fig. 38). The asymmetric ripples are merged into straight lines, as in Fig. 41, but some continue on both sides of this straight line (see Fig. 42 A) The long side of the ripples in this image is not consistent (see Fig. 42 B, and compare C and D). Some of the ripples are symmetric (see Fig. 42 E). The wavelength and amplitude are not consistent throughout the image. Wavelength varies from 6μm to 40μm, and amplitude varies from 3μm to 20μm. As in Fig. 41, some ripple lines stop, or go from two lines to just one or vice versa (see Fig. 42 F). In Fig. 42 G one ripple line goes to a flat line. In H the ripple line ends in the dog-bone shape. The red angles are ~ 18°, and the top left green angle is 10°. The green angle in the bottom right is part of a cross, where the marked angle is 29°, and the larger angle is 151°. As can be seen just above the cross, there are also a few larger corrugations visible in blue. These structures will be discussed further below.

Figure 43 shows in a few areas the same kind of regular pattern as seen in Fig. 41 and 42 observed with the SEM from sample 11 (heated to 600°C, stress of 0.279 MPa, long side 77° to microstructures). The image shows more straight lines, and ripple lines on different scales (see Fig. 43 A and B). Smallest wavelength is around 8μm, biggest around 85μm. The smallest amplitude is 4μm and the biggest amplitude is 28μm. In the right side of the images there are more dog-bone structures (see Fig. 43 C), as well as some larger dome like structures (see Fig. 43 D). In E the ripple line to a straight line is highlighted, the angle that is make is 167°. Following that line to the top, it once again becomes a ripple line.

To summarize the results described above, there are a few distinguishable microstructures visible in the samples: straight lines, symmetric ripples, asymmetric ripples, starting dog-bone shapes, dog-bone shapes and dome-like structures.

When the structures come across a broken sheet edge, the structure stops at the edge (see Fig. 44). Lower lying sheets do show similar structures and similar orientations. There are no signs of kinking or cracks within the sheets of mica.

The structures seem to be mainly on the near surface, as in scrolling through the sample with the Leica microscope just revealed a few layers with microstructures. The difference in microstructural development in samples that are only heated to 600°C, and the samples that are heated to 600°C and stressed, are not identifiable without an in depth quantitative analysis of the microstructure distribution. There seems to be no difference in the top or bottom of the sample.

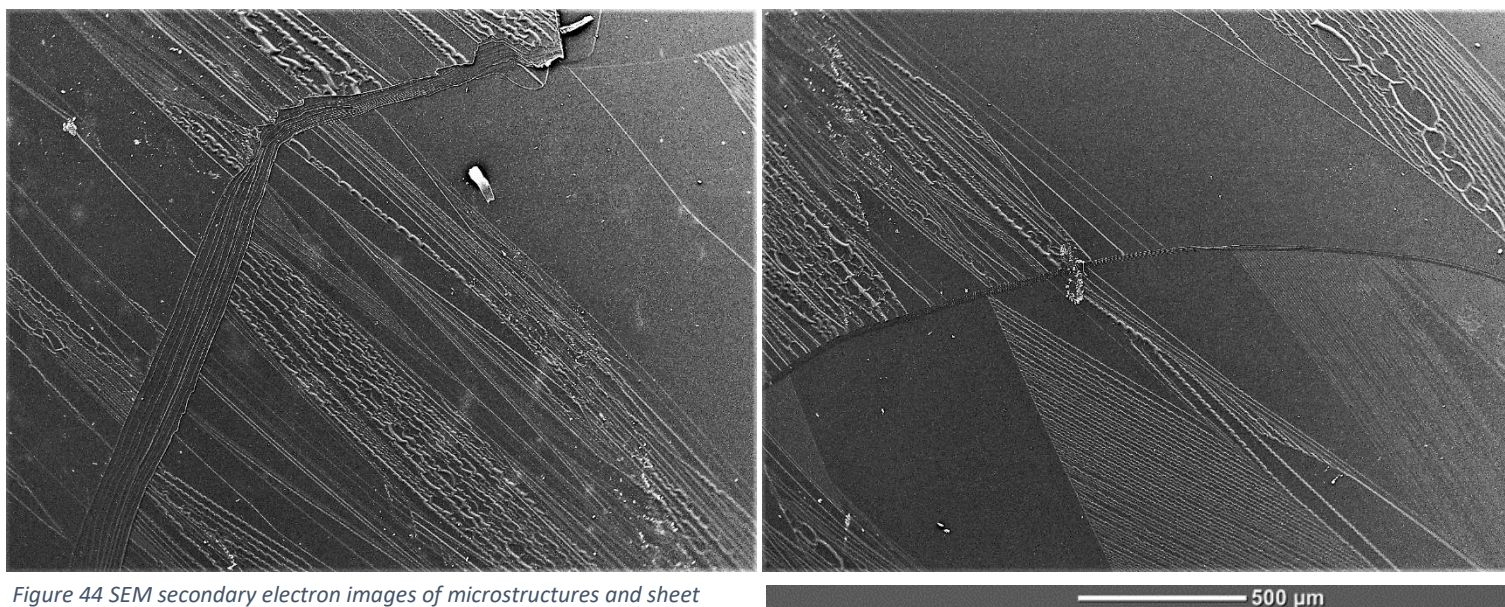


Figure 44 SEM secondary electron images of microstructures and sheet edges.

Figure 45 displays some other features observed with the Leica microscope in sample 19. The rainbow colors are Newton rings and fringes. It is interesting to notice that the microstructures follow the edge of these fringes.

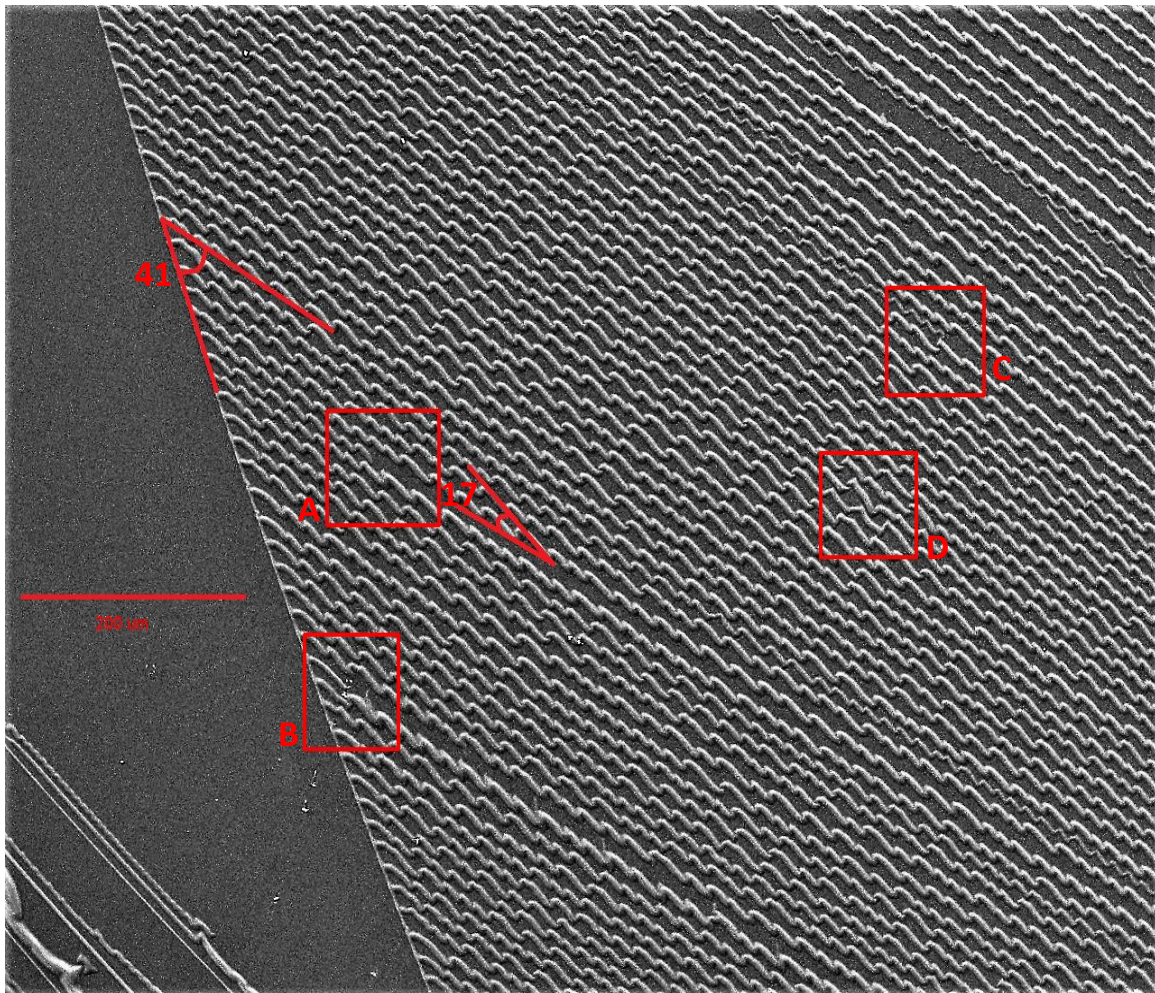
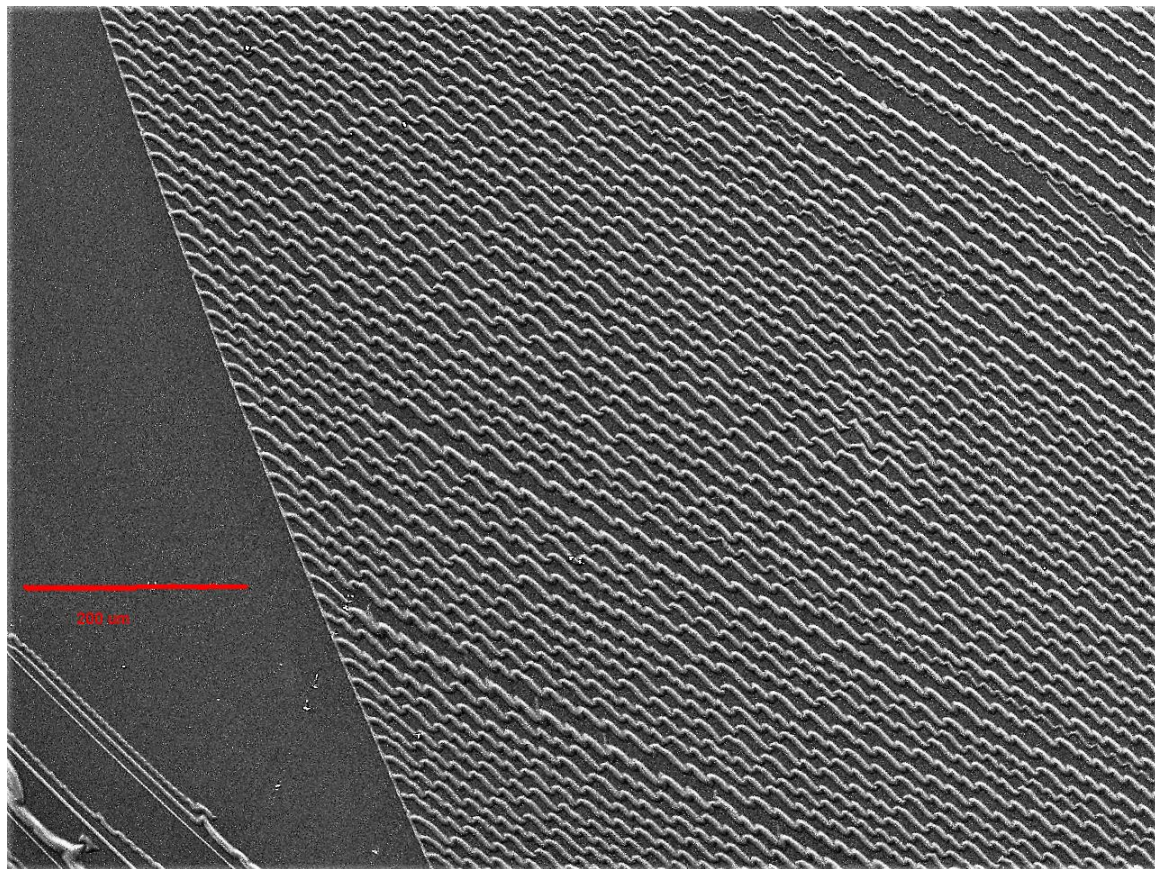


Figure 41 SEM secondary electron image from sample 14 showing a very regular pattern of asymmetric ripples on a μm scale

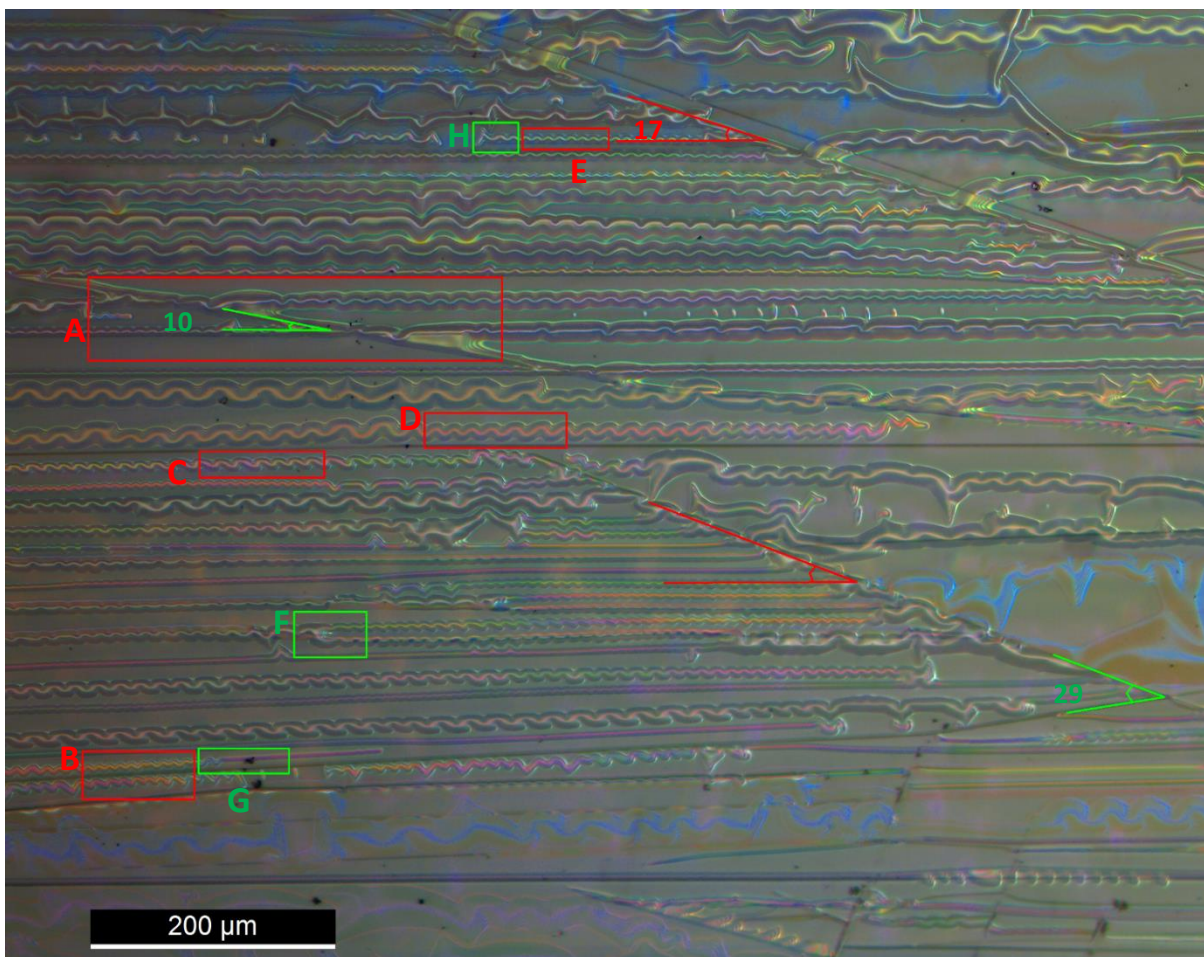
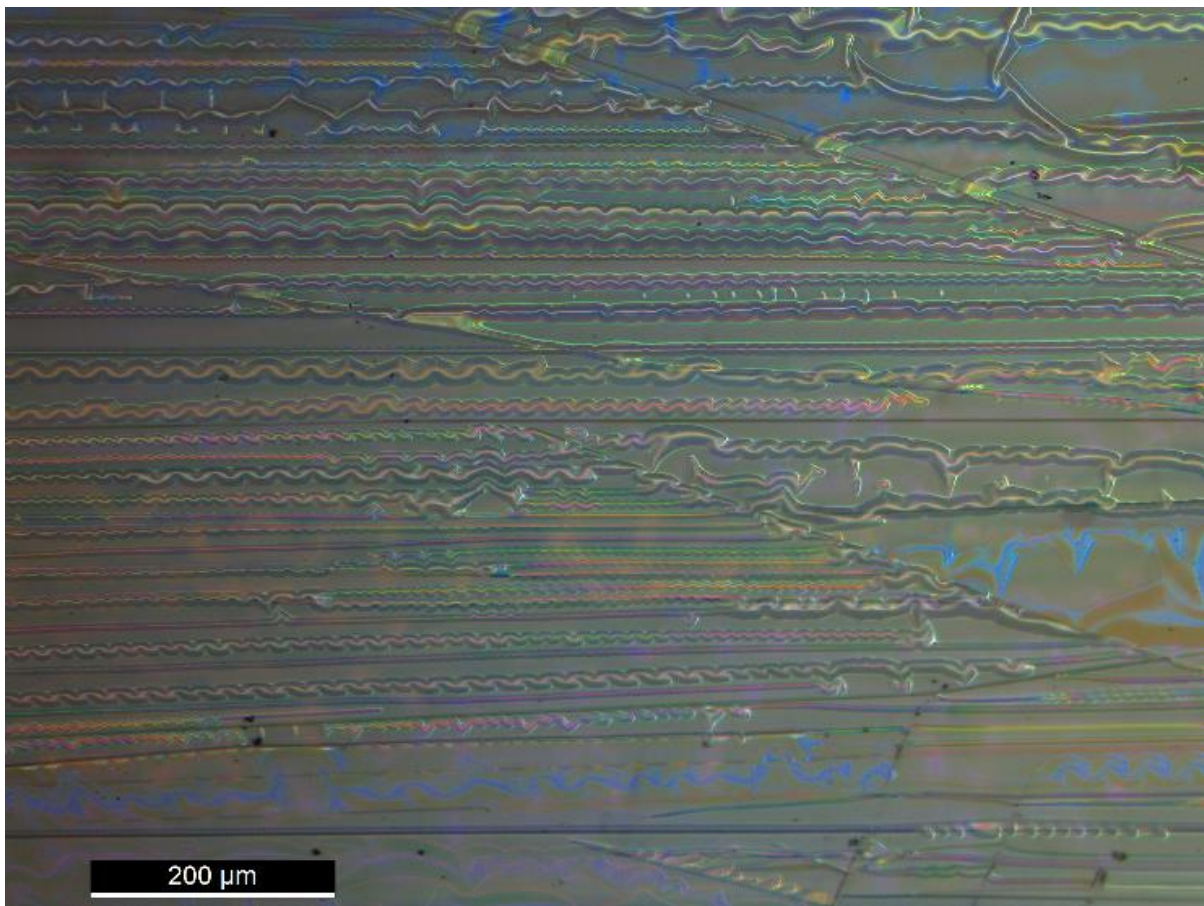


Figure 42 Leica optical microscope image from sample 19 showing an array of colors and microstructures

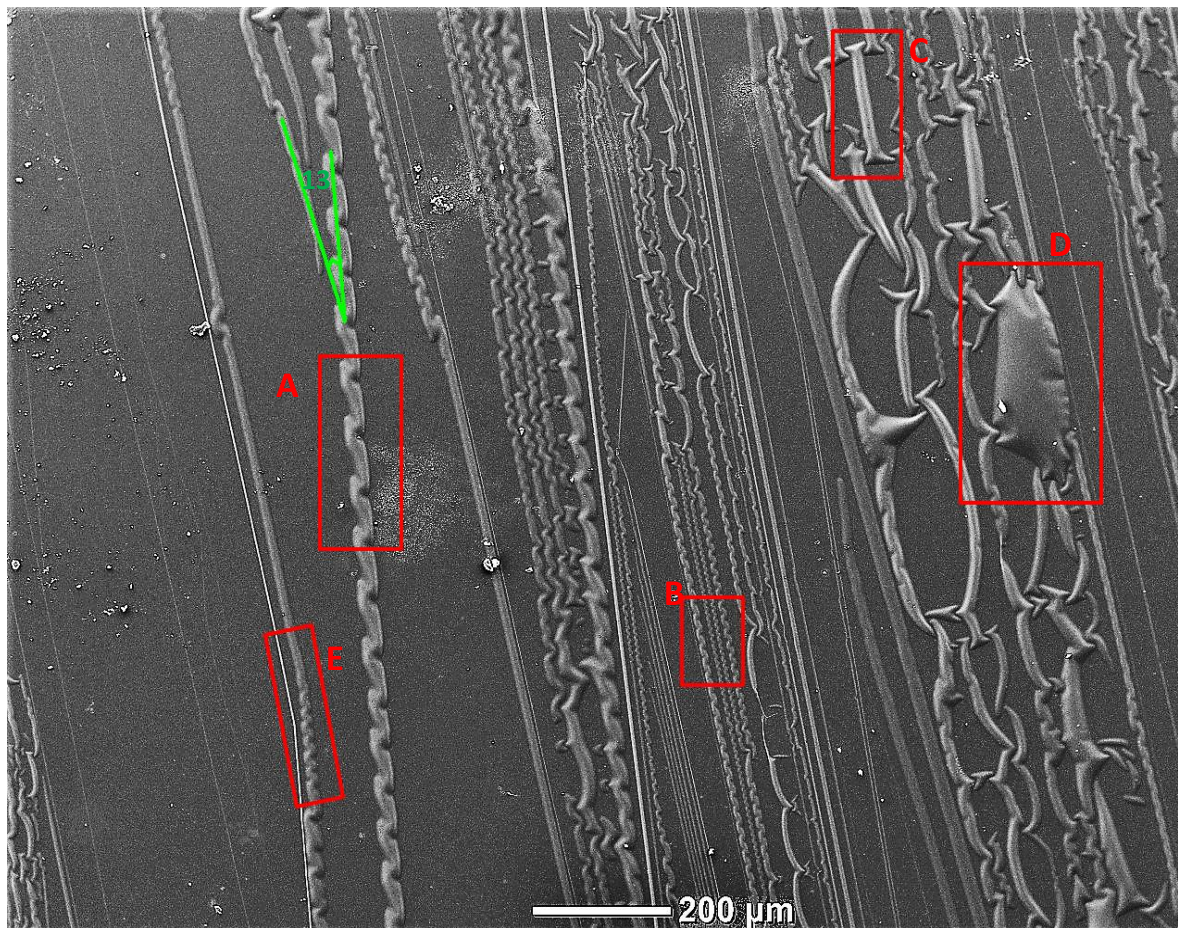
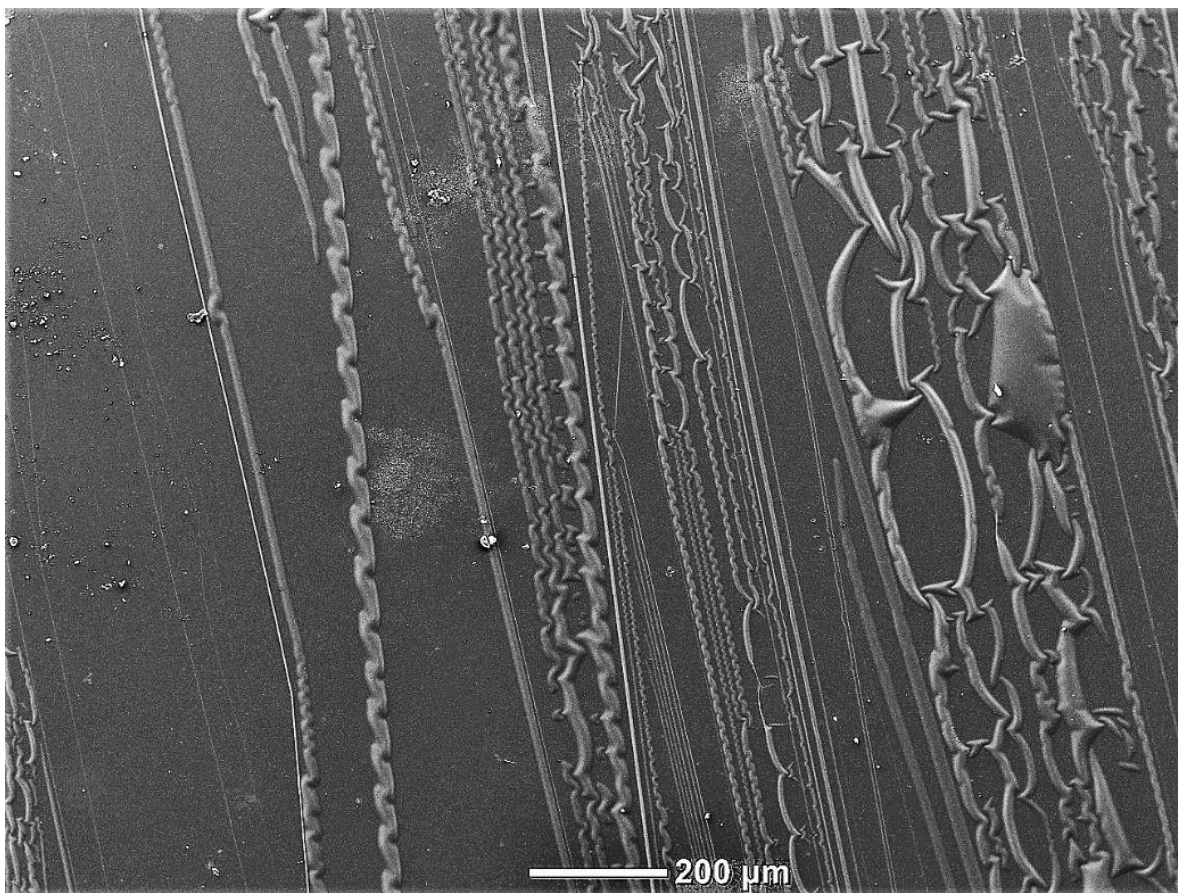


Figure 43 SEM secondary electron image from sample 11 showing an array of microstructures ranging from straight lines (E) to dome-like structures (D).

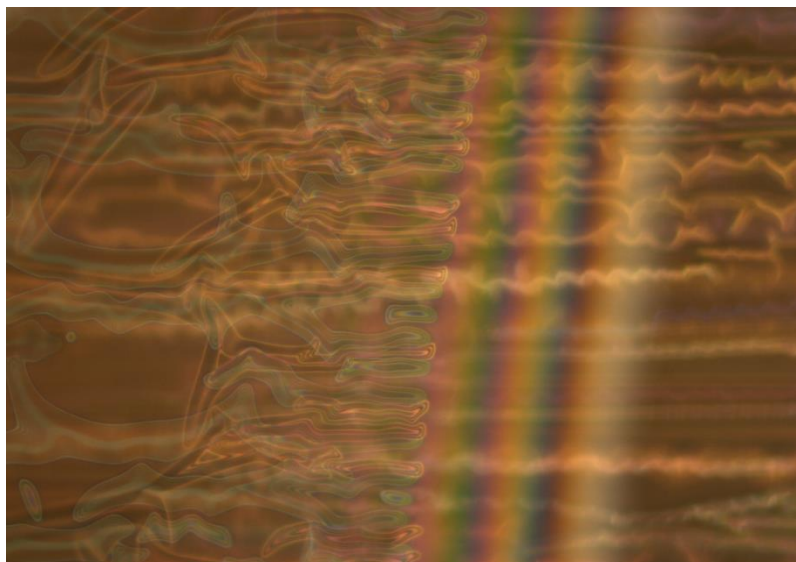
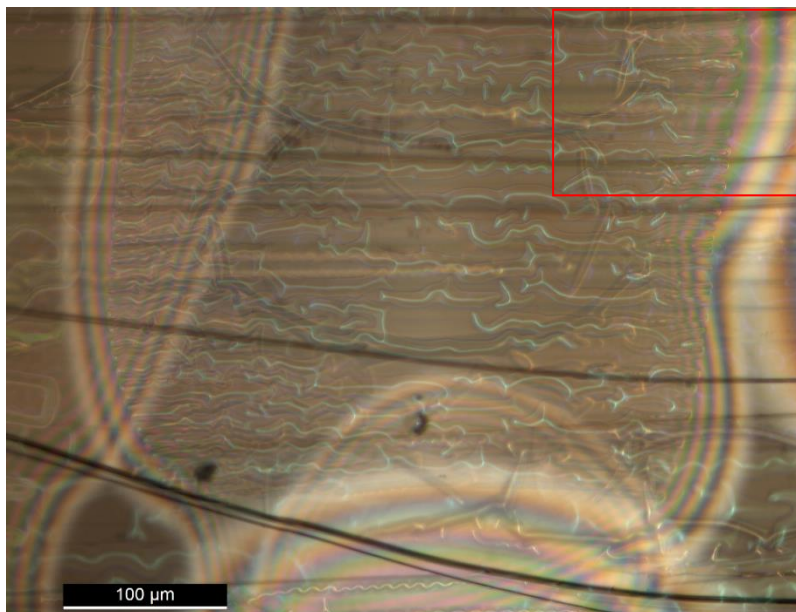
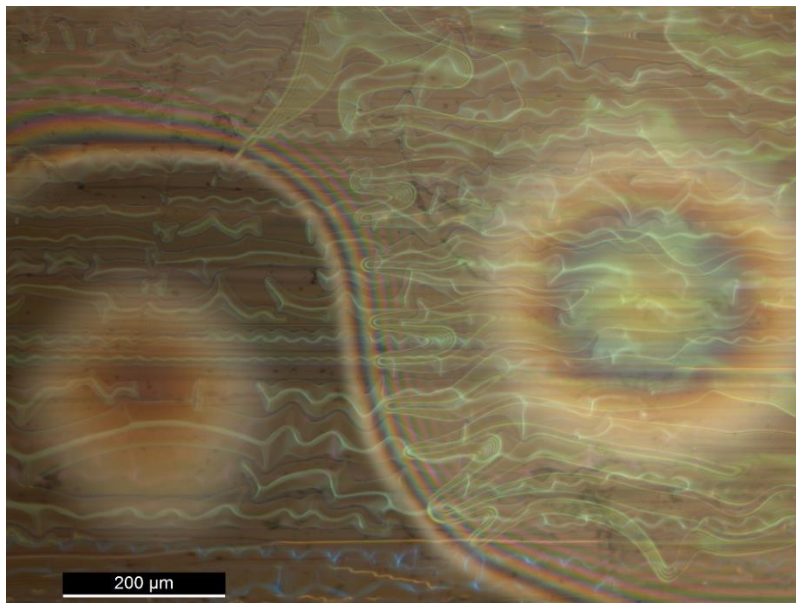


Figure 45 Features visible with the Leica optical Microscope. The rainbow color indicate Newton rings and fringes

4. Discussion

This study was conducted with the aim to investigate at the deformation of muscovite as affected by stress, at high temperatures. The hypothesis was that glide of basal dislocations could be activated to achieve deformation/strain. In the previous section the results of the TGA measurements, the three point bending experiments, and the microstructural analysis were presented.

In this section an attempt will be made to distinguish between flow laws describing the deformation behavior of muscovite under the conditions of the experiments. The results presented in the previous section will be compared to previous work, and underlying mechanism(s) will be proposed and discussed. Lastly, the implications of the present results will be discussed.

4.1 Comparison with previous work

4.1.1 TGA

Our TGA data compares reasonably well with those of Mariani et al. (2006). We find a single stage dehydroxylation between 650°C-920°C for the single crystals, and between 450°C-910°C for the powder, whereas Mariani et al. (2006) find this stage between 600°C-820°C for their powders. The total weight loss of $4.43 \pm 0.2\%$ as measured by Mariani et al. (2006) compares well with our data. Mariani et al. (2006) do not report reaction rate data. In their highest experimental temperature (700°C), they consider 12% water loss, i.e. 0.54% loss of total weight, to be insignificant. Sources of error in the measurements may be due to the presence of some interlayer water and volatilization of elements such as K⁺ (Mariani et al., 2006).

The fanning of the heated samples reported in Section 3.1 did not happen with the samples that were retrieved from the three point bending experiments. This suggests that the fanning does not occur at temperatures below 600°C or that the rate of heating plays a crucial role in this process.

The observation that dehydroxylation starts at 450°C in a powder sample, combined with previous work that reported that for powder samples kept at a constant elevated temperature the dehydroxylation reaction progresses over time (Mariani et al., 2006; Roy, 1949), it creates the possibility that at 600°C the sheeted samples slowly dehydroxylates with time also.

4.1.2 General strain achieved

Results of experiments are graphically represented in Fig. 13 and 14 in strain vs time plots. The average strain achieved in the experiments is around 0.9%. These are relatively small strains compared to most previous work: 22% Mares & Kronenberg (1993), 21% by Kronenberg et al. (1990), 20% Etheridge et al. (1972), 12% Shea & Kronenberg (1992). Our strains compare well with the work of Mariani et al. (2006), who achieved 1.9% in stress relaxation tests and 3.3% in constant strain rate tests. Mariani et al. (2006) employed shear stresses between 14 – 134 MPa. It should be noted that a significant amount of strain may not be included in our analyses due to our choice of the starting point (see Section 3.2.1).

4.1.3 Influence of strain

Our experimental data is gathered before steady state is reached, and it is anticipated that strain influences the results. For single experiments this means that under the influence of stress the dislocation density will increase during the experiment. An increased dislocation density will lead to more dislocation

interaction/entanglement, a process commonly termed strain hardening. Therefore, during the experiment, the applied stress will be less capable to deform the sample and the strain rate will decrease. Ultimately steady state is reached and the dislocation density will no longer increase, and the strain rate will become constant.

Figures 28 and 29 show that within a single experiment the strain rate decreases with increasing strain as follows:

$$\dot{\epsilon} \propto \epsilon^m, \text{ with } m = -2$$

The inferred m-values confirm the occurrence of work hardening. This is expected, as the values are inferred at strains that lie for the largest part in the transient regime (see Fig. 19a and 20a) and not in the steady state regime. This relation holds for experiments with different stresses. Which means that higher stresses do not lead to faster strain rate decreases. It should therefore not influence the calculated stress exponent. Previous research determines the stress exponent at a certain percentage strain, but does not elaborate on strain hardening.

4.1.4 Influence of crystal orientation

In our experiments there is no clear distinction for the strain vs time curves as long as the orientation of the b-axis makes an angle with the long side of the sample. The few experiments with the b-axis parallel to the long side of the sample show slower strain rates at the beginning. From microphysical considerations regarding the crystal structure, a weak mechanical anisotropy could be expected (Meike, 1989; Etheridge et al, 1972). Previous work underlined this, but noted that sample to sample variation gives the same magnitude of scatter as can be expected from the orientation variations (Mares & Kronenberg, 1993; Shea & Kronenberg, 1992; Kronenberg et al., 1990). Within the reproducibility of the experiments, crystal orientation does not seem to affect the results to such extent that separate discussion is warranted.

4.1.5 Influence of stress

The strain rates achieved in our experiments range between 10^{-6} s^{-1} to 10^{-10} s^{-1} . While this is on the slow side compared to previous work, generally in the range of 10^{-3} s^{-1} to 10^{-7} s^{-1} (Mariani et al., 2006; Mares & Kronenberg, 1993; Shea & Kronenberg, 1992; Kronenberg et al., 1990), they overlap by two orders of magnitude. A notable difference is that in our experiments the strain rates 10^{-6} s^{-1} to 10^{-10} s^{-1} are achieved at low strains, while in earlier experiments these low strain rates are associated with high strains. The stresses needed to achieve those strain rates in our experiments are low (0.026 – 0.389 MPa) compared with previous work (0.5-353 MPa) (Mariani et al., 2006; Mares & Kronenberg, 1993; Shea & Kronenberg, 1992; Kronenberg et al., 1990).

One way to relate strain rate to stress is by a power law relation as adopted by e.g. Mariani et al. (2006):

$$\dot{\epsilon} \propto \sigma^n, \text{ with } 0 < n < 1$$

The n-values inferred from our experiments, relating stress and strain rate (see Fig. 25), compare well with the low-strain experiments by Mariani et al. (2006; n-values of 1.13 ± 0.12 strains between 0.5% and 1.9% at strain rates $< 10^{-5} \text{ s}^{-1}$), conducted at 700°C. However, they found a sharp transition to higher n-values (6-65) when the strain rate became faster than 10^{-5} s^{-1} . In other words, the power law with the proposed

linear relationship breaks down at higher strain rates. A similar breakdown is also seen when the power law relationship is applied to data from experiments submitted to higher stresses.

In our experiments low stresses were employed and we expect to achieve slow strain rates, since strain rate and stress are linearly related (by approximation). We employed stresses that were ~ 3 orders of magnitude lower than in previous work, and the strain rates we found were ~ 3 orders of magnitude lower as well. In Fig. 46 the expected strain rates are shown when our employed stresses and temperatures are used for different flow laws established in previous work. The power law relation found by Kronenberg et al. (1990) (see Fig. 46b) predicts strain rates that deviate the most from our results.

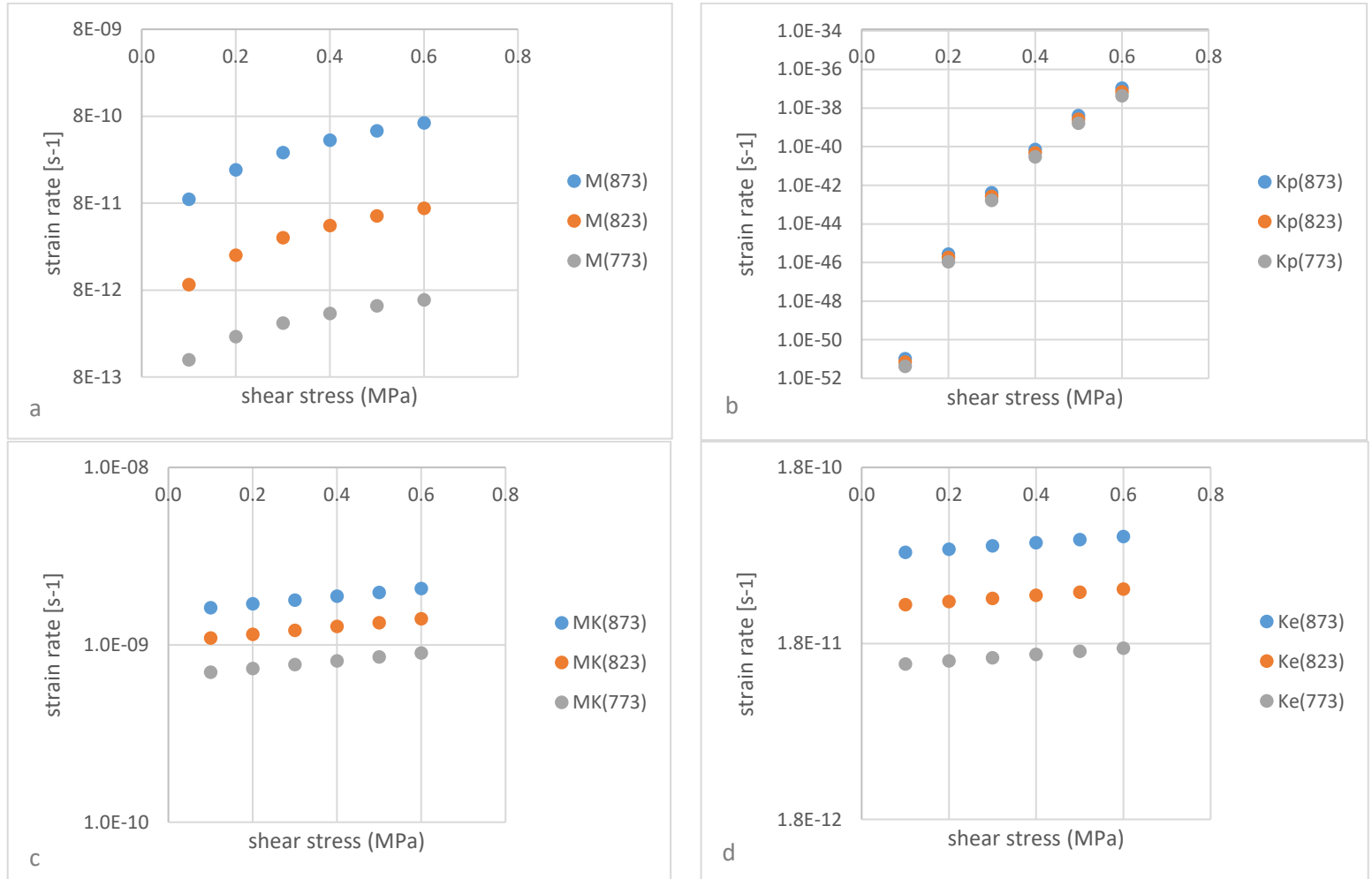


Figure 46. The expected strain rates for experiments under the conditions used in this work, calculated using different flow laws. a) flow law and parameters used as determined by Mariani et al., 2006 for a power law relations between strain rate and stress. b) flow law and parameters used as determined by Kronenberg et al., 1990 for a power law relation between strain rate and stress. c) flow law and parameters used as determined by Mares & Kronenberg, 1993 for an exponential relation between strain rate and stress. d) flow law and parameters used as determined by Kronenberg et al., 1990 for an exponential relation between strain rate and stress

Theoretically, stress exponents of around 1 are expected for creep mechanisms where diffusion is the controlling mechanism. This could be solely vacancy diffusion, as is the case for Nabarro – Herring (N-B) (diffusion through the crystal lattice) and Coble creep (diffusion through the grain boundaries). Both mechanisms are usually observed in polycrystals. For mechanisms describing dislocation movement Harper – Dorn (H-D) creep could yield a stress exponent of 1. For this creep mechanism it is reported that, at low stresses and small stress intervals, the dislocation density is independent of stress. Dislocation motion is then only related to stress by dislocation climb, which is aided by vacancy diffusion. As our experiments are done on single crystals, N-H and Coble creep are deemed unlikely.

Other mechanisms unrelated to vacancy diffusion or dislocation motion, which also generates a stress exponent of 1 are pressure solution mechanisms. These mechanisms are usually seen in wet polycrystals. Pressure solution can be treated mathematically similar to Coble creep. In theory, there could be pressure solution at the contact points of the set up with the sample (the semi-cylindrical rods) and it should leave a visible imprint in the samples surface. We disregard these processes as potential deformation mechanisms, as our samples surfaces are considered dry, due to high experimental temperatures, and there are no indications of these processes seen at the samples surface.

It could be expected that in a 3-point bending set-up, when higher strain rates are achieved, there could be a similar breakdown of the power law as seen by Mariani et al. (2006). These higher values of the stress exponent are also found in previous studies. Kronenberg et al. (1990) present values of 18 ± 4 for single crystals of biotite.

The other way to relate strain rate to stress is by an exponential relationship as adopted by e.g. Mares & Kronenberg (1993):

$$\dot{\epsilon} \propto e^{\alpha\sigma}, \text{ with } 0 < \alpha < 6.8$$

Mares & Kronenberg (1993) report an α -value of 0.5 ± 0.2 , however reanalysis of their data (their Fig. 11) yields an average α value of 0.27 at 5% strain. Kronenberg et al. (1990) found a value of 0.41 ± 0.08 for single crystals of biotite at 5% strain. At first glance, the α -values found in this study vary with strain (see Fig. 26), but when the error bars are taken into account, the values average around 4, for our medium strains (0.075-0.6%). It is important to note that these values are found for a non-steady state. This makes it hard to compare with previous work, where steady state was reached.

The physical consideration underlying the exponential relation is the elementary (atomic scale) jump frequency (see Section 1.4.2.3). The mechanism represents dislocation glide limited by obstacles/Peierl's stress.

4.1.6 Influence of T

$$\dot{\epsilon} \propto e^{-\frac{\Delta Q}{RT}}$$

This Arrhenius type of temperature dependence is assumed for both the power law and the exponential law. The activation energy is presumed to be a value independent of temperature, stress and pressure. It represents the energy a particle must have to overcome the barrier, i.e. the barrier height relative to the equilibrium position, and is defined independent of the parameters that decrease or increase the relative barrier height. ΔQ , which is proportional to the slope of $\ln \dot{\epsilon} - 1/T$ plot (Arrhenius plot), is the apparent activation energy of creep (see Section 1.4.1 and Fig. 11). The values I found for ΔQ start with $\sim 206 \text{ kJmol}^{-1}$ at small strains and decrease with increasing strains (see Fig. 37). At the high strains in my experiments, there is no longer an activation energy required within the scatter and uncertainty in the data. This implies that the processes are independent of temperature. However, it should be noted that, since my calculations are done on very little data, this value is subject to large uncertainties.

The obtained value falls in line with previous work, although the activation energies reported in literature are also poorly constrained. The values range from as low as $47 \pm 19 \text{ kJmol}^{-1}$ (single crystals of muscovite; Mares & Kronenberg, 1993) to as high as a minimum of 270 kJmol^{-1} (muscovite gouge; Mariani et al, 2006). Kronenberg et al. (1990) calculated the activation energy of single crystals of biotite for both the power law and the exponential law, and obtained values of $82 \pm 13 \text{ kJmol}^{-1}$ and $51 \pm 9 \text{ kJmol}^{-1}$ respectively. Note that the same experiments were used for these calculations.

The authors all inferred/assumed that the mechanism contributing to strain was dislocation slip and glide on (001), even though their conditions varied. This has as a consequence that they all assumed the same process, dislocation glide (see Table 1), thereby eliminating the possibility to explain their activation energy differences by a difference in operating process.

There is a difference in approach since I did constant stress experiments, and other workers did constant strain rate experiments. These differences propagate into the plots used to determine ΔQ . For my work, I used the “classic” Arrhenius plot ($\ln \dot{\epsilon} - 1/T$ plot). For constant strain rate experiments, the $\sigma - 1/T$ plot (for exponential) or $\ln(\sigma) - 1/T$ plot (for power law) is used. Both plots have their α - or n -value as part of the slope. As seen by others (Kronenberg et al, 1990; Shea & Kronenberg, 1992) this results in different activation energies for the flow laws.

Also, the range of temperatures used in the construction of these plots, could be of great influence of the found activation energy (see fig. 11). That is, if the assumption that there is one unique thermally activated process operating, is incorrect.

4.2 Macroscopic Observations

I said a little earlier that the total displacement or strains reached are very small. This corresponds to a tenth of a millimeter displacement of the center. We were unable to observe this displacement after the set up was disassembled. One could explain this in a few ways, the displacement measured, does not exist and is some result of instrumental drift, but I don't think this is the case. As I did some dummy runs, and although there is some drift measured, those results were clearly different from the actual runs. The other option is that the displacement measured is there, but somehow it is reversed upon unloading. I don't think this is the case either, although reversible strains are reported for sheeted minerals, they always follow a permanent strain.

What this leaves us with, is that the measured displacements are small enough to be undone by the technique we used to measure it. This involved sticking the sample on sticky tape to a sample holder, and prepping it for SEM measurements. And if the sample had a miniscule curve to it, the sticky tape was adhesive enough to counteract this.

4.3 Microstructures

In our samples, no indication of kinks or cracks formed during deformation is found, and mechanisms involving these microstructures (like low angle kink bands, or dislocation pile ups) are therefore not discussed.

As said at the end of section 3.4.2 the microstructures seem to be superficial and only involve the first near surface layers of the muscovite sample. There are no obvious differences in the samples that are only heated to 600°C and the samples heated to 600°C and stressed. We therefore assume that the formation of the microstructures is solely due to the temperature. Combined with the assumption that the features are superficial, it follows that the surface microstructures bear no relation with deformation. However, their formation could influence the measurements of deformation. To estimate their relevance in our analysis of the mechanical data (section 4.1), a few possible mechanisms are brought forward and discussed.

4.3.1 Potential “mechanisms” to create the observed microstructures

Dislocation networks

Networks form when a dislocation moves through the crystal and interact with another (nearby) dislocation. Lothe & Hirth (1982, p. 663) state that, in general, if interactions between crossing dislocations occur, a dislocation net with hexagonal meshes is produced. If the reactions do not occur, the mesh is more logenze-shaped (see Fig. 47). Pure twist boundaries are always hexagonal shaped.

These expressions of dislocation have been found by previous workers. Mares & Kronenberg (1993) reported the presence of hexagonal meshes (see Fig. 48) observed in TEM micrographs. The hexagonal mesh can be observed as a symmetrical “ripple” (see Fig. 48 middle). They also observed straight dislocation lines and curvilinear dislocation lines. Christoffersen & Kronenberg (1993) examined deformed single crystals of biotite and found hexagonal meshes (see Fig. 49). It is important to note that these are TEM images, and this work only reports secondary electron SEM images. It is therefore unlikely that our observations are of similar structures.

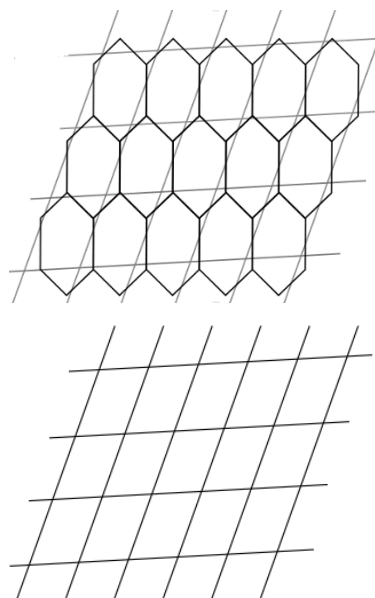


Figure 47 Figures from Lothe & Hirth (1968, p.662) depicting two types of dislocation networks. Top: a hexagonal mesh formed when crossing dislocation interact. Bottom: a logenze-shaped mesh formed when the interaction does not occur.

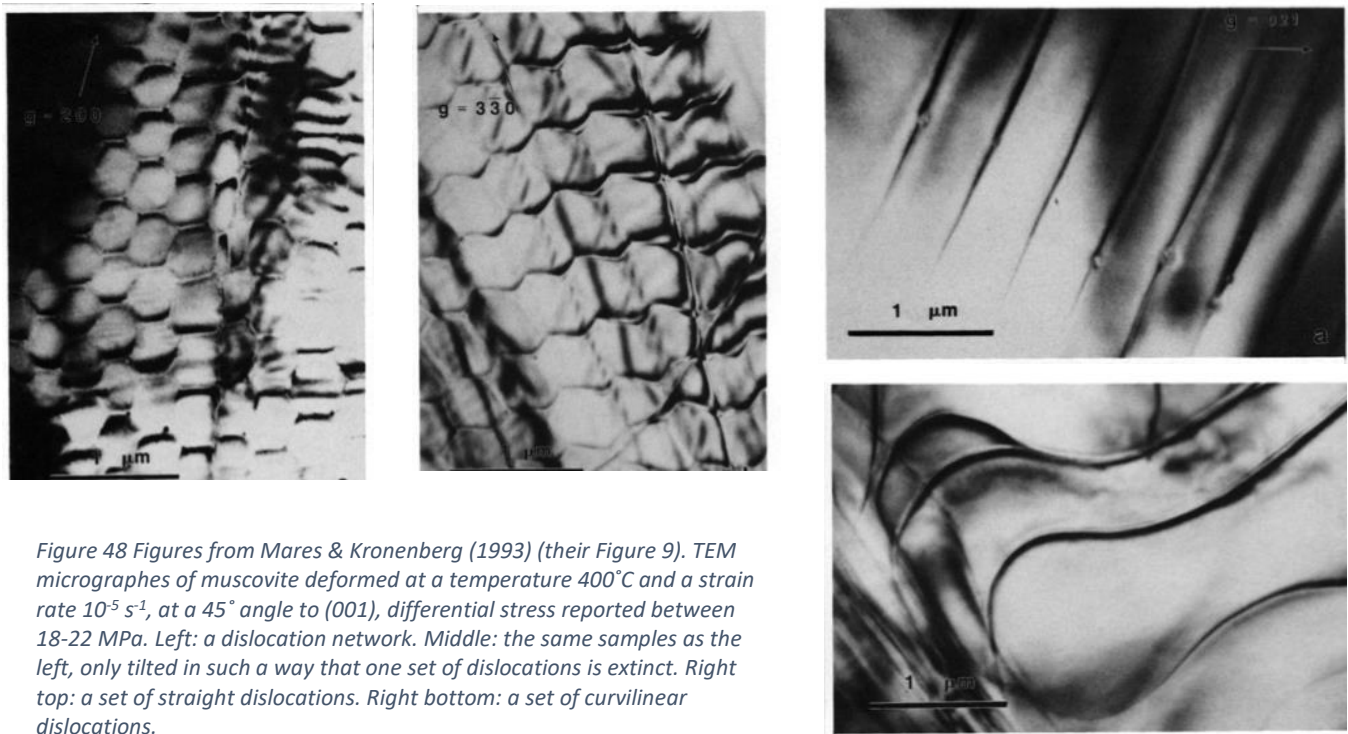


Figure 48 Figures from Mares & Kronenberg (1993) (their Figure 9). TEM micrographs of muscovite deformed at a temperature 400°C and a strain rate 10^{-5} s^{-1} , at a 45° angle to (001), differential stress reported between 18-22 MPa. Left: a dislocation network. Middle: the same samples as the left, only tilted in such a way that one set of dislocations is extinct. Right top: a set of straight dislocations. Right bottom: a set of curvilinear dislocations.

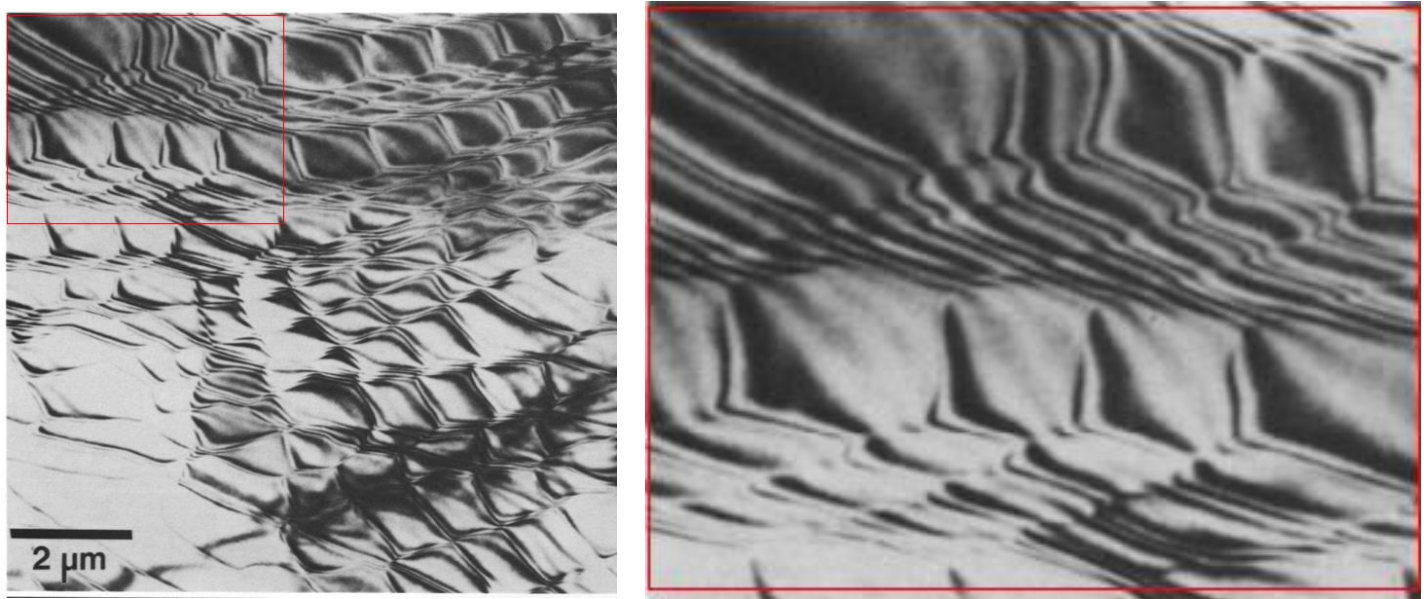


Figure 49 Figures from Christoffersen & Kronenberg (1993) (their Figure 6). Left: TEM bright-field image of an extended network with a complicated geometry in single crystal biotite deformed at a temperature of 400°C , a strain rate of 10^{-5} s^{-1} with a shear stress of 21 MPa, at a 45° angle to (001). Right: enlargement of the red frame in the left image to highlight the "asymmetric ripples".

Helical dislocations

In crystals that accommodate deformation associated with climb, dislocations can form spiral structures as described by Hull & Bacon (2011) (see Figure 50). They form when a dislocation, with a partly edge and partly screw character, is pinned between two points. Dislocations both glide and climb, where the climb is aided by vacancies. Ultimately this can lead to a dislocation with a helical appearance, with a Burgers vector along the axis of the helix.

These dislocations are made visible by decorating techniques and observed with SEM imaging. This makes it unlikely that our microstructures are of similar origin.

Wrinkles, Ripples

Other studies describe microstructures observed in graphene or other layered solids. Deng & Berry (2015) proposed a few possible mechanisms involved in the formation of wrinkles (length:height ratio 10:1), ripples (ratio 1:1) and crumbles (dense deformations with folds and wrinkles) observed on the nanometer scale. Wrinkles are fairly straight features (see Fig. 51a) but they can develop into wrinklons (Fig. 51 b and c),

producing straight lines at an angle with each other, and a higher density of microstructures at the edge of the sample (Compare Fig. 51 c with Fig. 42 F). It should be noted that these studies are done on samples of just a few layers of graphene, and our samples consist of a multitude of muscovite layers. In this work we tried to activate basal dislocations in muscovite samples with a thickness of a few tenths of mm. Therefore, a mechanism relevant for this work could be defects and/or dislocations inducing microstructures.

Deng & Berry (2015) propose that out of plane deformation (like wrinkles and ripples) is a way to significantly reduce the magnitude of in-plane stresses generated by the defects. The ripples wavelength and amplitude decrease as the angle between the line-defect and strain-direction increases (Deng & Berry, 2015).

Another potential source for in-plane stresses are not only defects, but also excess material or length which can arise if there is a difference in the thermal expansion coefficient between the layers and the substrate (Deng & Berry, 2015). In our case, this would be between surface layers and the bulk, as the dehydration onset of the muscovite starts with the surface layers, and dehydration influences the crystal structure or bond lengths in such a way that during heating the surface gains more length, or during the experimental run the surface gradually gains more length or that upon cooling and shrinking the surface shrinks less than the bulk. The result is a surface layer with an excess of length with respect to the bulk and this could lead to ripple formation.

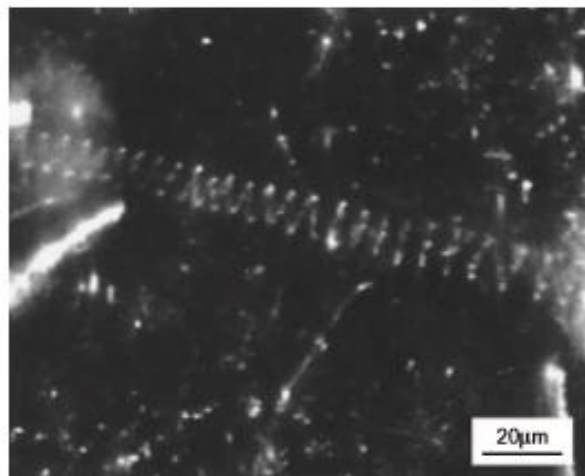


Figure 50 Figure from Hull & Bacon, 2011 (their Figure 3.21). A dislocation in CaF_2 revealed with a SEM using the decoration technique (After Bontinck and Amelinckx, *Phil. Mag.* 2, 94, 1957) showing a helical spiral.

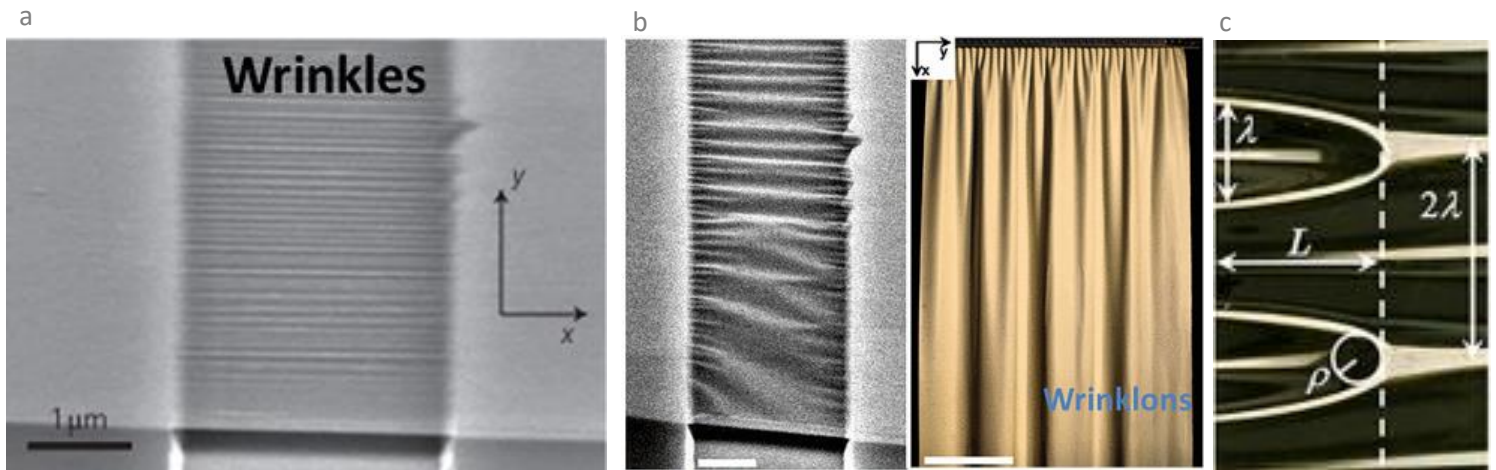


Figure 51 Wrinkles and wrinklons as presented in Deng & Berry, 2015 (fig. 7). a) a bilayer suspended graphene membrane produced by thermal manipulation, b) SEM image of suspended graphene bilayer (scalebar is 1 μm), and a pattern of folds obtained from a rubber curtain (scalebar is 25 cm), c) schematic representation of the morphology of the wrinkle.

Ripplocations

Ripplocations have been defined by Kushima et al. (2015) as sharp and localized folds, aligned with well-defined crystallographic directions, in thin-layered crystals with van der Waals structures. They originate from excessive material inserted in one layer compared to another much like edge dislocations (see Fig. 52 top). However, ripplocations are energetically different from the conventional dislocation. Striking is that ripplocations do not have a burgers vector (Griggs et al, 2017), and that same sign ripplocations attract and merge into larger structures (Kushima et al., 2015) (see Fig. 52 bottom). Kushima et al. (2015) thought of ripplocations to be near surface structures in 2D van Der Waals solids, but Griggs et al. (2017) extended this idea to all layered solids and made a case for ripplocations to occur in the bulk of the crystal as well as the near surface (see Fig. 53). Ripplocations were found to come in two types, in sharps lines, or as tortuous wrinkles with relatively large wavelengths and asymmetric morphologies, observed on the nanometer scale (Kushima et al, 2015). Their energies only depend on the amount of excess material and the sharp lines are thought to be quite mobile (Kushima et al., 2015; Griggs et al., 2017), in contrast the wrinkles can hardly migrate once formed (Kushima et al., 2015). It takes little external driving force to overcome the migration barrier and move the sharp line ripplocation athermally (Kushima et al., 2015). Sharp line ripplocations can merge and when large enough can self-fold into large wrinkles, and due to the multilayer adhesion between self-folded domains, they become kinetically trapped (Kushima et al., 2015).

These ripplocations are only reported to date on the nanometer scale, and are therefore insufficient to explaining the deformation and microstructures reported here. However, if there is a way to upscale these features, this could be interesting, especially in the light of my proposed microstructure evolution (i.e. the merging of ripples, towards dog-bone shapes and ultimately the dome-like structures, see Section 4.2.2)

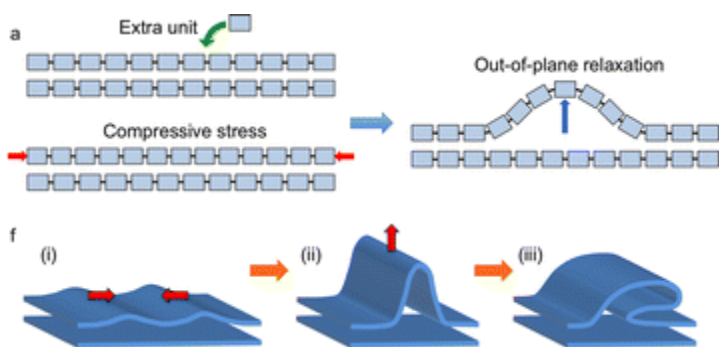


Figure 52 Figure from Kushima et al. (2015) (their Figure 2). Top: schematic illustration of the formation of a ripplocation by adding extra material in a simulated bilayer model. Bottom: schematic illustration of the tendency of ripplocations to merge and form larger structure

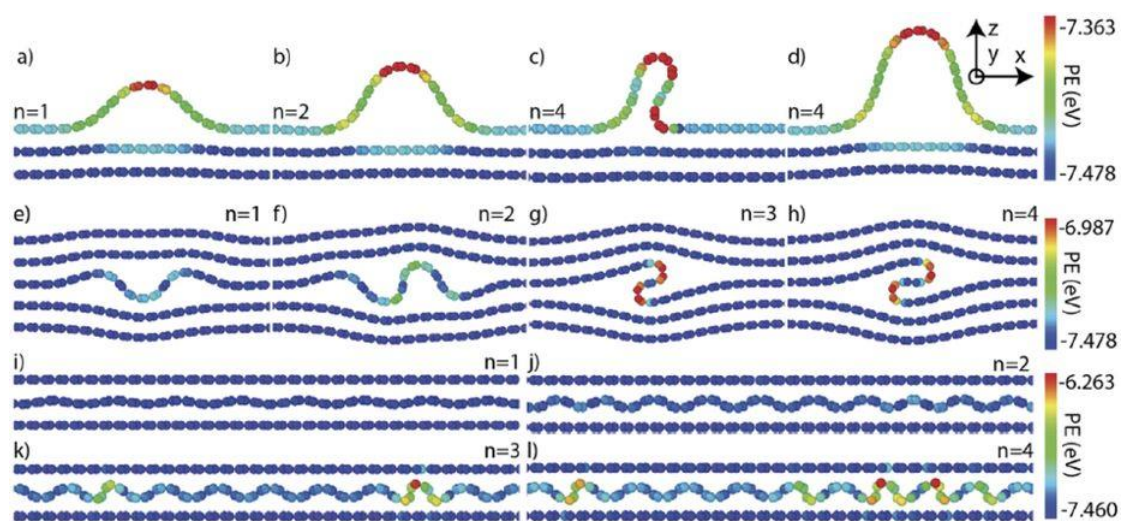


Figure 53 Figure from Gruber et al (2017) (their Figure 1). A schematic illustration of ripplocation formation, depending on excess material (n), in a model simulation. Top: (a-d) unconstrained surface showing two forms of $n=4$ structure. Middle: (e-h) bulk unconstrained. Bottom: (i-l) bulk constrained. Atoms are colored according to their potential energy defined from the interatomic potential whose scale is shown on the right. This is a side view of several layers.

Water evaporation vesicles & air content

Muscovite is known to dehydrate at elevated temperatures. Deng & Berry (2015) propose trapped solvent evaporation/removal as a possible mechanism responsible for formation of microstructures. Previous work has been done on water vapor vesicles during thermal breakdown of muscovite. Those vesicles always have a circular bubble shape in the (001) plane (Devineau et al., 2007; see Fig. 54) and are seen after melting has occurred (Rodriguez-Navarro et al., 2003). These structures are different from the microstructures in our samples, and it is therefore not likely that they indicate the presence of water vapor vesicles.

Although it is not mentioned in previous work, there is a 25% air content in our samples according to the supplier (SPI supplies). It could be possible that the air inside the crystal expands more during heating than the crystal itself in such a way that it can no longer remain inside the samples and alters the structure upon leaving. Although I deem it unlikely that this causes the microstructures, it might aid or impede the dehydroxylation.

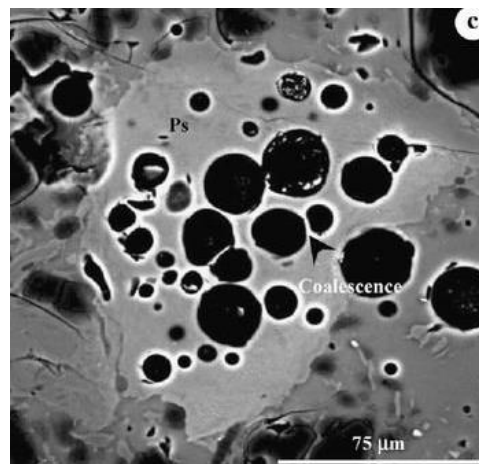


Figure 54 Figure from Devineau et al. (2007) (their Figure 1c). BSE-SEM image showing bubbles (dark areas) in basal sections of muscovite pseudomorph after heating at 1,175°C for 40 min

4.3.2 Most likely mechanisms operating in the experiments

The reason we investigated the microstructures is to quantify their influence on the deformation or the measurement of deformation.

A few mechanisms that could cause the microstructures are discussed above. My most logic conclusion would be that there is some thermal coefficient difference involved, which triggers a ripplocation kind of microstructure formation to reduce in-plane stresses. A necessary assumption in this case is that the dehydroxylation reaction leads to a volume change of the top layers with respect to the bulk. The surface layer needs an excess of length or volume that is unable to simply extend over the bulk samples edges, to cause in-plane stresses. In order to reduce those, out of plane deformation triggers the formation of ripples. This deformation could follow crystallographic orientations. Support of this hypothesis is the observation that when the samples were heated to 900°C, the microstructures were not found, but the samples “fanned” out (see Fig. 16), indicating some kind of volume change. The microstructures are most abundant at 600°C, but also occur in the samples heated to 550°C. The remaining issue that needs to be resolved for the interpretation of the mechanical data, is the timing of the microstructure formation, i.e. is it (semi-)instantaneous upon heating, does it occur gradually over time during the experimental run, or do they form upon cooling. In the first and last case, the formation would not influence the measurement of the deformation. If, however, they form gradually during the experimental run, they could influence the measurements.

To see if the microstructural development could significantly influence the measurement when they gradually form during the experiment, we consider the scale of the features. Some ripples have almost 100 μm long wavelengths, we can assume a 1:1 ratio (ripples), or a 10:1 ratio (wrinkles), giving the largest structures height varying between 100 μm and 10 μm . We have displacements of max 100 μm . In a 1:1 ratio, this could affect the measurement of strain by 10-100%. Therefore, if the features develop during the experiment, the bubbling of the surface, could cause a significant apparent decrease in strain rate.

The colors in the sample, visible macroscopically and with the Leica microscope, act as an indicator that the microstructures are “hollow” structures and not deposits on the surface. They can tell something about the distance between the top of the structure and the bottom, i.e. the height of the hollow. However, I did not elaborate on this.

As said earlier, ripplocations tend to merge and form larger structures. There are several microstructures presented in Fig. 42-43, straight lines, symmetric ripples, asymmetric ripples, starting dog-bone, dog-bone and the dome-like structure. Straight lines are seen to be going towards rippled lines (see Fig. 42 G and Fig. 43 E) and the asymmetric rippled lines are seen to be going towards the dog-bone shapes (see Fig. 41 D and Fig. 42 H), and the dog-bone shapes merge towards more dome-like structures (see Fig. 43 D). Following the merging idea, I propose an “evolution” of the microstructure as shown in Fig. 55. As what is shown by Fig. 41-43 are only snapshots of the evolution of the microstructures, it is difficult to distinguish between a time evolution and/or a spatial distribution.

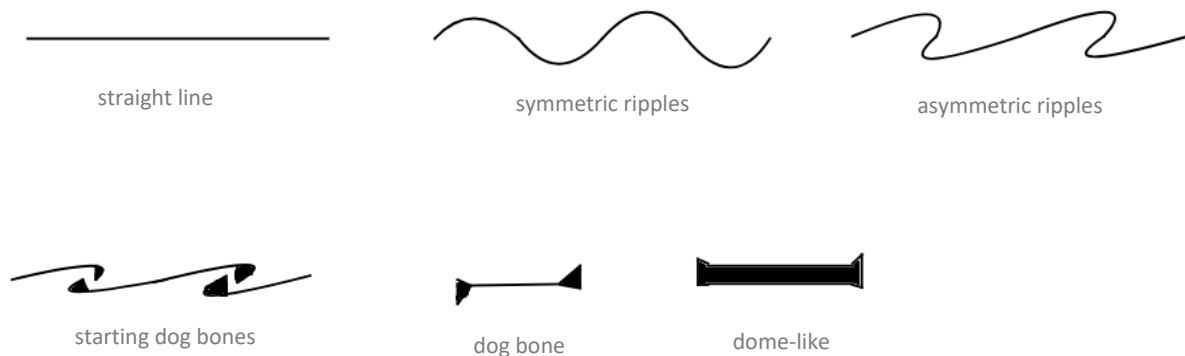


Figure 55 Schematic illustration of the proposed microstructural ‘evolution’. Microstructures start as straight lines, and under influences of in-plane stresses, slowly evolve into symmetric ripples, to asymmetric ripples that eventually “break” to form dog-bone shapes, after which the shapes merge into larger dome-like structures.

4.4 Underlying mechanism of deformation

With the assumption that the microstructures are not an expression of deformation or dislocation activity, but a result of the sample heating and cooling, the underlying mechanism responsible for deformation will be inferred only from the mechanical data. Remember, the micromechanism responsible for creep is usually creep of basal dislocations (see Section 1.5).

4.4.1 Power law

In Section 4.1.6 we arrive on Harper-Dorn (H-D) creep (see Section 1.4.2.1) operating under low stress, high temperatures (Ardell & Lee, 1986), as the most likely model describing the deformation in our experiments. In all materials exhibiting this creep, there is a transition to power-law creep when the applied stress exceeds a characteristic transition stress (Ardell, 1997). It is suggested that H-D creep involves dislocation glide, but is controlled by climb of edge dislocations saturated by vacancies (Langdon & Yavari, 1982 (for Al-5% Mg solid solution alloy)). However, it is probable that the controlling factor might equally well be cross-slip of screw dislocations, depending on the material under consideration. One view regarding H-D creep is that there is nothing special about it, and that it is a manifestation of “normal” power-law creep when the applied stress is smaller than the internal stress determined by the steady state dislocation density (Ardell, 1997; Ardell & Lee, 1986). The other explanation for the transition stress from power-law creep to H-D creep, is that H-D creep prevails when the applied stress is too small to activate Frank-Read (F-R) sources. H-D creep is only seen in materials with a low starting dislocation density.

A dislocation density independent of stress means that this density does not in-/decrease with in-/decreasing stress. The view in which the stress could be too low to activate F-R sources, seems to imply that there are no new dislocations formed under the influence of stress (this is if F-R sources are the only dislocation sources). Following this thought, strain hardening due to an increase in dislocation interaction, should not be observed in the material if H-D creep is governing the deformation, or only to a very limited extent (only existing dislocation can move and interact). The question remains how strain is accumulated in this way.

Another way to maintain a constant dislocation density with increasing stresses, is that the dislocation disappear as fast as they are formed, i.e. the dislocations need to be able to move very freely, and no entanglement or interaction should occur. Entanglement would (temporarily) catch dislocations and increase their density if the rate of formation remains constant. Strain hardening could be possible if the rate of entanglement somehow regulates and balances the formation rate.

When microstructures are investigated in material exhibiting H-D creep, it can be described as a three-dimensional network (Ardell & Lee, 1986), i.e. showing evidence of dislocation interaction. Ardell (1997) proposed that the plastic strain during H-D creep is generated by constrained dislocation motion during coarsening of the dislocation network. It is a balance between hardening as a consequence of the nearly immobile dislocations in the network, and recovery involving the coarsening of the network (Ardell, 1997).

4.4.2 Exponential law

The exponential law concerns glide, by taking the energy needed to overcome obstacles/Peierls valleys as the rate-limiting factor (see Section 1.4.2.3). It describes the atomic jump from one equilibrium position to the next, including stress assisting this process. α includes geometric parameters associated with the energy barrier. Unlike H-D creep it does not explicitly require vacancy diffusion, with its linear dependence on stress, for out of plane movement of dislocations. Furthermore it imposes no limitations towards strain hardening or strain softening.

4.4.3 Best fit

Both explanations/mechanisms fit the data. For the power law, the n -values would correspond to an H-D creep model, representing dislocation glide and climb aided by vacancy diffusion. The main feature of H-D creep is that the dislocation density remains constant over a range of applied stresses. In a bending set-up there is a geometrically need for an increase in same sign dislocations to accommodate the bending. If the dislocation density is to remain constant, dislocations of the opposite sign should be removed from the crystal lattice, while the wanted dislocations increase. So, there is no net change in density, but a net change in the signs of the dislocations. The exponential law representing the atomic scale jumping process, fits the data equally well, and imposes no limitations to dislocation density. This means that the geometrically necessary dislocations for bending can be formed, and their density can increase without the need to balance this with a process to proportionally remove the dislocations with the opposite sign.

During our experiments strain hardening is observed (i.e. with increasing strain, the strain rate decreases). As strain hardening is usually the result of dislocation interactions, slowing down the average dislocation velocity, it seems reasonable that this is accompanied by an increase in dislocation density.

If the problem is simplified in this manner, Harper – Dorn creep is excluded as a possible mechanism operating in our samples. This makes the exponential creep mechanism the most likely mechanism active in our samples.

4.5 Implications of my work

There is a knowledge gap in the mechanism/interpretation of deformation in mica's, involved in modelling crustal and fault strengths. This work aimed to find constraints for the stress sensitivity of the deformation of muscovite, taking as a representative of the micas. The results were comparable with the results found in earlier studies for a power-law relation between stress and strain rate. Within the small stress range and high temperature conditions tested, this relationship was linear. The exponential law fit the data equally well. From theoretical considerations the dislocation density exponential law creep had the fewest theoretical constraints and is therefore the most likely fit. This would have consequences for the models using the power law interpretation (see Fig. 2).

4.6 Suggestions for methodological improvements

The three point bending set up employed only allows for constant load experiments. Temperatures could be adjusted during the experiments if that was found necessary. The temperature regulator had a tendency to largely overshoot the designated temperature and therefore setting up an experiment required relatively much attention to prevent temperatures that exceeded the desired temperature. When the temperature control is more refined, it could decrease the sample to sample variation for temperatures close to the onset of dehydroxylation.

It is unfortunately not possible to do constant strain rate tests in the current set up and neither is it possible to employ confining pressures or providing a wet environment for the crystal, making direct comparison with previous work a little harder.

Although the relative simple set up of the three point bending apparatus has advantages in the ease to use and the operational costs, it also has a few shortcomings. They are mostly related to the way the load is transmitted to the sample. The dead weight has a little room to move and is therefore not always applied in the exact middle of the sample. The heating and cooling of the machine seems to affect the straightness of the kanthal wire. Deviations in the straightness of the kanthal wire effect the smoothness of the up and down movement of the load, i.e. it can get stuck in the steel guiding plate. It also affects the way the top rod is placed onto the sample, as you remove the support sideways, one side of the loading circle lowers earlier than the other side. In a few cases the load remained uncentered, instead of the loading evenly across the sample. During the loading of the sample and unloading the sample itself can be moved around by the kanthal wire and the top rod, further adding to the problems of loading exactly in the middle. Upon loading the kanthal wire is displaced from the oven chamber, giving rise to a “thermal cooling” stage, which affect the initial part of the displacement measurements. It follows that there is room for improvement of this part of the set-up. An option could be to automate the up and down movement of the support, to minimize differences between experiments.

Experiments are performed with a closed oven chamber, so no visual control is possible once the experiment is started. As a consequence, the actual bending at high temperatures cannot be directly observed. It could be interesting to be able to compare the (elastic) bending at high temperatures to those observed on room temperature.

4.7 Further research

A lot of things remain enigmatic about the deformation process(es) at work. A few things are mentioned throughout the discussion that could shed some light on the matter. Options are explored for further research using the same experimental set up employed in this work, but also some suggestions for different methods are included.

First of all there are a few notes about the microstructures. As it is now, the hypothesis proposed could be tested by investigating the ripplocations dynamics to see if they can be scaled from nm to μm . Absence of clarity remains about the microphysics behind the changing length/volume of the upper plate, and whether or not this could be due to (partial) dehydration. With TGA measurements the samples can be brought to experimental temperatures with a very strong control on heating rate and maximum temperatures. Measuring the weight loss for different amounts of time, e.g. 1 min at 600°C, 1 hour and 24 hours, could correlate the extent of dehydroxylation with the formation of microstructures. More

detailed microstructural study could also confirm the proposed hypothesis that the microstructures bear no relation with the deformation. Further research on the colors visible in the sample could be used to determine if the microstructures are hollow, and say something about the height of the hollow.

As for the creep laws, solely the n and Q values don't give enough information to pinpoint a mechanism (Poirier, 1985). Further investigation of the microstructural state of the samples, e.g. dislocation configuration examination by TEM or decoration techniques for the SEM, can be used to distinguish between the potential creep process(es). By observing the dislocation density, it can be established whether or not it is independent of stress, which is a distinguishing feature for H-D creep. Other observations could include the organization of dislocations (to accommodate bending), e.g. by an increase of one sign of dislocations versus the opposite sign. This could involve going into more detail with the theory behind the geometrical necessary dislocations (GNDs).

Furthermore, it could be interesting to see if experiments with higher applied stresses can be done in the three-point bending set up to confirm the theoretical expectation that for power law creep the linear relation found between strain rate and stress should break down at higher stresses. In my experience, the sample literally broke when loaded with a stress of 0.5 MPa. However, this involved a very thin sample, which could have had pre-existing fractures due to the separating method, causing the failure.

5. Conclusions

In this study I experimentally investigated the ductile deformation behavior of single crystals of muscovite at high temperatures against a theoretical background. Based on my results, I conclude the following:

Theoretical background of intra-crystalline deformation mechanisms yields two different approaches for the relation between strain rate and stress. The first approach assumes a power law relation, $\dot{\epsilon} \propto \sigma^n$, and it has a geometrical basis. It assumes that deformation is accommodated via glide of dislocations as well as climb. In the Weertman model a stress exponent of 3-5 is usually found. A stress exponent of one is found for the model of Harper – Dorn creep, which states that dislocation density is independent of stress. The second approach assumes an exponential relation, $\dot{\epsilon} \propto e^{\alpha\sigma}$, and it finds its basis in the elementary jump theory. It assumes that deformation is accommodated via glide of dislocations limited by dispersed obstacles such as interstitials and impurities.

The employed stresses ranged between 0.1-0.4 MPa and gave initial strain rates of 10^{-6} s^{-1} that decreased with time to a value between $10^{-8} - 10^{-10} \text{ s}^{-1}$. When a power law relation was fitted to the data, our results gave a stress exponent (n) of 1, corresponding with Harper-Dorn creep. When an exponential relation was fitted to the data, our results gave an exponential factor (α) of 4. It is important to note that these values are inferred before (quasi) steady state is reached, and caution is needed when comparing these results directly to previous work. Adding to this caution is the fact that the three point bending set up uses constant stresses, which is quite different from the triaxial compression set up with constant strain rates used in previous work.

Our experiments yielded very small strains, maximum strains achieved ranged between 0.6-1.0 % and upon retrieval the sample did not show any permanent bending. The method employed to examine for any permanent bending is quite possibly too crude to measure any permanent deformation. The development of extensive microstructures on the samples surface, ranging from straight lines to dome-like structures on a scale of 5-250 μm , did not influence the deformation or the measurement of deformation, as they are most likely a shrinking feature upon cooling.

The two flow laws cannot conclusively be distinguished based on the data. However, from the Geometrically Necessary Dislocations (GND) theory it follows that in a bending geometry, dislocations of one sign need to accumulate in the crystal to accommodate the bend which conflicts with the assumption of a constant dislocation density. In addition, we also observed strain hardening, Harper-Dorn creep is therefore regarded unlikely. This leaves dislocation glide (exponential creep) as the most likely deformation mechanism in our three-point bending tests. This has implications for models that use a flow law with power law relation between stress and strain rate to incorporate phyllosilicate behavior. As the exponential relationship predicts higher strain rates for lower stresses, and therefore a weaker crust (see Fig. 2). A weaker crust means that displacement can occur along a fault at lower stresses. This means that the strain will most likely be released aseismically before stresses necessary to initiate brittle behavior can build up.

Experiments with a wider range of stresses and temperatures are needed, to further investigate the found fit for both approaches. As long as there is no conclusive answer to which flow law is most accurate in which situation, researches need to carefully select a flow law, and make a theoretical assessment before selecting one approach or the other.

6. Acknowledgements

I would like to thank my supervisors for their support during this project and the technical staff for helping me with the experimental set up.

7. References

- Ardell, A.J. and Lee, S.S. (1986), *A dislocation network theory of Harper-Dorn creep—I. Steady state creep of monocrystalline Al*, Acta Metallurgica, vol. 34, no. 12, p. 2411-2423
- Ardell, A.J. (1997), *Harper – Dorn creep – Predictions of the dislocation network theory of high temperature deformation*, Acta Materialia, vol. 45, no. 7, p. 2971-2981
- Bos, B. and Spiers, C.J. (2002), *Frictional-viscous flow of phyllosilicate-bearing fault rock: Microphysical model and implications for crustal strength profiles*, Journal of Geophysical Research: Solid Earth, vol. 107, no. 2, 2028, p.1-13
- Chen, J. and Spiers, C.J. (2016), *Rate and state frictional and healing behavior of carbonate fault gouge explained using microphysical model*, Journal of Geophysical Research: Solid Earth, vol. 121, no.12, p. 8642-8665
- Christoffersen, R. and Kronenberg, A.K. (1993), *Dislocation interactions in experimentally deformed biotite*, Journal of Structural Geology, vol. 15, no. 9-10, p. 1077-1095
- Cottrell, A.H. (1953), *Dislocations and plastic flow in crystals*, London, Oxford University Press
- Deng, S. and Berry, V. (2015), *Wrinkled, rippled and crumpled graphene: an overview of formation mechanism, electronic properties, and applications*, Materials Today, vol. 19, no. 4, p. 197-212
- Devineau, K., Villiéras, F., Barrès, O. (2007), *Development and evolution of water vapor vesicles during fast thermal breakdown of muscovite*, Physics and Chemistry of Minerals, vol. 38, no. 8, p.559-572
- Dunne, F.P.E., Rugg, D., Walker, A. (2007), *Lengthscale-dependent, elastically anisotropic, physically-based hcp crystal plasticity: Application to cold-dwell fatigue in Ti alloys*, International Journal of Plasticity, vol. 23, no. 6, p.1061-1083
- Etheridge, M.A., Hobbs, B.E., Paterson, M.S. (1972), *Experimental deformation of single crystals of biotite*, Contributions to Mineralogy and Petrology, vol. 38, no. 1, p. 21-36
- Fagereng, A., Hillary, G.W.B., Diener, J.F.A. (2014), *Brittle-viscous deformation, slow slip, and tremor*, Geophysical Research Letters, vol. 41, no.12, p.4159-4167
- H. Fossen (2010), *Structural Geology*, Cambridge, Cambridge University Press
- J.P. Hirth and J. Lothe (1968), *Theory of dislocations*, New York, McGraw-Hill Book Company
- Griggs, J., Lang, A.C., Gruber, J., Tucker, G.J., Taheri, M.L., Barsoum, M.W. (2017) *Spherical nanoindentation, modeling and transmission electronmicroscopy evidence for ripplations in Ti_3SiC_2* , Acta Materialia, vol. 131, p. 141-155

- Gruber, J., Lang, A.C., Griggs, J., Taheri, M.L., Tucker, G.J., Barsoum M.W.(2016), *Evidence for Bulk Ripplifications in Layered Solids*, Scientific Reports, vol. 6, no. 33451
- D. Hull and D. J. Bacon (2011), *Introduction to dislocations*, Amsterdam, Butterworth - Heineman
- Imber, J., Holdsworth, R.E, Butler, C.A., Strachan, R.A. (2001), *A reappraisal of the Sibson-Scholz fault zone model: The nature of the frictional to viscous ("brittle-ductile") transition along a long-lived, crustal-scale fault, Outer Hebrides, Scotland*, Tectonics, vol. 20, no. 5, p. 601-624
- Imber, J., Holdsworth, R.E., Smith, S.A.F., Jefferies, S.P., Collettini, C. (2008), *Frictional-viscous flow, seismicity and the geology of weak faults: a review and future directions*, Geological Society, London, Special Publications, vol. 299, p. 151-173
- Karato, S. (1987), *Scanning electron microscope observation of dislocations in olivine*, Physics and Chemistry of Minerals, vol. 14, no. 3, p. 245-248
- Kronenberg, A.K., Kirby, S.H., Pinkston, J. (1990), *Basal Slip and Mechanical Anisotropy of Biotite*, Journal of Geophysical Research, vol. 95, no. 12, p.19257-19278
- Kushima, A., Qian, X., Zhao, P., Zhang, S., Li, J. (2015) *Ripplifications in van der Waals Layers*, Nano Letters, vol. 15, no.2, p. 1302-1308
- Langdon, T.G. and Yavari, P. (1982), *An investigation of Harper-Dorn creep—II. The flow process*, Acta Metallurgica, vol. 30, no. 4, p. 881-887
- Manonukul, A., Dunne, F.P.E., Knowles, D. (2002), *Physically-based model for creep in nickel-base superalloy C263 both above and below the gamma solvus*, Acta Materialia, vol. 50, no. 11, p. 2917-2931
- Mares, V.M. and Kronenberg A.K. (1993), *Experimental deformation of muscovite*, Journal of Structural Geology, vol. 15, no.9/10, p.1061-1075
- Mariani, E., Brodie, K.H., Rutter, E.H. (2006), *Experimental deformation of muscovite shear zones at high temperatures under hydrothermal conditions and the strength of phyllosilicate-bearing faults in nature*, Journal of Structural Geology, vol. 28, no.9, p.1569-1587
- Meike, A. (1989), *In situ deformation of micas: A high-voltage electron-microscope study*, American Mineralogist, vol. 74, p.780-796
- Moore, D.E. and Lockner, D.A. (2004), *Crystallographic controls on the frictional behavior of dry and water-saturated sheet structure minerals*, Journal of Geophysical Research, vol. 109, no. 3, p. B03401 1-16
- Niemeijer, A.R. and Spiers, C.J. (2005), *Influence of phyllosilicates on fault strength in the brittle-ductile transition: insights from rock analogue experiments*, Geological Society, London, Special Publications, vol. 245, p. 303-327
- Ogorkiewicz, R.M. and Mucci, P.E.R. (1971), *Testing of fibre-plastics composites in three-point bending*, Composites, vol. 2, no. 3, p.139-145
- Poirier, J-P. (1985), *Creep of Crystals: high-temperature deformation processes in metals, ceramics and minerals*, Cambridge, Cambridge University Press

- Putnis, A. (2003), *Introduction to Mineral Sciences*, Cambridge, Cambridge University Press
- Ranalli, G. (1995), *Rheology of the Earth*, London, Chapman & Hall
- Roy, R. (1949), *Decomposition and resynthesis of the micas*, Journal of the American Ceramic Society, vol. 32, no. 6, p. 202-209
- Satake, K. and Atwater, B.F. (2007), *Long-Term Perspectives on Giant Earthquakes and Tsunamis at Subduction Zones*, Annual Review of Earth and Planetary Sciences, vol. 35, p. 349-374
- Shea, W.T. and Kronenberg, A.K. (1992), *Rheology and Deformation Mechanisms of an Isotropic Mica Schist*, Journal of Geophysical Research, vol. 97, no.B11, p.15201-15237
- SPI Supplies, retrieved June 4, 2018, from <https://www.2spi.com/item/z01870/mica-substrates-v4-muscovite/>
- Vedder, W. and Wilkens, R.W.T. (1969), Dehydroxylation and rehydroxylation, oxidation and reduction of micas, The American Mineralogist, vol. 54, p. 482-509
- Wintsch, R.P., Christoffersen, R., Kronenberg, A.K. (1995), *Fluid-rock reaction weakening of fault zones*, Journal of Geophysical Research: Solid Earth, vol. 100, no. 7, p. 13021-13032
- Zhang, L. and He, C. (2016), *Frictional properties of phyllosilicate-rich mylonite and conditions for the brittle-ductile transition*, Journal of Geophysical Research: Solid Earth, vol. 121, no.4, p. 3017-3047